

2003

Performance Advantages of Maximum Likelihood Methods in PRBS-Modulated Time-of-flight Energy Loss Spectroscopy

Zhongyu Yang

Follow this and additional works at: <http://digitalcommons.library.umaine.edu/etd>



Part of the [Atomic, Molecular and Optical Physics Commons](#)

Recommended Citation

Yang, Zhongyu, "Performance Advantages of Maximum Likelihood Methods in PRBS-Modulated Time-of-flight Energy Loss Spectroscopy" (2003). *Electronic Theses and Dissertations*. 320.
<http://digitalcommons.library.umaine.edu/etd/320>

This Open-Access Dissertation is brought to you for free and open access by DigitalCommons@UMaine. It has been accepted for inclusion in Electronic Theses and Dissertations by an authorized administrator of DigitalCommons@UMaine.

**PERFORMANCE ADVANTAGES OF MAXIMUM LIKELIHOOD METHODS
IN PRBS-MODULATED TIME-OF-FLIGHT ELECTRON ENERGY LOSS
SPECTROSCOPY**

By

Zhongyu Yang

B.S. East China Normal University, 1994

A THESIS

Submitted in Partial Fulfillment of the

Requirements for the Degree of

Doctor of Philosophy

(in Physics)

The Graduate School

The University of Maine

May, 2003

Advisory Committee:

Brian Frederick, Associate Professor of Chemistry, Advisor

Peter Kleban, Professor of Physics

Robert Lad, Professor of Physics

William Unertl, Professor of Physics

David Frankel, Senior Research Scientist, Laboratory for Surface Science and
Technology

Jack Rowe, External Reader, Senior Research Scientist, Army Research Office

LIBRARY RIGHTS STATEMENT

In presenting this thesis in partial fulfillment of the requirements for an advanced degree at The University of Maine, I agree that the Library shall make it freely available for inspection. I further agree that permission for "fair use" copying of this thesis for scholarly purposes may be granted by the Librarian. It is understood that any copying or publication of this thesis for financial gain shall not be allowed without my written permission.

Signature: 

Date: 5/9/2003

**PERFORMANCE ADVANTAGES OF MAXIMUM LIKELIHOOD METHODS
IN PRBS-MODULATED TIME-OF-FLIGHT ELECTRON ENERGY LOSS
SPECTROSCOPY**

By Zhongyu Yang

Thesis Advisor: Dr. Brian Frederick

An Abstract of the Thesis Presented
in Partial Fulfillment of the Requirements for the
Degree of Doctor of Philosophy
(in Physics)
May, 2003

This thesis describes the design, experimental performance, and theoretical simulation of a novel time-of-flight analyzer that was integrated into a high resolution electron energy loss spectrometer (TOF-HREELS).

First we examined the use of an interleaved comb chopper for chopping a continuous electron beam. Both static and dynamic behaviors were simulated theoretically and measured experimentally, with very good agreement. The finite penetration of the field beyond the plane of the chopper leads to non-ideal chopper response, which is characterized in terms of an "energy corruption" effect and a lead or lag in the time at which the beam responds to the chopper potential.

Second we considered the recovery of spectra from pseudo-random binary sequence (PRBS) modulated TOF-HREELS data. The effects of the Poisson noise distribution and the non-ideal behavior of the "interleaved comb" chopper were simulated. We showed, for the first time, that maximum likelihood methods can be

combined with PRBS modulation to achieve resolution enhancement, while properly accounting for the Poisson noise distribution and artifacts introduced by the chopper. Our results indicate that meV resolution, similar to that of modern high resolution electron energy loss spectrometers, can be achieved with a dramatic performance advantage over conventional, serial detection analyzers.

To demonstrate the capabilities of the TOF-HREELS instrument, we made measurements on a highly oriented thin film polytetrafluoroethylene (PTFE) sample. We demonstrated that the TOF-HREELS can achieve a throughput advantage of a factor of 85 compared to the conventional HREELS instrument. Comparisons were made between the experimental results and theoretical simulations. We discuss various factors which affect inversion of PRBS modulated Time of Flight (TOF) data with the Lucy algorithm. Using simulations, we conclude that the convolution assumption was good under the conditions of our experiment. The chopper rise time, Poisson noise, and artifacts of the chopper response are evaluated. Finally, we conclude that the maximum likelihood algorithms are able to gain a multiplex advantage in PRBS modulation, despite the Poisson noise in the detector.

ACKNOWLEDGMENTS

First of all, I would like to thank my advisor, Dr. Brian Frederick, who is largely responsible for making my graduate school experience a positive one. Not only was this whole project originally formed from his ideas, but has also seen success due to his advice, knowledge and experience. Brian has been a great advisor on all fronts, from the technical and conceptual realm to personal advice for career and life in general. For all this, and for his continuing support of me as a Research Assistantship, I am very grateful.

Thanks also to Prof. Peter Kleban, my co-advisor in committee group, he gave me a lot of precious advice in theoretical simulation. I also like to present my appreciation to Prof. William Unertl, he not only gave me useful advice in the whole project and also teach me in using AFM system. I am also indebted to Prof. Robert Lad and Dr. David Frankel for their patience, advice and time.

Next, there is a very important person for me, Dr. Robert Jackson who worked with me over the last 5+ years on this project. In the beginning, Dr. Robert Jackson taught me all the detailed technical know-how about the vacuum, and the EELS system. Then we attempted to build an idle old EELS system into a simple TOFEELS system to do preliminary experiment. In last two year, based on his mechanical design, a state-of-art new TOF-EELS system was build. The bulk of the data presented here was a result of him and I working together. During the whole project, he always provides a great deal of comic relief which even made the labor work become so fun.

There is no room to thank all the people who have helped me survive grad school in various ways, but I am overwhelmingly grateful to all of you. Special thanks to

Crother Bronson and Jay Legore. Bronson is the one that I ask for help whenever I got electronic trouble in experiment. Jay gave a lot of help in build the system and discussion about the deconvolution method.

Funding for this project was received from the National Science Foundation.

Of course, I can't go without mentioning my wife Liying, who has provided me with unconditional love and support through our eight years of marriage, and who is my inspiration. Her solid trouble shooting skill in program saved a lot of time for me in struggling to make the theoretical simulation work. And to my family, my parents and sister and brother and their families. I am forever thankful for all of you.

TABLE OF CONTENTS

ACKNOWLEDGMENTS.....	ii
LIST OF FIGURES.....	vii
Chapter	
1. INTRODUCTION	1
1.1 General Description of HREELS.....	1
1.1.1 Dipole Scattering Mechanism.....	6
1.1.2 Impact Scattering Mechanism.....	7
1.1.3 Negative Ion Resonance Scattering Mechanism.....	9
1.2 The Advantages and Disadvantages of HREELS.....	11
1.3 Possible Methods to Achieve a Throughput Advantage in HREELS.....	13
1.4 Comparison of TOF-HREELS and Conventional HREELS.....	20
1.5 General Description of the Hadamard Method.....	22
1.6 Relationship Between Hadamard Spectroscopy and PRBS-TOF Methods.....	25
1.7 Maximum Likelihood Methods for Resolution Enhancement.....	28
1.8 Organization of the Thesis.....	32
2. APPLICATION OF THE INTERLEAVED COMB CHOPPER TO TOF-HREELS	33
2.1 Introduction.....	33
2.2 Experimental Methods.....	34
2.3 Theoretical Model.....	37
2.4 Experimental Results.....	40

2.5 Theoretical Simulation Results and Discussion.....	43
2.6 Conclusions.....	49
3. ADVANTAGES OF MAXIMUM LIKELIHOOD METHODS FOR PRBS MODULATED TOF ELECTRON SPECTROMETRY.....	50
3.1 Introduction.....	50
3.2 Theoretical Background.....	51
3.3 Simulation of PRBS Modulated TOF Data.....	56
3.4 Results of Cross Correlation vs. Maximum Likelihood Recovery.....	58
3.5 Conclusions.....	64
4. DESIGN OF A TOF-HREELS SPECTROMETER.....	66
4.1 Introduction.....	66
4.2 Description of the Conventional HREELS Instrument	68
4.3 The TOF Analyzer.....	71
4.3.1 Chopper Assembly.....	71
4.3.2 Magnetic Shielding.....	72
4.3.3 Faraday Shielding.....	73
4.3.4 The Detector.....	73
4.4 The Electronics.....	74
5. FACTORS AFFECTING INVERSION OF PRBS MODULATED TOF DATA WITH THE LUCY ALGORITHM.....	77
5.1 Introduction.....	77
5.2 Theoretical Background.....	78
5.3 Methods.....	85

5.3.1	Experimental.....	85
5.3.2	Trajectory Simulation Methods.....	87
5.4	Results.....	92
5.4.1	Experimental Results.....	92
5.4.2	Simulation Results.....	100
5.5	Discussion and Conclusions.....	109
5.5.1	Intrinsic Time Resolution (Single Pulse Mode).....	109
5.5.2	Resolution in Spectra Recovered from PRBS Modulation.....	116
5.5.3	Performance of the PRBS-TOF Instrument.....	121
5.5.3.1	Conventional HREELS Spectrometer.....	123
5.5.3.2	Single Pulse TOF Instrument.....	124
5.5.3.3	PRBS-Modulated TOF Instrument.....	131
6.	SUMMARY AND FUTURE WORK.....	139
6.1	Summary of Results.....	139
6.2	Future Improvements to Instrument.....	141
6.2.1	Resolution.....	141
6.2.2	Reduction of Artifacts.....	142
6.2.3	Improvement to Simulation Methods.....	143
6.2.4	Lens Design.....	144
6.3	Application to Demonstrate Performance Advantages.....	144
	APPENDIX.....	146
	REFERENCES.....	153
	BIOGRAPHY OF THE AUTHOR.....	159

LIST OF FIGURES

Figure 1.1	The schematic drawing of the energy distribution before and after scattering in the specular direction.....	2
Figure 1.2	The relationship of the current measured at the detector versus the resolution (FWHM) of the ultimate spectrometer for the new spectrometer (squares) and the penultimate design (circles).....	4
Figure 1.3	A photograph of the EELS 3000 (from LK Technologies) at the Laboratory for Surface Science and Technology.....	5
Figure 1.4	A schematic drawing of how the orientation of a dynamic dipole leads to the metal surface dipole scattering mechanism.....	8
Figure 1.5	A typical schematic drawing of Hadamard transform spectrometer.....	23
Figure 1.6	A simple case to illustrate the convolution in time domain.....	27
Figure 2.1	The photograph of the chopper made in two methods.....	35
Figure 2.2	Schematic diagram of the system designed to characterize chopper.....	36
Figure 2.3	A) Model for an infinite array of infinitely long wires of radius, R , and spacing, d , in the $x=0$ plane, with alternating potential $\pm V_{app}$. B) The two-wire problem obtained by conformal mapping.....	38
Figure 2.4	A) A typical angular distribution, measured with the TOF detector B) Theoretical angular distributions to compare with the experimental results.....	41
Figure 2.5	The experimental Time of Flight histogram.....	42
Figure 2.6	The theoretical simulation of TOF histogram.....	45

Figure 2.7	Contour map of the potential, $\psi(x,y)$, with critical boundaries, $f(x,y, \theta_{acc}, V_{app})$, as a function of the acceptance angle and applied voltage.....	46
Figure 3.1	Illustration of the non-ideal chopper response on the autocorrelation function.....	53
Figure 3.2	Energy corruption histograms for a 2 eV electron as a function of distance from the hopper.....	55
Figure 3.3	Comparison of the object spectrum with simulated single pulse TOF spectra (gate open 8 ns) and the spectra recovered from a PRBS modulated experiment using the cross correlation method.....	60
Figure 3.4	Comparison of the object function with estimates recovered from PRBS modulated data using the cross correlation method and the maximum likelihood method	62
Figure 3.5	A) Comparison of the object function with estimates recovered from PRBS modulated data that includes the non-ideal chopper response using the maximum likelihood method.....	63
Figure 3.5	(continued) B) Illustration of the negative-going artifacts in the cross correlation recovery due to the non-ideal response of the chopper (middle curve) and the importance of accurately determining the response function.....	65
Figure 4.1	Schematic drawing of the TOF-HREELS system.....	67
Figure 4.2	The functional block diagram of the chopper driver circuitry and pulse counting electronics.....	75

Figure 5.1	Critical boundary condition of 4 eV and 3.6 eV on contour plots of the potential for a wire diameter-to-spacing ratio of 0.1.....	79
Figure 5.2	Schematic illustration of the relationship between the time dependence of the potential applied to the chopper, $V_{app}(t)$, and the functions $g_i(t)$	82
Figure 5.3	Schematic drawing of the TOF-HREELS system.....	86
Figure 5.4	Schematic drawing of the trajectory simulation model used to generate noisy data.....	88
Figure 5.5	Flowchart of the trajectory simulation method.....	90
Figure 5.6	Chopper response function taken under different lens condition.....	93
Figure 5.7	Analysis of the effects of A) the dead time of the drive electronics (circles) and the response function of the system (squares) as a function of the number of consecutive 1's (transmission on) in the PRBS sequence; and B) the transmission during the open periods.....	95
Figure 5.8	Auto-correlation functions corresponding to chopper response functions measured for a range of different monochromator angles.....	98
Figure 5.9	Comparison of the vibrational loss spectrum of an highly oriented PTFE film, measured by the conventional HREELS analyzer, with the spectra measured by the TOF detector.....	99
Figure 5.10	The simulated chopper response function and PRBS spectrum of PTFE films with two methods.....	101
Figure 5.11	Comparison between the experimental TOF spectrum and the simulation results of the PTFE films.....	104

Figure 5.12 The recovery results of simulated PRBS spectrum by varying only the duty cycle.....	107
Figure 5.13 The recovery results of simulated PRBS spectrum by simulating the reduction height in single bits.....	108
Figure 5.14 The TOF histograms converted from the energy corruption histograms of Fig. 5.2.....	111
Figure 5.15 A) The onset of a chopper response function for 4 eV beam with $2R/d = 0.1$. B) The relationship between the lag time and d -spacing C) The relationship between the rise time and d -spacing.....	113
Figure 5.16 The dependence of the rise time (10%-90%) on beam energy and the FWHM of the monochromatic electron beam.....	115
Figure 5.17 The explanation of rise time based on Fourier transform.....	118
Figure 5.18 Comparison of the shape of the a single pulse calculated with the Monte Carlo method on a 25 ps time bin size for a kinetic energy of 4 eV (bars) and 3.6 eV (solid curves) to show that the energy dependence of the shape of the response function is negligible under the conditions of this experiment.....	122
Figure 5.19 The importance of the signal-to-noise ratio (S/N) and the shape of the instrumental response function in recovering the synthetic data.....	127
Figure 5.20 Comparison of the convolution of a pair of Lorentzians of equal height and two smaller Lorentzians of differing shape.....	129
Figure 5.21 Illustration of the numerical method used to assess the signal-to-noise ratio in the synthetic data recovered with the Lucy algorithm.....	137

Figure 5.22 A) The multiplex advantage predicted from the Eq. 21 for the Hadamard transform recovery of the PTFE spectrum. B) The multiplex advantage is calculated by taking the ratio of the S/N using Lucy and PRBS modulation to the S/N in a single pulse mode experiment.....	138
Figure A.1 A schematic drawing of the PTFE film deposition instrument.....	147
Figure A.2 A photo of PTFE samples taken under the microscope.....	150
Figure A.3 Some AFM images for the PTFE film on Pt substrate.....	151
Figure A.4 A height profile for the PTFE films on platinum substrate was obtained by scanning along a line perpendicular to the PTFE ribbons.....	152

Chapter 1

INTRODUCTION

1.1 General Description of HREELS

High resolution electrons energy loss spectroscopy (HREELS) is a technique that uses an electron beam to measure the properties of solid surfaces, such as phonon vibrations or the vibrational modes of adsorbed molecules on the surface.[1] Because the momentum of the electrons is relatively large, the technique has played an important role in mapping the dispersive curves of surface phonons, i.e. the relationship between the phonon energy and momentum[1]. A primary role of HREELS in surface science has been to identify the fragments of molecules or intermediates, which form during adsorption on surfaces. By measuring the vibrational energy loss, the physical and chemical properties of the atoms or molecules adsorbed on the surface can be understood in considerable detail, for example in the work done by Rowe and Ibach on semiconductor surfaces[2, 3]. By application of selection rules, especially on metallic substrates, the orientation of atoms or molecules on the surface can also be determined[4-9]. A fundamental understanding of the vibrational properties of surfaces involves measurement of energy transfer processes and their associated lifetimes. HREELS has been particularly important in probing the dynamics of vibrational energy transfer when temporary negative ions are involved[10, 11].

In HREELS, a highly monochromatic beam of low energy electrons (typically 1-10 eV) is scattered from a solid surface as illustrated in Figure 1.1. Most surfaces have reflectivities less than 1%. Of the minority that backscatter, a large portion of the electrons are scattered elastically, that is, without losing any energy. The fraction of the

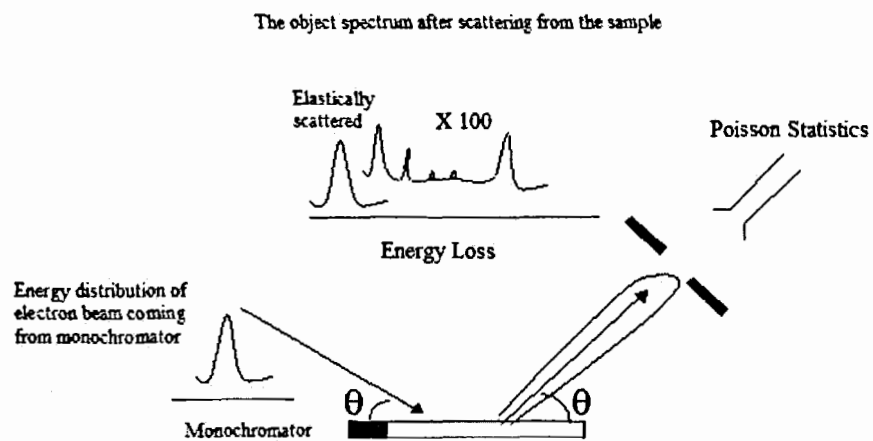


Figure 1.1 The schematic drawing of the energy distribution before and after scattering in the specular direction.

incident electrons that are scattered inelastically, that is, after losing various amounts of energy, is typically less than 10^{-4} of the incident electron beam current. These energy losses correspond to excitation of vibrational modes or electronic transitions in the surface. Because the fraction of electrons that convey “useful” information is so small, the throughput of the instrument is particularly important. In fact, only on relatively well surfaces, where the inelastically scattered electrons suffer small deflections away from the specular direction, has the intensity of the loss peaks beam sufficiently large to be practical. Therefore, by scanning the kinetic energy of the scattered electrons from the initial energy to lower kinetic energies, an energy loss spectrum is obtained.

Because the magnitude of these energy losses is very small, varying between a few milli-electronvolts (meV), and several hundred meV, an HREELS spectrometer must prepare an electron beam with an energy distribution of width several meV or less. Typically the energy of the incident electron beam can be adjusted in the range of 1-200 eV.

From the 1970's to 1990's, Ibach and co-workers made major contributions to the development of the field and improvement of HREELS instrumentation[12, 13]. Ibach's ultimate monochromator achieves a resolution of 1 meV with 10^6 times greater current than early spectrometers. Fig. 1.2 shows the relationship of the current measured at the detector versus the resolution (FWHM) of the ultimate spectrometer for the new spectrometer (squares) and the penultimate design (circles). Fig 1.3 shows the instrument used in this work, which was built according to Ibach's penultimate design (EELS 3000, LK Technologies). The major improvement in the optics[12] involved careful modeling of the space charge effects in the monochromator. The analyzer design is similar to the

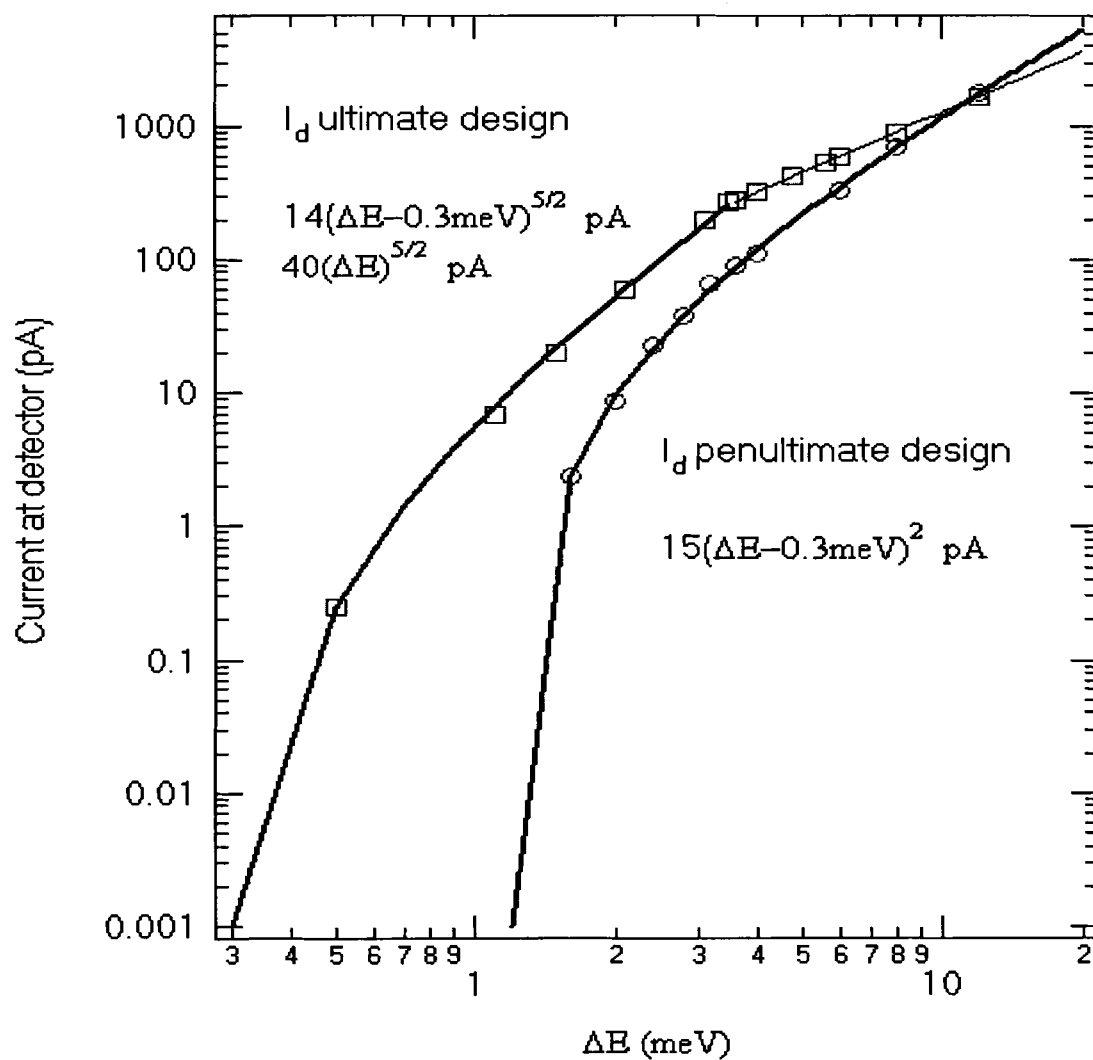


Figure. 1.2 The relationship of the current measured at the detector versus the resolution (FWHM) of the ultimate spectrometer for the new spectrometer (squares) and the penultimate design (circles).

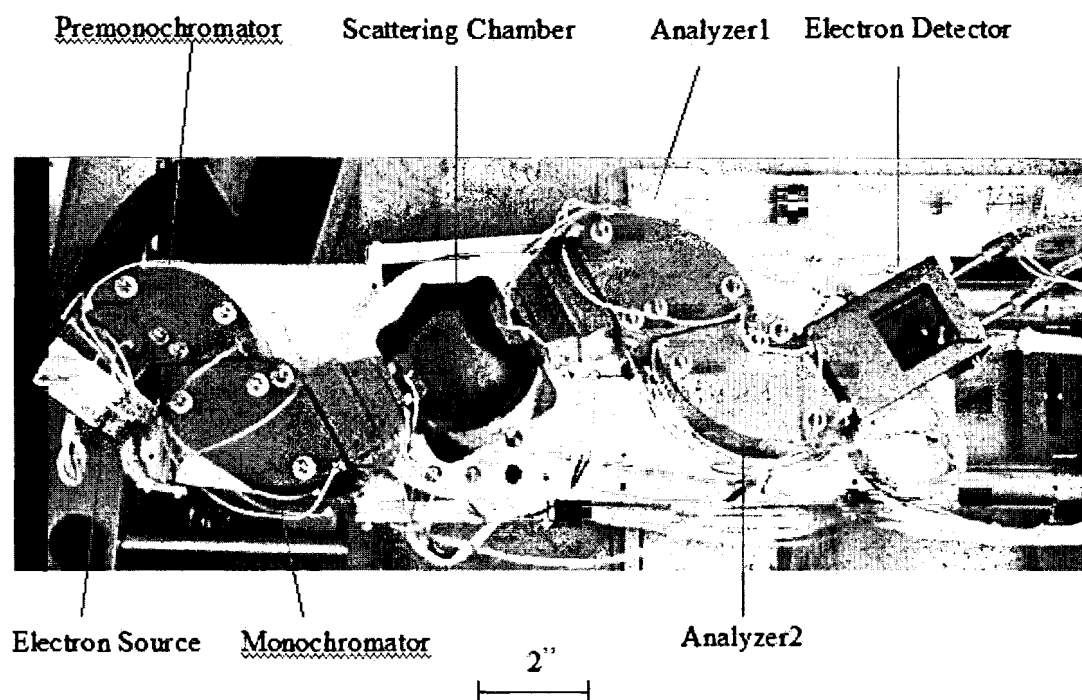


Figure 1.3 A photograph of the EELS 3000 (from LK Technologies) at the Laboratory for Surface Science and Technology.

main monochromator and also achieves resolution at the 1 meV level. However, because it is a dispersive device, that accepts or transmits only one energy of electrons at a time, the data collection time is relatively long compared to other surface spectroscopies, such as infrared reflection absorption spectroscopy (IR-RAS)[14, 15]. Therefore, the work described in this thesis focused on gaining a throughput advantage using time-of-flight (TOF) techniques for the electron energy analyzer. While the penultimate design[12] does not achieve the performance of the ultimate design[13], it is somewhat more flexible and was more convenient for coupling to the time-of-flight detector developed in this work.

Before discussing the background and general approach that we have adopted, we first survey the information that may be obtained in HREELS to illustrate the reasons that a parallel detection electron energy analyzer may benefit the development of the field. There are three important scattering mechanisms involved in HREELS. The importance of each depends upon the surface and/or adsorbate system.

1.1.1 Dipole Scattering Mechanism

When electrons interact with adsorbed molecules or optical phonons of oxide surfaces through the dipole mechanism, the electric field of the incident electron perturbs the oscillating (time dependent) field of dipole active vibrational modes at the surface[1, 16, 17]. At large distances (10-100 nm) the incident electron cannot distinguish individual oscillating atoms, but instead experiences the long-range field constituting surface phonons (collective oscillations of atoms). The energy losses are usually small compared to the incident energy and so conservation of energy and momentum causes the

deflection of an inelastically scattered electron to be small (less than a few degrees). When the surface is periodic, the reflected electron beam is constrained to diffraction conditions, which means that the inelastically scattered electrons appear in a "dipole scattering lobe" within a degree of the specular (or other diffraction) condition.

The so-called metal surface dipole selection rule applies for dipole scattering. This states that only vibrational modes which result in a change in the dipole moment perpendicular to the surface plane can be observed[1]. Fig.1.4 shows a schematic diagram of a surface dipole at a metal surface. An image charge is set up on metallic surfaces which enhances dynamic dipoles perpendicular to the surface, but tends to cancel any dynamic dipole moment oriented parallel to the surface plane. Normal modes that have a component of their dipole perpendicular to the surface are dipole allowed, while modes that have no dynamic dipole moment perpendicular to the surface are forbidden (in reality, the screening is not perfect and weak "forbidden" modes are sometimes observed). The presence of certain vibrational modes and the absence of others can therefore be used to deduce the surface point group, from which the orientation of a molecule, with respect to the surface plane, can be determined. The scattering cross-section varies with the inverse of the incident electron energy and a theoretical treatment of dipole scattering has been developed based on classical electrodynamics[1].

1.1.2 Impact Scattering Mechanism

In this mechanism, the incident electrons are scattered by much shorter range interactions, on the order of atomic dimensions. This short-range scattering mechanism involves much larger momentum transfer and produces a broad angular distribution of

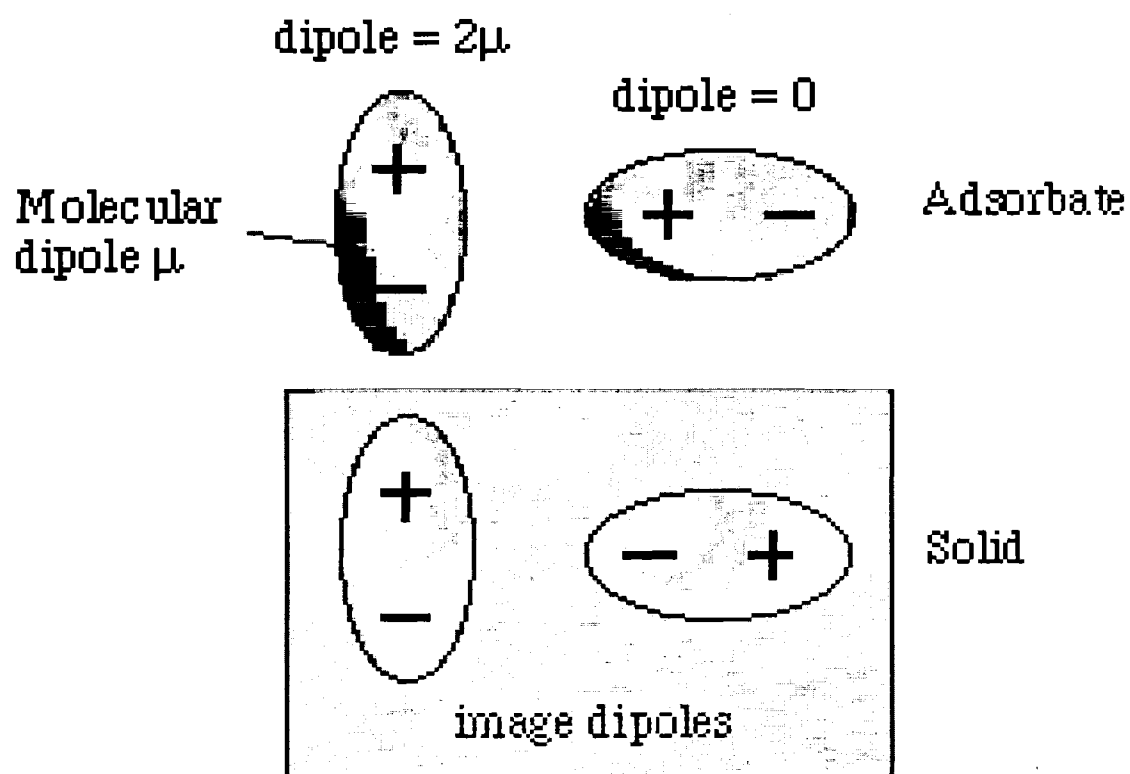


Figure 1.4 A schematic drawing of how the orientation of a dynamic dipole leads to the metal surface dipole scattering mechanism.

inelastically scattered electrons. The final angle of the scattered electron is determined by the component of the phonon vibration parallel to the surface. Impact and dipole scattering mechanisms can be distinguished, therefore, by moving the detector away from the specular direction, since the dipole active modes decrease proportional to the intensity in the elastic peak off specular. The impact scattering cross-section varies with incident beam energy, generally increasing with energy. However, the cross section oscillates due to multiple scattering effects[18] that are also important in the LEED I/V experiment [19]. Thus, the calculations are very intensive, and the lack of available experimental data has limited the activity in this area. Nevertheless, good example of comparison between experimental and theory exist, for example in the early work of Wilson Ho and Ibach *et. al.*[1, 20]. Impact scattering usually has a much lower probability than dipole scattering. Because the acquisition time is large and a range of angle dependant spectra is required, such studies are less common. However, HREELS is one of the few techniques that can determine the azimuthal orientation of adsorbate or highly oriented material. While most HREELS spectrometers provide rotation of either the monochromator or analyzer in the scattering plane, out-of-plane rotation, as implemented in angle resolved UPS, has not been widely performed. This limits the symmetry of phonons that can be interrogated with typical HREELS instruments.

1.1.3 Negative Ion Resonance Scattering Mechanism

Here, the incident electrons are temporarily captured by empty electronic energy levels of atoms or molecules. In the gas phase, negative ion resonance (NIR) scattering dominates, and the theory has been extensively developed by Teillet Billy[21] and

Gauyacq others[22]. The gas phase work has been reviewed in detail by Schulz[23, 24] and The lifetime of the state is critical to the loss intensity, and for this reason Ibach and Mills argued that, for small molecules adsorbed on metallic surfaces, the negative ion cross section would be small[1]. However, for larger molecules[25, 26] or weakly bond adsorbates[27] the negative ion resonance scattering can be dominant. Palmer and Rouse[11] and Sanche[28] have reviewed recent work in this area.

In the NIR scattering process, the electron is trapped into a temporary negative ion state derived from the unoccupied orbitals of the molecule. As the negative ion relaxes toward its equilibrium geometry, the vibrational wave function is no longer in a stationary state of the neutral molecule. Emission of the electron provides an efficient means of generating highly excited vibrational states of the neutral molecule. The process can be treated either within a Franck-Condon picture[29] or within a time dependent electron dynamics model using, for example, wave packet calculations[30].

Experimentally, the angular and energy dependence of the differential scattering cross section provides a wealth of information. The cross section of a vibrational mode goes through a maximum when the incident beam energy is in resonance with the “dressed” NIR state, which provides information about the energy and lifetime of the unoccupied orbital[10]. The vibrational modes that are excited are related to the spatial localization of the state on the molecule[26]. The directions of the incident or scattered beam, in which the differential loss cross-section vanishes, allow nodal surfaces to be determined if the molecule is azimuthally oriented. Finally, the width of the resonance

provides dynamical information concerning the lifetime and the displacement of the negative ion potential energy surface with respect to that of the ground state[31].

1.2 The Advantages and Disadvantages of HREELS

Generally, the main strengths of HREELS compared to other (optical) vibrational techniques rely on the properties of these scattering mechanisms. Electrons are scattered by the outermost one or two layers of a surface and do not penetrate the bulk, unlike photons. This makes HREELS intrinsically more surface sensitive than infrared. Furthermore, the range of losses observed in HREELS experiments covers the entire vibrational spectrum: vibrations of <1000 wavenumbers cannot be observed in IR spectroscopy without specialized windows and detector technology. Angle- and incident energy-dependent experiments can be performed with most HREEL spectrometers allowing studies of molecular geometries and scattering mechanisms to be performed. In the following, the advantages and disadvantages of HREELS are classified.

The advantages of HREELS can be classified among properties of the mode of operation and implications of the nature of electron scattering. Because the loss spectrum is measured directly, rather than as a ratio to a “blank” or background spectrum (as in FTIR), HREELS can measure the vibrational loss spectrum of the clean, as well as the adsorbate covered surface. In this respect, it is similar to Raman and emission spectroscopies. Whereas the sensitivity of an absorption spectroscopy is limited by the fluctuations in the source, which leads to instability in the signal to background ratio, in

HREELS the background is controlled by the dark count of the detector (< 2 cts/s) and so the background is usually negligible.

Electron scattering offers a number of opportunities, which are apparent from the theoretical basis of the three scattering mechanism. Because the primary beam energy can be chosen over a range from 1 to several hundred eV, it is possible to optimize the cross section for vibrational losses (< 0.5 eV) as well electronic losses (0-100 eV) in the same instrument. The strong interaction between electrons and condensed matter results in high surface specificity. This also leads to high sensitivity, typically small fractions of a monolayer coverage ($\approx 0.1\%$), particularly when the adsorbate has a strong dynamic dipole moment. Whereas the dipole mechanism (in HREELS and IR) only permits the orientation normal to a metal surface to be detected, the impact and NIR scattering mechanism yield additional information about azimuthal orientation and the structure of electronically excited states. Variation in the reflectivity, whether from negative ion resonance or properties of the bulk band structure, provides additional information. Although all materials vibrate, and in principle can be measured with HREELS, there are practical constraints.

The disadvantages of HREELS can be understood in relation to the use of electrons to probe surfaces. First, the short mean free path in air and its sensitivity to electric and magnetic fields requires a high quality vacuum with magnetic shielding. The vacuum requirements are demanding because of the need to maintain clean surfaces within the dispersive sector so that the work function is as homogeneous as possible. The aberrations in ion and electron optics, as well as space charge effects make focusing

electron beams difficult which limits the spatial resolution of conventional instrument. Despite dramatic improvement in resolution, the achievable resolution is not as good on rough surfaces as can be achieved on well-ordered surfaces. Surface charging presents a challenge on insulating surfaces, although considerable work has been done with thin films and neutralizing beams[32-34]. However, the optical phonon spectra of many insulating materials, such as oxides, tend to obscure adsorbate losses and limit sensitivity. Some experimental[35] and theoretical deconvolution approaches[36] have been used to alleviate this problem. By comparison with other techniques, HREELS tends to be relatively expensive, difficult to operate due to the large number of potentials that must be tuned, and requires relative long data acquisition times.

1.3 Possible Methods to Achieve a Throughput Advantage in HREELS

As we discussed in Section 1.1, the angular dependence of the energy loss cross section contains a wealth of information. Depending upon the goals of a particular experiment, different types of analyzers could be designed to increase the throughput relative to a conventional HREELS instrument. The option chosen in this work was to use time-of-flight methods to gain a throughput and a multiplex advantage; however, the alternative means of using a spatially resolved, or parallel detector was also considered. We first discuss the ideal characteristics of a spectrometer designed for experiments that are optimized for dipole, impact, and negative ion resonance scattering, and then discuss the advantages of the TOF vs. parallel detector technology available at the time this work was started.

In dipole scattering, the dipole lobe is somewhat broader than the angular distribution of the elastic peak. On well-ordered surfaces, the FWHM of the elastic peak is typically about $\pm 1\text{-}2^\circ$. Because the dipole lobe shifts away from the specular direction for increasing loss energy and broadens at lower primary beam energies, the small acceptance angle of the state-of-the-art conventional spectrometers results in significant reduction in the transmission at low energies (2-4 eV) where the dipole cross section is maximized. The small acceptance angles are necessary to achieve the high energy resolution with the dispersive sector instruments[12]. Nevertheless, for the purpose of comparing on-specular with off-specular scattering, we suggest that the acceptance angle should be chosen to be large enough to include the entire dipolar lobe, which should be in the range of $\pm 2\text{-}4^\circ$. Interestingly, this is similar to the range of early, lower resolution instruments, such as the Riber Sedra spectrometer[37].

On surfaces that are polycrystalline or poorly ordered, the lack of periodicity means that the momentum conservation condition does not hold and the specular peak is considerably broadened. Often the elastic peak has a FWHM as large as $\pm 10^\circ$. A lens that increases the acceptance angle to a larger range, such as this, would increase the signal with no loss of angular information. Perhaps such a design, if high energy resolution can still be achieved, would allow the use of HREELS on more technologically relevant surfaces.

In the impact scattering regime, we consider two particular cases with significantly different requirements for the angular resolution required. For phonon band mapping, a high k_{\parallel} resolution is needed. The angular resolution is energy dependent, and at higher energies, where the impact cross section is generally larger, the deflection angle

corresponding to the edge of the Brillouin zone decreases, requiring higher angular resolution. On the basis of these considerations, Ibach chose an acceptance angle criterion of order ± 0.5 [12].

By contrast, when impact scattering is utilized to determine the non-dipole active modes and to investigate the azimuthal orientation of molecules on single crystal surfaces, the cross section can vanish under special conditions, e.g. on specular when the surface point group contains a mirror plane perpendicular to the scattering direction or within the scattering plane when the scattering plane contains a mirror plane. In principle, the impact excited modes may show angular distributions that reflect these symmetries, but due to thermal motion of the molecules there will be minima but not necessarily zeroes in the high symmetry conditions. Therefore, the angular resolution required for measurement of the angular distribution is probably much lower than required for phonon band mapping. Early studies of impact scattering, for example by Ho and Willis for the H/W(110) surface suggest that an angular resolution of $\pm 2-4^\circ$ may be adequate. An instrument that could measure the angular distribution of in-plane vs. out-of-plane polarized modes would allow new experiments, such as the freezing out of molecular motion at low temperatures, in a manner similar to results with ESDIAD (electron stimulated desorption ion angular distributions)[38].

For negative ion resonance scattering, the characteristics of the angular distribution are perhaps more interesting than in the case of impact scattering. Recent work by Chen, et al, has shown that the CH stretch cross section varies significantly with both primary beam energy and emission angle for highly oriented benzene rings in the $c(8 \times 2)$ benzoate structure on Cu(110). High energy resolution is needed to resolve all of

the ring modes and the throughput of the conventional spectrometer precluded measurement of entire loss spectra for a wide range of angles and energies. Thus, a dramatic improvement in throughput is necessary to enable more complete studies of the angle- and energy dependent loss cross section. Again, the symmetry of the molecular orbitals should lead to zeroes in the loss cross section when the scattering conditions are such that either the incident (i.e. monochromatic beam) or emission (i.e. analyzer) direction is in a nodal plane (or nodal surface) of the adsorbate. Due to thermal motion the angular resolution required is probably similar to that required for impact scattering, but the range of angles required is much larger than in impact scattering. For example, Richardson and Jones[39] measured the angular distribution of the shape resonance for CO/Ni(110) over a 30° range in 3-4° intervals.

On this basis, we now consider the use of both TOF and parallel detection methods to increase the performance of a high energy resolution spectrometer. As we will discuss in greater detail below, TOF methods could provide a dramatic throughput and multiplex advantage. This would be particularly useful in dipole scattering, where the information of interest is already collimated into a narrow solid angle (for well-ordered surfaces) or there is little angular information to be obtained, such as on poorly ordered surfaces. By contrast, in the area of negative ion resonance scattering, optics that transmit the angular distribution to a position sensitive detector could result in a tremendous parallel detection advantage. For the reasons outlined below, the former approach was chosen for development of the first generation TOF-HREELS spectrometer.

The key factor in the development of a TOF electron spectrometer is the existence of a fast beam-chopping device. Sub-nanosecond rise times of the chopping system are

required to guarantee that the resolution is comparable to the state-of-the-art conventional HREELS instruments. Several groups have demonstrated the use of a Bradbury-Nielsen gate, more recently referred to as an “interleaved comb” chopper to deflect or pass ions in a TOF mass spectrometer[40-42]. This device consists of a plane of closely spaced parallel wire segments, in which alternate wires are biased with equal but opposite voltage. An ion beam travels perpendicularly to the plane of the chopper. If the potential on the wire sets are grounded, all of the ions pass through the chopper without being affected. However, if the wire sets are held at opposite potentials of equal magnitude with respect to the flight tube potential, the ions will be deflected to one side or the other side depending on the polarity of the field. In this case, the ions can be excluded from the detector by a slit and the chopper is effectively “shut off”.

Prior to this work, there was no experimental evidence and insufficient theoretical understanding of this device to demonstrate whether the “interleaved comb” chopper could achieve sufficiently fast response times to allow electron energy analysis using TOF techniques. We should note, however, one experimental setup in which a pair of closely spaced grids was used to pass electrons by applying a sinusoidal signal. A second pair of grids placed further down a flight path functioned in a similar manner to create a notch filter with an effective energy resolution of 3 meV[43].

The time resolution of pulse counting electronics and microchannel plate detectors has been well established. In fact, several applications of TOF electron spectroscopy have already been reported in x-ray photoelectron spectroscopy in which the ultra-short light pulses of a synchrotron was used to provide the time base. Thus, the detector technology was already established and the time resolution of commercially

available time to digital converters was sufficient for our purposes. We should note, however, that the dead time of these devices was a significant limitation and the need for customized timing electronics still exists.

The alternative approach of using a position sensitive detector presents several challenges. The retarding field analyzer, coupled with microchannel plates and a fluorescent screen, is essentially one solution. However, the retarding field analyzer operates as a high pass filter and would not be practical for measurement of a particular vibrational loss energy if the primary beam is continuously impinging upon the surface. The energy resolution is insufficient, typically being limited to a large fraction of an electron volt due to variation in the work functions of grids and field penetration. If a pulsed primary electron beam could be prepared, then a set of grids could operate as a gating device to admit electrons only during a particular window of flight times. However, this adds the complexity of TOF methods to the challenges of a position sensitive detector. A number of methods have been reported[44-47] to determine positions, and in some cases arrival times, using microchannel plates to amplify electrons and achieve single particle counting. Thus, development work was focused on TOF gating technology, which will enable future work to be pursued with larger area detectors having both time and position measurement capabilities to gain further performance advantages.

We should also note the work of Dubois and Kevan,[48-50] and others[48-50], to implement dispersion compensation in HREELS. In this approach, the exit and entrance slits of the monochromator and analyzer are removed. Electrons flying through the monochromator are dispersed at the exit focal plane. The positions of the electrons on the

focal plane depend on their energy relative to the mean pass energy of the monochromator. By following their time reversal trajectories, these spatially dispersed electrons are focused again at the exit plane of the analyzer. This requires that the monochromator and analyzer be placed symmetrically with respect to the sample position. Therefore, parallel processing of electrons that enter the monochromator with a broad range of energies can be achieved, whereas only a small fraction of those electrons are utilized in the conventional spectrometer. Based on this design, a throughput advantage of a factor of 15 has been reported for the same resolution[49].

Another way to build a parallel detection system in HREELS is to use a multichannel detector, as shown by Ho and coworkers in the designed of their time resolved HREELS (TREELS). With the TREELS, they demonstrated that changes in the nature of the adsorbed species can be monitored in real time[51]. This instrument is made of putting a multichannel detector at the exit focal plane of the analyzer, instead of a narrow slit. The rest of the instrument is the same as the conventional HREELS. TREELS is able to probe adsorbed species in real time, but it has a limited energy range and the instrument is relatively complicated to tune up. In the TREELS, a 96-channel detector was used and a time resolution of 5 millisecond was achieved. If a higher energy range or resolution is required, more detector channels are needed and the radius of the analyzer should be increased, although aberrations in the optics will limit the achievable range and resolution. Therefore, the throughput advantage that can be achieved by the dispersion compensation and TREELS techniques is limited.

1.4 Comparison of TOF-HREELS and Conventional HREELS

The conventional energy analyzer used in HREELS is based upon electrostatic field deflection. The analyzer is tuned to the energy of each energy loss channel and only electrons of that energy are measured. This serial detection scheme limits the actual performance defined in terms of the acquisition time to achieve a spectrum of a specified signal-to-noise ratio (SNR). For example, a scan of 600 meV with step size of 0.2 meV implies 3000 data channels. If the signal is collected for a duration of 1 second per channel, the acquisition time is typically an hour. If the energy of all electrons were measured simultaneously, in a parallel detection scheme, the acquisition time would be reduced from hours to seconds.

Time of Flight (TOF) is a technique used extensively in secondary ion mass spectrometry [52] in which the mass of the ions is measured by determining the time required for the ions to reach the detector after the primary ion beam impinges on atoms in a sample surface and scatters secondary ions. In order to enable such time-dependent measurements; the beam has to be pulsed. The time of arrival of the detected particle can then be measured with respect to the pulsing of the ion beam. In a single pulse mode TOF experiment, in order to achieve high resolution, the duration of the primary pulse is small compared to the period (typically the pulse is $10^{-3} - 10^{-5}$ of the period) which limits the throughput of the instrument. However, the TOF technique has the advantage that all of the ions with different mass generated in a single primary beam pulse can be detected; that is, the TOF method is a parallel detection system which, in principle, can detect 100% of the ions generated in a given pulse. However, when there is a continuous source of ions, such as in orthogonal ionization TOF mass spectrometers, now commercially

available in GC/MS systems[53, 54], the low duty cycle still leads to relatively poor efficiency. A significant improvement can be achieved by combining TOF with advanced modulation methods.

In the conventional TOF method, the time period between two successive chopping events has to be larger than the width of the TOF distribution at the detector so that particles originating from different chopping events will not interfere when arriving at the detector at the same time. In order to improve the time resolution, the duration of the chopper pulse, τ , must be decreased. However, because the time between successive pulses, T , is determined by the width of the TOF distribution, the duty cycle τ/T will also decrease with decreasing τ . This leads to the dilemma of the conventional TOF analysis: to choose between high resolution and high transmission (high SNR).

The trade-off between the resolution and transmission can be overcome by applying the so-called “pseudo-random binary sequence” (PRBS) modulation time of flight technique[55-57]. In this case, the time between successive pulses is no longer required to be larger than the width of the TOF distribution. Therefore, the resolution can be increased without affecting the transmission. On the other hand, the TOF spectra from successive chopping events will overlap at the detector resulting in an overall spectrum which is much more complex than the single pulse mode TOF experiments. In the ideal case, the time modulated spectrum, $y = o \otimes p$, is a convolution of the object spectrum, o , with the modulation function, p . There are special sequences, known as PRBS, or maximal length shift register sequences [58, 59], having the unique property that their autocorrelation functions are approximately a delta function. Therefore, the object

function can be recovered simply by cross-correlation; i.e. $p \oplus y = (p \oplus p) \otimes o \approx o$. To be more precise, the maximal length shift register sequences have discrete autocorrelation functions that are two-valued functions: 1 at zero phase shift, and $-1/(2^n-1)$ at all other phase shifts.

The PRBS-TOF modulation method is closely related to Hadamard spectroscopy. In the next section, we discuss the Hadamard method, since it illustrates the performance advantages in a somewhat simpler situation than in the PRBS-TOF method.

1.5 General Description of the Hadamard Method

The Hadamard technique was originally developed as a means of increasing the optical throughput of a dispersive spectrometer, as illustrated schematically in Fig. 1.5. The incident beam is dispersed spatially by a prism and then passes through a mask that has a specific combination of open and closed slots to accept or reject particular wavelengths. The transmitted part of the light is then collected and impinges on the detector. A data set is formed by using a series of masks that have slot combinations that change in a pattern derived from a Hadamard matrix or S-Matrix. The spectrum is obtained from this data set by a linear matrix multiplication using the inverse of the Hadamard matrix or S-matrix. There are two distinct advantages of this procedure. First, because each slot is open in half of the mask positions, the total amount of light is $n/2$ times larger than is measured in the same amount of time with a conventional, n -element, dispersive instrument. This leads to a throughput advantage. Second, because in each measurement a different combination of the wavelengths pass through the mask, each wavelength is measured multiple times, which leads to an improved SNR, or multiplex

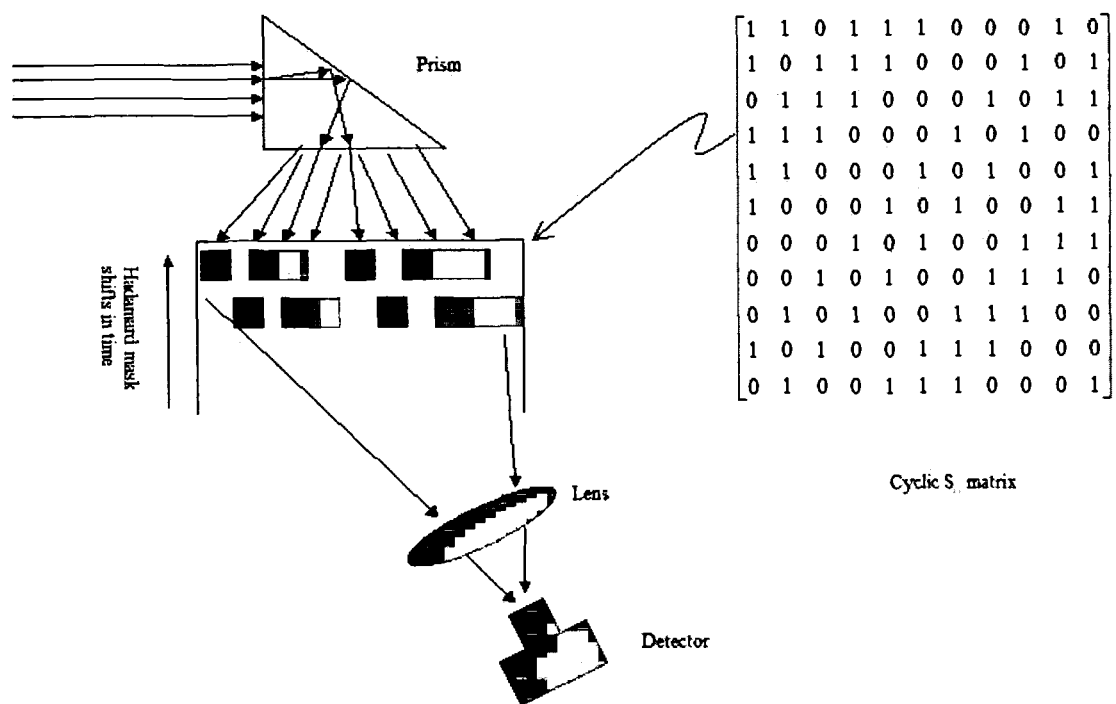


Figure 1.5 A typical schematic drawing of Hadamard transform spectrometer.

advantage. The multiplex advantage can be understood by analogy to the statistical analysis of weighing experiments[58]. If three objects are to be weighed, the simplest procedure is to place each object on the balance and record its weight. However, the random error in each measurement can be reduced if instead the objects are weighed in combinations. First, the three objects can all be placed on the balance and the total is weighed. Then one object is removed and the weight of the two remaining objects is recorded. Finally, the first object is put back on the balance and one of the others is removed. In total, three measurements are still made, but the random errors are distributed among the measurements. When the masses are determined by solving the set of linear equations, the signal to noise ratio (i.e. mass divided by the standard deviation of each error) is increased by $\sqrt{3}$, or in general, \sqrt{n} , where n is the number of objects measured.

There is a close connection between the maximal length shift register (or PRBS) sequences and the Hadamard matrix. The Hadamard matrix is an $n \times n$ matrix of +1's and -1's with the property that $H_n H_n^T = H_n^T H_n = nI_n$. The mask itself is obtained by first normalizing the Hadamard matrix such that the first row and column are all 1's, then omitting the first row and column to produce an $(n-1) \times (n-1)$ matrix, and finally converting all +1's to zero and the -1's to one. This matrix is known as the S-matrix. An example of an 11-element S-matrix is shown in Fig. 1.5. In fact, each row or column of the S-matrix is identical to a PRBS sequence. In the S-matrix, the rows are related by shifting the sequence cyclically to the left. Thus, in Hadamard spectroscopy, there is a spatial multiplexing of the n channels according to a PRBS sequence, which is shifted relative to the spectral elements, at each step in time.

The multiplex advantage depends on both the nature of the spectrum and the noise. Under conditions that the detector noise is large and normally distributed, the multiplex advantage, as shown originally by Fellgett[60], is \sqrt{n} . However, when the noise is shot limited, Plankey and Winefordner[61], showed experimentally that correlations between the signal and noise in the detector, such as is the case for Poisson (counting) noise, reduces the multiplex advantage. Larson et al. [62] and Gompf [63] have shown that in the case of Poisson noise, the multiplex advantage, when recovering the spectrum with the Hadamard matrix inversion, is frequency dependent and is given by

$$F_i = \sqrt{\frac{x_i}{2\bar{x}}} \quad (1.1)$$

where x_i is the intensity in the i^{th} channel of the true spectrum and \bar{x} is the arithmetic mean of the intensities of the channels in the spectrum. For spectra with a few strong peaks there is still a significant multiplex advantage; however, for weak peaks in a dense spectrum, there is a distinct multiplex disadvantage. Nevertheless, because the overall performance is improved by the product of the multiplex and throughput advantages, the Hadamard technique may still be advantageous.

1.6 Relationship Between Hadamard Spectroscopy and PRBS-TOF Methods

We now illustrate the relationship between the time-modulated data and the Hadamard technique. Figure 1.6 shows a simple TOF spectrum, containing three delta functions. The chopper is opened and closed according to the PRBS sequence. If only the first peak is present in the TOF spectrum, then the signal at the detector is a phase-shifted copy of the modulation sequence. Note that the shift between the response

function, $p(t)$, and the contribution from the first peak, $y_1(t)$, is the time of flight for o_1 . When a second peak is added to the object function, it also generates a phase-shifted copy of the modulation function, where its phase shift is o_2 . The heights of y_1 and y_2 are determined by the intensities of the peaks in the object function. Therefore, the total signal at the detector is the superposition of these signals and, because a single detector is used to collect all particles, the experiment uses multiplexing in the time domain.

The analogy to the weighing experiment can be seen by considering the components that add to any particular time bin. As illustrated in Figure 1.6, the signal in the time bin of $y(t_1)$, is a sum of $1 \cdot o_1 + 1 \cdot o_2 + 0 \cdot o_3$, whereas $y(t_2) = 1 \cdot o_1 + 1 \cdot o_2 + 1 \cdot o_3$ and $y(t_3) = 0 \cdot o_1 + 0 \cdot o_2 + 1 \cdot o_3$. In general, half of the elements of the object function contribute to each channel, but the combinations are different for every channel. The sum can be expressed either as a matrix multiplication, in which the object function is multiplied by the S-matrix:

$$\begin{bmatrix} o_1 & o_2 & \dots & o_n \end{bmatrix} \begin{bmatrix} 1 & 1 & 1 & 1 & 1 \\ 1 & \cdot & \cdot & \cdot & \cdot \\ 1 & \cdot & H_n & \cdot & \cdot \\ 1 & \cdot & \cdot & \cdot & \cdot \\ 1 & \cdot & \cdot & \cdot & \cdot \end{bmatrix} = \begin{bmatrix} y_1 & y_2 & \cdot & \cdot & y_n \end{bmatrix} \quad (1.2)$$

or as a convolution of the object function with the PRBS response function:

$$y(t) = o(t) \otimes p(t) = \int_{-\infty}^{\infty} o(\tau) p(\tau - t) d\tau \quad (1.3)$$

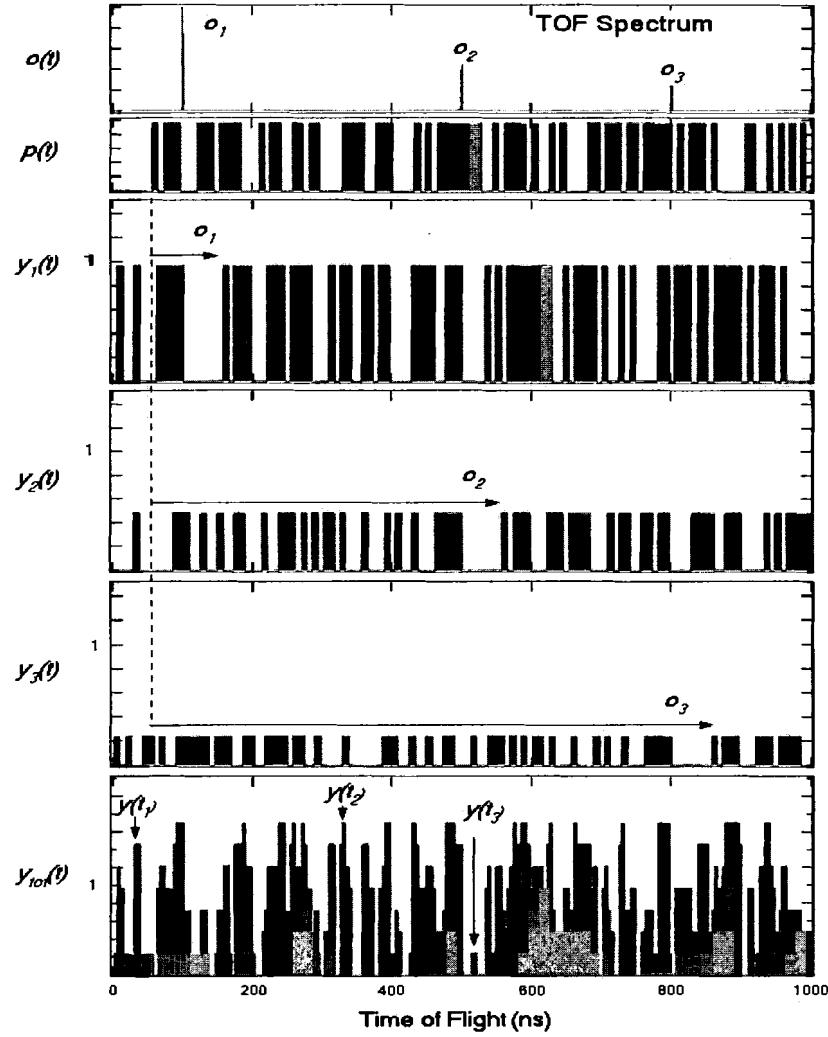


Figure 1.6 Illustration of the relationship between the time of flight spectrum, $o(t)$, the PRBS modulation function, $p(t)$, and the measured data, $y(t)$. A single peak, o_1 , in the TOF spectrum, generates a copy of the modulation function $y_1(t)$ shifted by the flight time (100 ns). Each additional peak in $o(t)$ produces a shifted copy that is scaled by the intensity of the peak in $o(t)$. The total TOF histogram, $y_{tot}(t)$, is a superposition of all of the contributions; in general each time bin is a unique binary combination of the intensities of half of the channels in $o(t)$, which illustrates the analogy of the time domain multiplexing process to the weighing experiments (discussed in the text).

1.7 Maximum Likelihood Methods for Resolution Enhancement

As we have discussed in section 1.4, the Hadamard technique, or PRBS modulation in the TOF approach, suffers a multiplex disadvantage when the standard methods are used for data recovery. A careful analysis, as given by Larson, et al,[62] shows that the correlation between the noise and the signal results in fluctuations that are significantly larger under the pulse counting noise conditions of HREELS. Both the Hadamard matrix multiplication and the cross correlation methods are linear inversion methods that are the correct maximum likelihood solution when the chopper function is ideal and the noise satisfies a normal distribution. However, in our case the noise should have a Poisson distribution, and we anticipate that the finite rise times of the chopper will lead to sufficiently non-ideal behavior, that neither assumption will be satisfactory for the HREELS spectrometer. In fact, finite thickness effects are well understood in molecular beam scattering, and lead to artifacts in the recovered spectrum[64]. An additional factor in the design of the TOF-HREELS instrument is the limitation that the finite rise time places on the minimum pulse width.

Previous work[35] with maximum likelihood and Bayesian resolution enhancement algorithms suggests that, when the noise is Poisson and the response function approximates a square pulse, resolution enhancement by as much as a factor of 6 or 8 can be achieved if the data can be described as a convolution. Therefore, we proposed to use maximum likelihood or Bayesian algorithms to improve the resolution, as well as estimate the underlying TOF spectrum when the noise is Poisson and the shape of the response function is not ideal. We therefore review the properties and assumptions of the maximum likelihood algorithm that will be used in the recovery of data in this

thesis. In traditional spectral restoration work, the point spread function typically has the characteristics of a single Gaussian, a single square pulse, or occasionally a combination of one or two peaks. For example, the contribution of the x-ray source to the measured spectrum in x-ray photoelectron spectroscopy is the sum of two strong, overlapping Lorentzians, as well as four weaker Lorentzian peaks. The instrument has a finite resolution which often has an asymmetric Gaussian shape due to the aberrations of a dispersive energy analyzer. The response function of the instrument becomes approximately a convolution of these two contributions. The point spread function, p , must be determined very accurately for deconvolution to be possible, which has led to much controversy in the XPS literature.

The advantage in HREELS is that the elastic peak provides a good estimate of the shape of the response function, which can be used for resolution enhancement of the loss region, as demonstrated by Frederick, et al[35, 36]. In the proposed TOF-HREELS instrument, the monochromator can potentially be used to measure the chopper's response function. However, we are not aware of any work in which the response function is cyclic and involves multiple pulses, as is the case in PRBS modulation. Thus, we review the behavior of maximum likelihood algorithms for the case of a "simple" response function. In Chapter III we will show that, in fact, we have developed an algorithm that converges and can be used to handle the cyclic data characteristic of PRBS modulation methods.

Consider a measured spectrum, characterized by its intensity distribution $y(t)$, corresponding to the observation of an object spectrum $o(t)$ that has been broadened by the point spread function, $p(t)$, and measured in the presence of Poisson noise, n_i . We

assume that the system is linear and time-invariant, and relate the true object to the collected spectrum via a convolution:

$$y(t) = o(t) \otimes p(t) + n(t) \quad (1.4)$$

In Fourier space we have:

$$Y(\omega) = O(\omega)P(\omega) + N(\omega) \quad (1.5)$$

We want to determine $o(t)$ knowing $y(t)$ and $p(t)$. This inverse problem has led to a large amount of work[65].

In the absence of noise, the data can be transformed to the frequency domain and then divided by the Fourier transform of the response function. In practice, the presence of noise requires some arbitrary filter to be chosen or the ratio will be amplified at higher frequencies as the Fourier transform of $p(t)$ approaches zero:

$$O(\omega) = \frac{Y(\omega)}{P(\omega)} - \frac{N(\omega)}{P(\omega)} \quad (1.6)$$

There are a number of methods that impose restrictions on the solution, such as in the Burg maximum entropy approach[66] in which all features in the object function have the same shape. For a vibrational spectrum[36], this assumption is simply not justified.

There have been a number of iterative approaches [67, 68] that avoid the problems of division in Fourier space and formally acknowledge the Poisson noise in the

data. The Lucy algorithm, maximizes the probability, $P(y|o)$, of obtaining the data, $y(t)$, given an object function, $o(t)$, when the noise has a Poisson noise distribution:

$$P(y_i(t)|o(t)) = \frac{(o(t) \otimes p(t))_i^{y_i} \exp[-(o(t) \otimes p(t))_i]}{y_i(t)!} \quad (1.7)$$

The algorithm used to optimize the object function is an iterative process in which the estimate at o^k is used to generate the next estimate, o^{k+1} :

$$o_i^{k+1} = o_i^k \left(\frac{y(t)}{o(t) \otimes p(t)} \right) \oplus p \quad (1.8)$$

Lucy[67] proved that this algorithm will eventually converge to the likelihood maximum. The method makes no assumptions regarding the shape or number of features in the object function. It is simply a numerical array which, convoluted with the response function, matches the data as well as possible within the Poisson noise. The extent of resolution enhancement depends on the signal to noise ratio in a particular peak, the number of iterations, and the shape and accuracy of the response function itself.

There are, however, disadvantages of this algorithm. When there is a background present, the algorithm will attempt to break the spectrum up into peaks that are not real and in practice the iteration process should be terminated. This is in effect, an arbitrary parameter. More fundamentally, the algorithm is a maximum likelihood algorithm: it optimizes the probability of obtaining the data, given a particular object function and information about the instrument's response function. We would prefer to optimize the probability that a particular object function, $p(o|y)$, is correct, given the data that has been measured. Methods such as the Bayesian maximum likelihood algorithms reported previously[36], have been shown to be reliable for use in HREELS and other

conventional spectroscopies. However, the convergence of the algorithm, when applied to the PRBS modulated data, has proved to be difficult to achieve.

1.8 Organization of the Thesis

In the remainder of this thesis, we give in Chapter II a theoretical analysis of the design of the interleaved comb chopper to first define the optical properties of this device. We discuss both the static and dynamic behavior of the chopper theoretically and verified it experimentally using an HREELS instrument modified for the study. In Chapter III, we first demonstrate the viability of maximum likelihood methods to recover the true object spectrum for an ideal chopper. Then, using simulated data that based upon the work in Chapter II, we present the preliminary indications that indicated that a TOF-HREELS spectrometer could be built based upon the interleaved comb chopper. Chapter IV then presents the design of the first generation PRBST-TOF HREELS spectrometer. In Chapter V, the first measurements are presented, together with a more thorough theoretical analysis and extensive simulation of the PTFE spectrum. We analyze the contributions to the time resolution of the instrument itself, the limitations of the noise and chopper characteristics for the recovery of the spectra, and define the throughput and multiplex advantages of the instrument. Chapter VI presents a summary and discussion of future work. The experimental methods used to prepare the highly oriented polytetrafluoroethylene (PTFE) films and their characterization by AFM and AES is included for completeness in the Appendix.

Chapter 2

APPLICATION OF THE INTERLEAVED COMB CHOPPER TO TOF-HREELS*

2.1 Introduction

A major limitation of commercially available, dispersive sector, electron energy analyzers is that they are inherently serial devices, leading to long data acquisition times, for example in high resolution electron energy loss spectroscopy (HREELS). Several groups have demonstrated that time-of-flight (TOF) methods can be utilized in photoelectron spectroscopy, where the time-base was provided via the pulsed light source of a synchrotron [69-71]. If the electron source is continuous, rather than pulsed, a throughput advantage of order 500-1000 can be achieved by combining TOF methods with pseudo-random binary sequence (PRBS) modulation of the electron beam. PRBS modulation has been widely used with slotted spinning disk choppers for heavy particles, such as in neutron[55, 56] and molecular beam scattering[57]. The development of time-of-flight (TOF) electron spectrometers hinges upon the existence of a fast beam-chopping device. Recently, several authors have demonstrated the use of an interleaved comb of closely spaced wires of equal but opposite voltage to deflect or pass ions in a TOF mass spectrometer [40-42]. The advantage of the “interleaved comb” or Bradbury-Nielson gate as compared to a deflection plate[40] is the much shorter length of the field along the flight direction, which confines the time resolution. We present a theoretical and experimental study, which demonstrates that the interleaved comb can modulate electron beams with sub-nanosecond rise times and discuss the limitations associated with chopper-charged particle interactions.

2.2 Experimental Methods

The construction of an interleaved comb ion deflection gate, first proposed by Loeb[72], has been described by Vlasak[40]. In our work, we fabricated choppers using two different methods as shown in the photograph of Figure 2.1. The first design utilized a circular, laser-cut ceramic disc with two sets of holes spaced 0.3 mm apart. Tungsten-rhenium wire (50 μm) was hand wired to achieve 0.6 mm or 1.5 mm spacing between oppositely charged wires. The two distinct wire sets are electrically isolated from one another by the ceramic plate and terminated on each line with a pair of surface mount 100 Ω resistors in parallel. A second type of chopper fabrication used lithographic methods[73]. Gold 50 ohm microstrip leads were patterned onto polished square aluminum substrates using the lift-off method. Gold wires were then positioned using a jig to align and tension the wires, which were bonded using a parallel gap welder (UNITEK equipment, UNI Bond (II), Model (50F))[73]. With this method, wire diameters of 25, 50 and 100 μm , centered on inter-wire spacings of 250, 500 and 1000 μm , respectively were achieved. The set of three chopper types, all with 90% transmission, were designed to test the dependence of optical properties on the scale of the device.

Figure 2.2 shows a schematic diagram of the system designed to characterize the chopper response, based upon an HREELS spectrometer (McAllister Technical Services, Model PS200, Coeur d'Alene, Idaho) and a custom designed time-of-flight detector. The chopper was mounted at the center of rotation on the face of the monochromator and rotated with it. The electron beam was focused by the monochromator lens through the

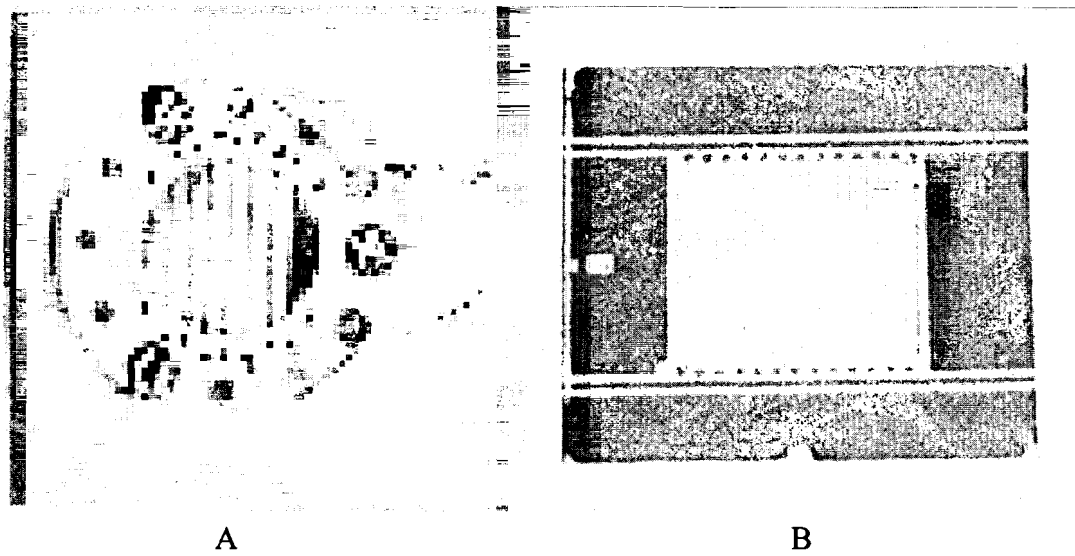
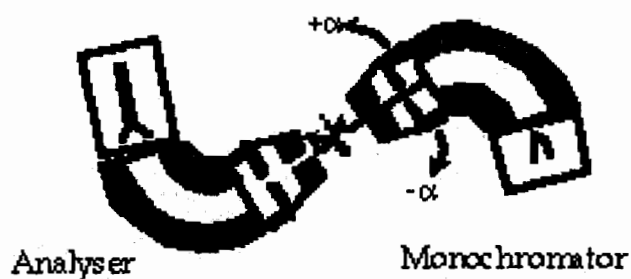


Figure 2.1 The photograph of the chopper made in two methods. Chopper A is the one made by hand wiring to a laser-cut ceramic disk. Chopper B is the one made by using lithographic method.

Into dispersive analyzer:



Into TOF Detector:

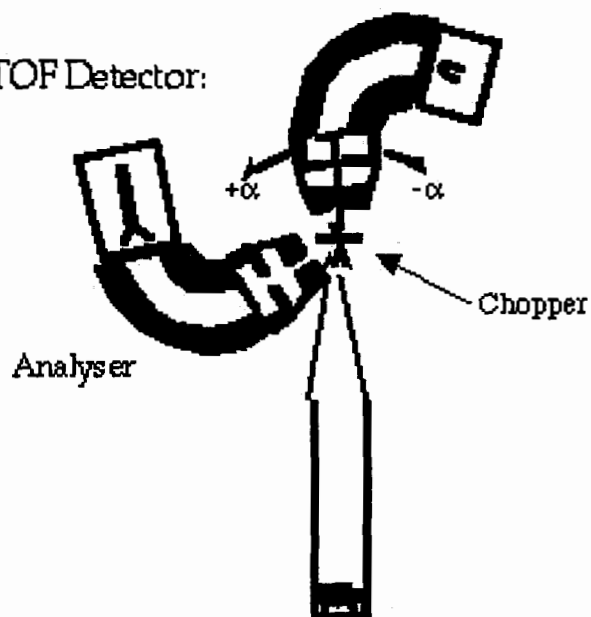


Figure. 2.2 Schematic diagram of the system designed to characterize choppers. The chopper is mounted on the monochromator at the center of rotation and rotates with it to measure, A) energy and angular distributions with the conventional analyzer as a function of the applied static potential, $\pm V_{app}$; and, B) time-dependent response and angular distributions with the TOF detector.

chopper into the analyzer to characterize the energy (typically 10-20 meV FWHM) and angular (typically $\pm 0.7^\circ$) distributions of the incident electron beam. When static potentials were applied to the chopper, the monochromator was rotated by a stepper motor under computer control to measure the angular distribution of the deflected beams. Data acquisition and control were performed using a SPECTRA card (Ron Unwin, Cheshire, UK) customized with a user-written dynamic link library (DLL). When the monochromator was rotated so as to direct the beam into the TOF detector, a modulated signal was applied to the chopper grid and the time-dependent response was measured. The TOF detector was based upon a micro-channel plate detector (AP-TOF, Gallileo Corp., Sturbridge, MA) which was custom-modified for negative particle detection.

2.3 Theoretical Model

We first present a two-dimensional analytical potential, based upon a conformal mapping of an infinite, periodic set of infinitely long, line charges $\pm\lambda$, as illustrated in Figure 2.3A, onto two line charges, illustrated in Figure 2.3B. In real space (Fig. 2.3A), wires of diameter $2R$ and alternating potential, $\pm V_{app}$, are spaced along the y -axis with a periodicity, d . Electrons passing in the positive x direction would be deflected in the $\pm y$ directions. In real space, let $\alpha = x + iy$. Using the complex transformation, $\eta = \exp\left(\frac{\pi}{d}\alpha\right)$, the line charges alternately map onto the points $(0, \pm i)$ in the η space (Fig. 2b) for which the potential is well known. The infinite chopper potential is then

$$\psi(x,y) = \frac{\lambda}{2\pi\epsilon_0} \ln \left[\frac{\cosh\left(\frac{\pi x}{d}\right) + \sin\left(\frac{\pi y}{d}\right)}{\cosh\left(\frac{\pi x}{d}\right) - \sin\left(\frac{\pi y}{d}\right)} \right]. \quad (2.1)$$

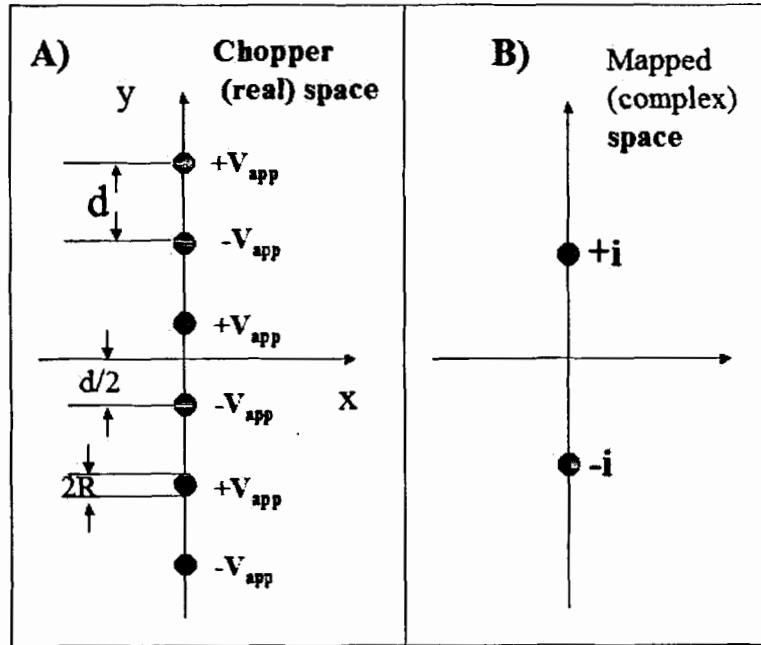


Figure. 2.3 A) Model for an infinite array of infinitely long wires of radius, R , and spacing, d , in the $x=0$ plane, with alternating potential $\pm V_{app}$. B) The two-wire problem obtained by by conformal mapping.

The contours of this potential in the real space are nearly circular close to the line charges. Thus, for finite diameter wires with $R \ll d$, *i.e.* near unity transmission, the line charge solution well approximates the actual chopper potential and we need only choose a point through which the potential passes to define the line charge λ . Choosing the point $(x = 0, y = d/2 - R)$ to have a potential V_{app} we have

$$\lambda = \frac{2\pi\epsilon_0 V_{app}}{\ln \left[\frac{1 + \cos\left(\frac{\pi R}{d}\right)}{1 - \cos\left(\frac{\pi R}{d}\right)} \right]} \quad (2.2)$$

The potential (see Fig. 2.6 below) is simply proportional to V_{app} , and has the important feature that it decays as $\psi \sim 4\lambda \exp\left(-\frac{\pi|x|}{d}\right)$, such that the potential is reduced to <3% of eV_{app} within the first d spacing, and is $<10^{-5} eV_{app}$ within $3.6 d$. For V_{app} of order 1V, the potential for $x > 3.6d$ is small compared to the typical (~ 2 meV) energy resolution of the monochromatic beam in HREELS.

Trajectory calculations were performed numerically using an adaptive, 4th order Runge-Kutta method (MathCad v. 6 and 2000, Mathsoft) with initial positions chosen randomly in a region of negligible potential to the left ($x < 0$) of the chopper plane. The distribution of angular deflection was determined from the final angle after the electron leaves the field affected region ($\psi < 10^{-5} V_{app}$). To simulate time-dependent changes in chopper potential, trajectories were calculated either in free space or over the applied potential, assuming that the potential was changed instantaneously, until the electron was in a region of negligible potential. For comparison with experimental data, flight times

were calculated from the final position and velocity to the detector at a chopper-to-detector distance of 16 cm.

2.4 Experimental Results

In Figure 2.4 A, we compare the angular distribution of the deflected electrons as a function of the applied potential using the TOF detector. Similar results were obtained with the dispersive analyzer. For small deflection angles and a beam size large compared to the wire spacing, d , the beam is split into a symmetric distribution, peaked at angles $\pm\theta_{\text{def}}$, which is approximately linear in the ratio of the applied potential to the electron's kinetic energy, $eV_{\text{app}}/\text{KE}$. The modulation of the beam is clearly dependent upon both the angular distribution of the incident electron beam and the deflection angle. For an acceptance angle of $\pm 1^\circ$, 99.9% modulation is easily achieved under static DC applied potentials. As expected, the deflection angle is independent of the wire d spacing, for constant transmission, or R/d ; *i.e.*, as the chopper geometry is scaled to smaller dimensions, the applied voltage *must remain constant* to achieve the same deflection angle.

The time-dependent response, illustrated in Figure 2.5 for the $2R=100\ \mu\text{m}$ chopper, was measured for a range of applied voltages with an incident 5 eV beam having an angular distribution of $\text{FWHM} = 1.5^\circ$. The potentials were periodically dropped to zero for approximately 100 ns (period of 700 ns; rise/fall times of 1.5 ns), during which time the undeflected beam was accepted through an aperture of half acceptance angle $\theta_a = 1.5^\circ$. The number of counts in each histogram varied with acquisition time, but are shown as counts to allow the noise level to be compared with that expect from the Poisson distribution. The TOF histograms, sampled on 250 ps time

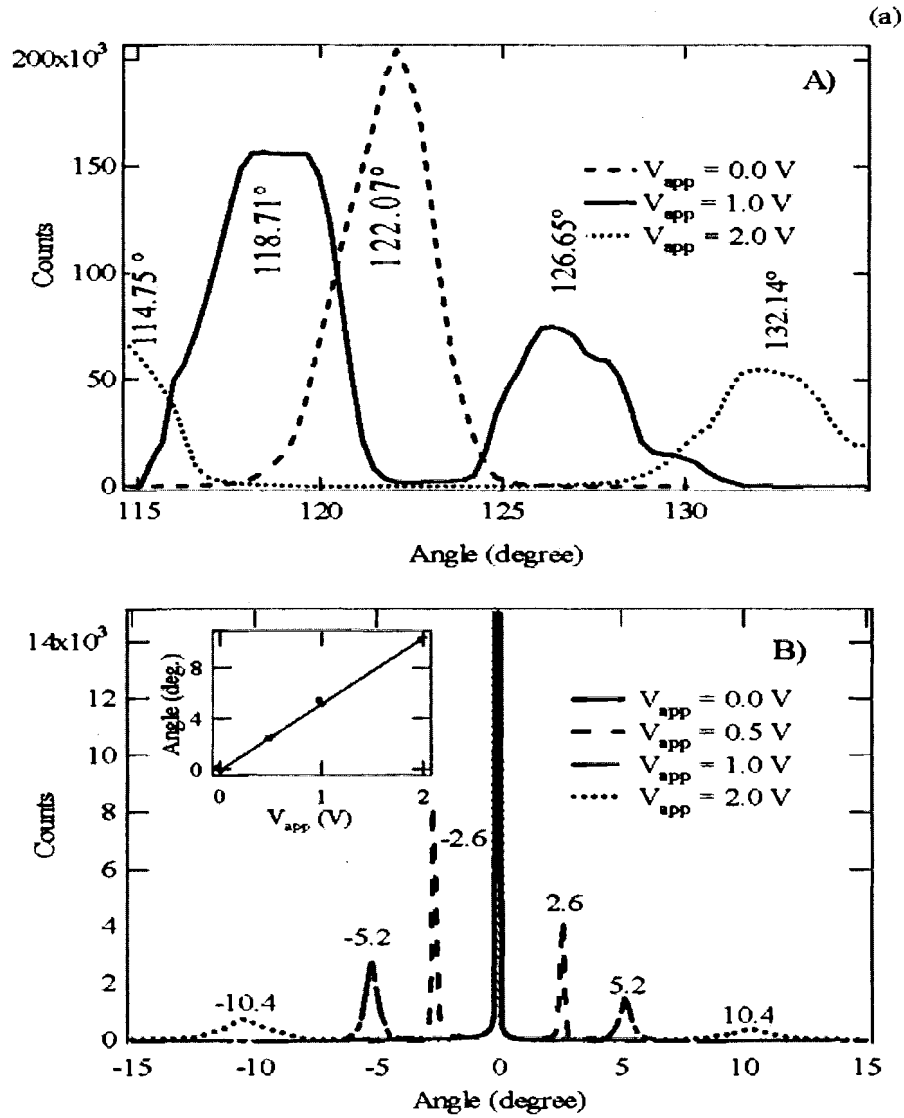


Figure. 2.4 A) A typical angular distribution, measured with the TOF detector, for a 5 eV beam as a function of the static DC voltage, V_{app} , applied to the chopper. (B) Theoretical angular distributions for a uniformly distributed (see text) beam of electrons ($E_p = 5\text{ eV}$) as a function of applied voltage, V_{app} , from trajectory calculations. Inset compares the experimental and theoretical peak deflection angle as a function the ratio V_{app}/KE . Wire radius, $R = 25\text{ }\mu\text{m}$; wire spacing, $d = 1.2\text{ mm}$; flight distance 160 mm; acceptance angle $\pm 1^\circ$; angular bin size = 0.1° .

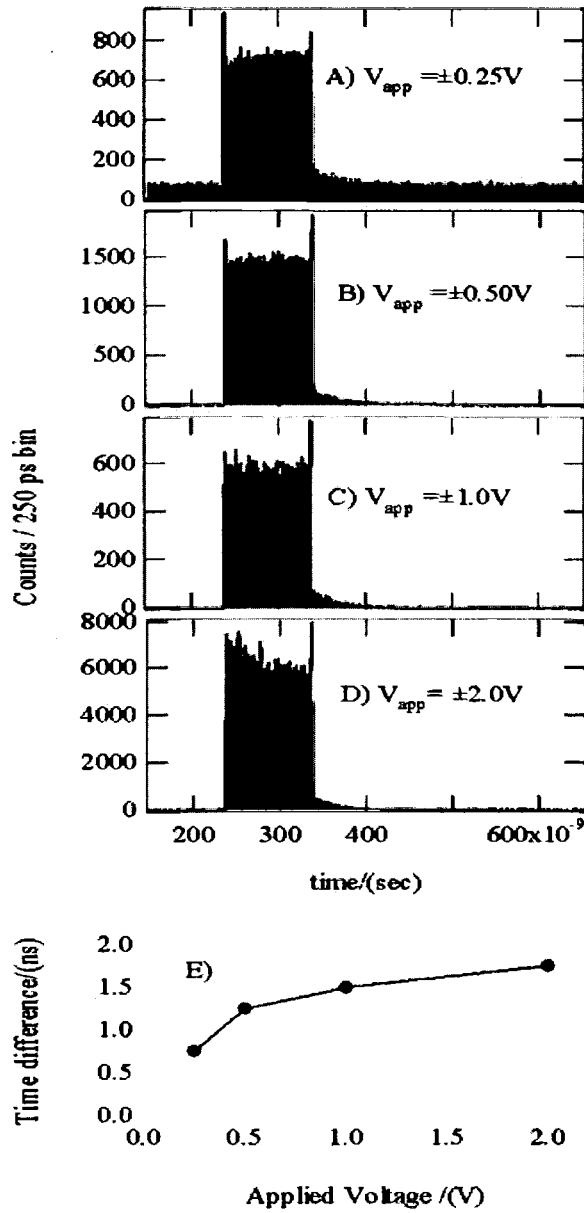


Figure 2.5 The time-dependent response of a $2R = 100 \mu m$, $d = 1 mm$ chopper to a 5 eV beam as a function of the chopper potential, V_{app} (A) 0.25 V, (B) 0.5 V, (C) 1.0 V, and (D) 2.0 V, for an acceptance angle of $\pm 1.5^\circ$. (E) The difference between the time that the beam is on and the time (~ 100 ns) that the chopper voltages are off. Both of these times are measured using the appropriate half heights.

bins, show that rise times of <0.5 ns are easily achieved. However, several features of the TOF spectra should be noted. First, the histograms display peaks and tails at the times when the chopper changes state that are significant compared to the Poisson noise distribution. Second, a detailed comparison of the time that the potentials are off and the time that the beam is on shows that the difference varies with applied voltage: the electron beam turns on late and/or shuts off early. The dependence is shown in Fig. 2.5 E. Third, while the background on the high energy side (shorter flight times) for $V_{app} > 0.5$ V is less than 10^{-5} of the average count rate when the gate is open, significant intensity with a distribution to lower energy appears with a relative intensity of 10^{-2} , which is attributed to inelastic scattering from the relatively thick apertures placed before and after the chopper. The origin of the first two features is discussed in light of the theoretical simulations presented in the following section.

2.5 Theoretical Simulation Results and Discussion

We first compare the angular distribution of the transmitted beam (Fig. 2.4A) with simulations based upon trajectory calculations. Electron positions were chosen randomly within the region ($-40\text{mm} < x < 40\text{ mm}$, $-1.8\text{mm} < y < 1.8\text{ mm}$). The potentials were applied for the first 8 ns, during which time the first electrons enter the field-affected region. The potentials were then turned off for 8 ns, on again for 8 ns, and finally turned off to calculate the final angle and the time in the field-free flight tube to reach the detector. Figure 2.4B shows the angular distributions calculated for the infinite chopper corresponding to the geometry of the ceramic disk design as a function of V_{app} . The results show that, for uniform filling of the chopper, the deflection angle in the angular distribution increases proportional to V_{app} , and as shown superimposed in the inset of fig.

2.4B, agrees quantitatively with the experimental measurements. Whereas the electrons in the simulation have initial velocity parallel to the x-axis, the angular distribution in the experiment leads to broader peaks in the angular distributions of Fig. 2.4A.

The results of simulations of the time-dependent response are shown in Figure 2.6. The flight times, for electrons accepted by an aperture of $\pm 1^\circ$ at a flight distance of 160 mm, are shown as a function of V_{app} in Fig. 2.6 a, b and c, and as a function of the wire spacing (for constant R/d) in Fig. 2.6 d, e, and f. While the beam is modulated as expected, turning the beam on then off and on again, several features noted in the experimental data are reproduced in the simulations. First, at the transitions, the simulations predict spikes and tails in the histograms which deviate significantly from the Poisson noise distribution. Second, the chopper response (here, the time-dependent beam current) has a lag or lead with respect to the applied voltage making it appear that the gate is open for times less than the 8ns used in the calculation and closed for times greater than 8 ns. These effects depend upon V_{app} as well as the scale of the chopper (*i.e.* the wire spacing for constant R/d). Reduction of the applied voltage or reduction of the wire spacing noticeably decreases these effects. We note that late opening and early closing of the gate is analogous to the effect of finite thickness investigated by Zeppenfeld [64] for spinning disk mechanical choppers.

The origin of the spikes and tails can be understood from consideration of trajectories over the potential, shown in Fig. 2.7. Consider first an electron approaching the chopper with potentials off (gate open). If an electron is near the gate and the potential is applied instantaneously, the electron may gain or lose potential energy, depending upon whether it is closer to a negative or positive wire, respectively. For

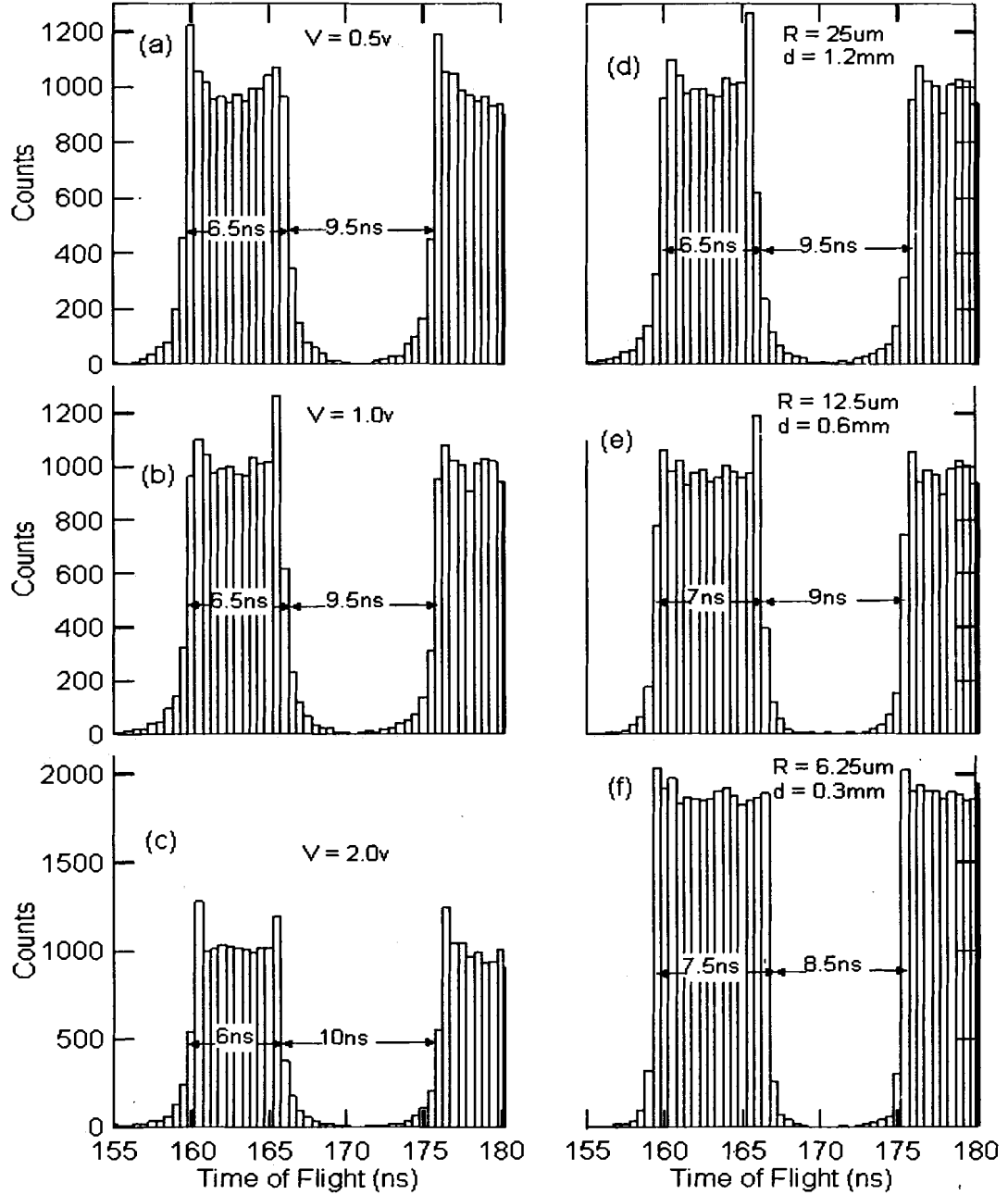


Figure 2.6 Calculated time-dependent response as a function of applied voltage, V_{app} (a) 0.5 V, (b) 1.0 V and (c) 2.0 V, and as a function of wire spacing (d, e, and f) at constant R/d (*i.e.* constant transmission) for $V_{app} = 1.0$ V. The peaks and tails, due to energy corruption, as was lag and lead effects, decrease with V_{app} and with d .

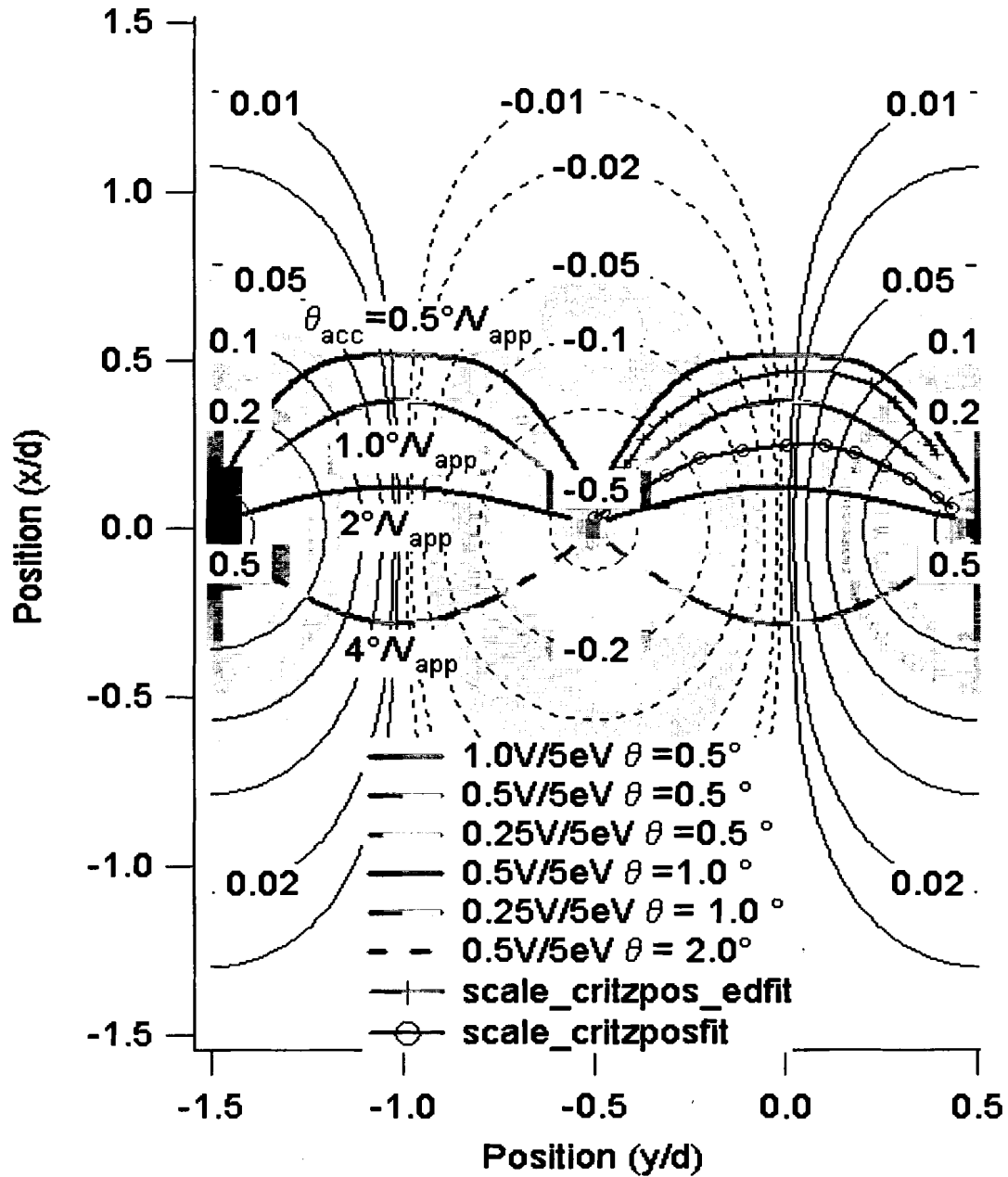


Figure 2.7 Contour map of the potential, $\psi(x,y)$, with critical boundaries, $f(x,y, \theta_{acc}, V_{app})$, as a function of the acceptance angle and applied voltage. If the electron is at position (x_0, y_0) beyond the boundary at the time when the potential is applied, the electron has final angle $\theta_f < \theta_{acc}$; i.e. the electron reaches the detector, and suffers an energy corruption $e\psi(x_0, y_0)$.

electrons in the field affected region, it is necessary to compute trajectories to determine whether sufficient transverse field exists over the subsequent path to exclude the electron from the detector. Clearly, this is dependent upon the applied voltage and the acceptance angle of the aperture. The curves in figure 2.7 represent critical boundaries, $f(x, y, \theta_{acc}, V_{app})$, such that if the electron is beyond the curve at the time the potentials are applied, the electron has final angle $\theta_f < \theta_{acc}$; *i.e.* the electron reaches the detector. For those electrons which reach the detector, their energy has been changed, or corrupted, by an amount given by the potential at the position of the electron when the potential was changed. Thus, there is a distribution of "energy corruption", ranging from $-V_{app}$ to V_{app} . The symmetry of the potential shows that, for a uniformly distributed beam of electrons, the probability of gaining energy is equal to that of losing energy, producing both longer and shorter flight times in the TOF histogram. Therefore, the step function response of the chopper is modified, producing the spikes and tails, which we attribute essentially to these energy corruption effects. As V_{app} is decreased, the maximum energy corruption decreases, and the magnitude of the spikes and tails in the simulations decrease.

The energy corruption effect can be distinguished from a second effect, noted in both the experimental and simulation data, that there may be a lead or lag in the beam current with respect to the times that the potentials are changed. Consider an electron approaching the gate, with $V_{app}=0$, along the mirror symmetry plane, $x = 0$, such that $\psi(x=0, y) = 0$. For this trajectory, the energy corruption effect is zero, since the electron is still at zero potential immediately after the voltages are applied. It propagates over some trajectory until leaving the field affected region, where again the potential is zero. However, depending upon the acceptance angle of the detector, the electron may or may

not be detected. If the acceptance angle is small, e.g. $0.5^\circ/V_{app}$, only electrons that have passed the plane of the chopper (by approx. $1/2 d$ in this example), reach the detector: the chopper appears to close early. By contrast, for large acceptance angles, electrons in a small region before the gate (e.g. $y \geq -0.3d$ for $\theta_{acc} = 4^\circ/V_{app}$), still reach the detector and the chopper appears to close late.

Examination of the boundaries for several combinations of V_{app} and θ_{acc} reveal that, since the deflection is approximately linear in the applied voltage for small deflection angles, the boundaries are a function of the ratio θ_{acc}/V_{app} , as indicated in the figure. Likewise, a scaling argument reveals that, for constant R/d ratio, the trajectories are the same if the electron enters from the field free-region independent of wire spacing, d , as long as the kinetic energy and applied voltage are constant. This implies that the deflection angle is only a function of the ratio eV_{app}/KE for the static chopper potential. Therefore, the information about the boundaries in Figure 2.7 summarizes everything that can be known about the time dependant optical properties of the chopper, within the approximation of a single, instantaneous change in chopper potential. Examination of trajectories corresponding to the reverse process, namely electrons approaching the gate with the potential applied and then turned off while in the neighborhood of the chopper, shows that the boundaries are essentially just the mirror image about the plane of the wires and the effects on the time lead or lag mirror the previous case: if for a small acceptance angle the beam turns off early, then it turns on late.

Since the energy corruption depends simply on the position of the electron when the potential is switched, the distribution of energy corruption for a given region of space near the chopper can be extracted simply as a histogram of the potential values (for

electrons in the region which reach the detector). In Chapter III, we utilize this potential to simulate the effects of energy corruption and lead/lag in beam response on TOF spectra for applications in HREELS.

2.6 Conclusions

We have shown that for near unity transmission, trajectory calculations on the potential derived from a conformal map agree well with experimental measurements characterizing both the static deflection and time-dependent response of the chopper, suggesting that this potential is a useful limiting-case description of the interleaved comb device. The finite penetration of the field beyond the plane of the chopper leads to non-ideal chopper response, which is characterized in terms of an energy corruption effect and lead or lag in the time at which the beam responds to the chopper potential.

Chapter 3

ADVANTAGES OF MAXIMUM LIKELIHOOD METHODS FOR PRBS

MODULATED TOF ELECTRON SPECTROMETRY

3.1 Introduction

Despite dramatic advances in the energy resolution and throughput of electron monochromators [12, 13] for high resolution electron energy loss spectroscopy (HREELS), a major limitation of conventional, dispersive sector, electron energy analyzers is that they are inherently serial devices, leading to long data acquisition times. The advantage of higher resolution leads to trade-offs in performance (throughput) because channel step size must be reduced, and therefore increasing the number of channels required to measure a given spectral region. Using a multi-channel plate detector to ameliorate this problem is one possibility. Indeed, time-resolved HREELS measurements have been demonstrated with a multi-channel plate in the dispersive plane of a conventional analyzer [46]. However, parallel detection can be accomplished in this way only over a limited spectral range without degrading resolution. Thus, development of an analyzer based upon parallel detection would benefit both typical spectral investigations and allow new experiments to be performed, such as recent inelastic diffraction experiments which are both momentum and energy resolved [74].

A throughput advantage of order 500-1000 can be achieved by combining time-of-flight (TOF) methods with pseudo-random (PRBS) modulation of the electron beam. In Chapter II [75], we examine the performance of an "interleaved comb" chopper for secondary modulation of an electron beam to provide a nanosecond timebase for time-of-flight (TOF) measurements. This shows that the electron beam can be modulated with

rise and fall times of less than a nanosecond, which corresponds to 3 meV energy resolution for 2 eV energy electrons. The finite penetration of the fields associated with this electrostatic device of course produce certain non-ideal behavior, which we characterize in terms of an "energy corruption" effect and a lead or lag in the time at which the beam responds to the chopper potential. Here, we present simulations of PRBS modulated TOF data. We examine, for the first time, the use of maximum likelihood methods to recover the underlying TOF spectrum [76]. We find that, compared to the standard cross correlation method, i) the resolution is improved relative to the nominal time base resolution of the PRBS sequence; ii) the Poisson (pulse counting) noise is accounted for; and iii) artifacts associated with imperfections of the chopper performance are reduced.

3.2 Theoretical Background

Pseudo-random binary sequences, also known as maximal length shift register sequences [58, 59], for modulation of photon and particle beams have been widely used in time-of-flight techniques applied, for example, to neutron scattering [55, 56], molecular beam scattering [57, 77] and ion mass spectroscopy [42, 78]. The PRBS-TOF method achieves a throughput advantage over single pulse TOF due to the 50% duty cycle of the PRBS sequences. In the experiment, the underlying TOF spectrum (the object spectrum, o) is modulated with the PRBS sequence, p , resulting in a periodic, time sequence, $(p \otimes o)$. In the standard cross-correlation method, an estimate of the TOF spectrum, r , is recovered by correlating the data with the PRBS modulation sequence, p : $r = p \oplus (p \otimes o)$. Here, \otimes and \oplus denote convolution and correlation, respectively. A special property of PRBS sequences is that the autocorrelation of the discrete sequence p

is a delta function; therefore, the recovered spectrum, r , is identical to the original object spectrum, o . In reality, the modulation function is continuous, but r is an estimate of o as long as the time base (minimum pulse width) of the modulation function is small compared to the linewidth of the narrowest features in o . If this is not the case, then the throughput advantage is gained at the expense of resolution in the recovered spectrum, and over-sampling of the modulated signal, $(p \otimes o)$, leads to a recovered spectrum which is the autocorrelation $(p \oplus p)$ (roughly, a triangular pulse) convoluted with the object function: $r = (p \oplus p) \otimes o$. A segment of an ideal PRBS sequence is shown in Figure 3.1 (curve a), together with its autocorrelation function (curve b). If the chopper is open (1) or closed (0) for the duration of a time step, τ , and the signal over-sampled (here 16x), then the autocorrelation is a triangular pulse with base 2τ . We note that for finite, linear rise and fall times, if the duty cycle is still 50%, as shown in curve c, the autocorrelation function (curve d) becomes rounded, but approaches zero smoothly without artifacts.

The problems that arise in applying the charged particle gate, known as the "interleaved comb"[40], to PRBS modulated TOF mass spectrometry have been recognized by Zare [41, 42]. In an accompanying paper, we examine in greater detail the artifacts that are introduced for electron spectroscopy [75]. Three effects can be distinguished:

- i) The "dead time" associated with the time for electrons to cross the field affected region leads to an error in the time at which the beam turns on and off. When the PRBS sequence (Fig. 3.1, curve e) differs from a 50% duty cycle, the autocorrelation function (curve f) contains oscillations in the baseline and negative artifacts. This effect is analogous to the effects of machining errors and the finite thickness of mechanical

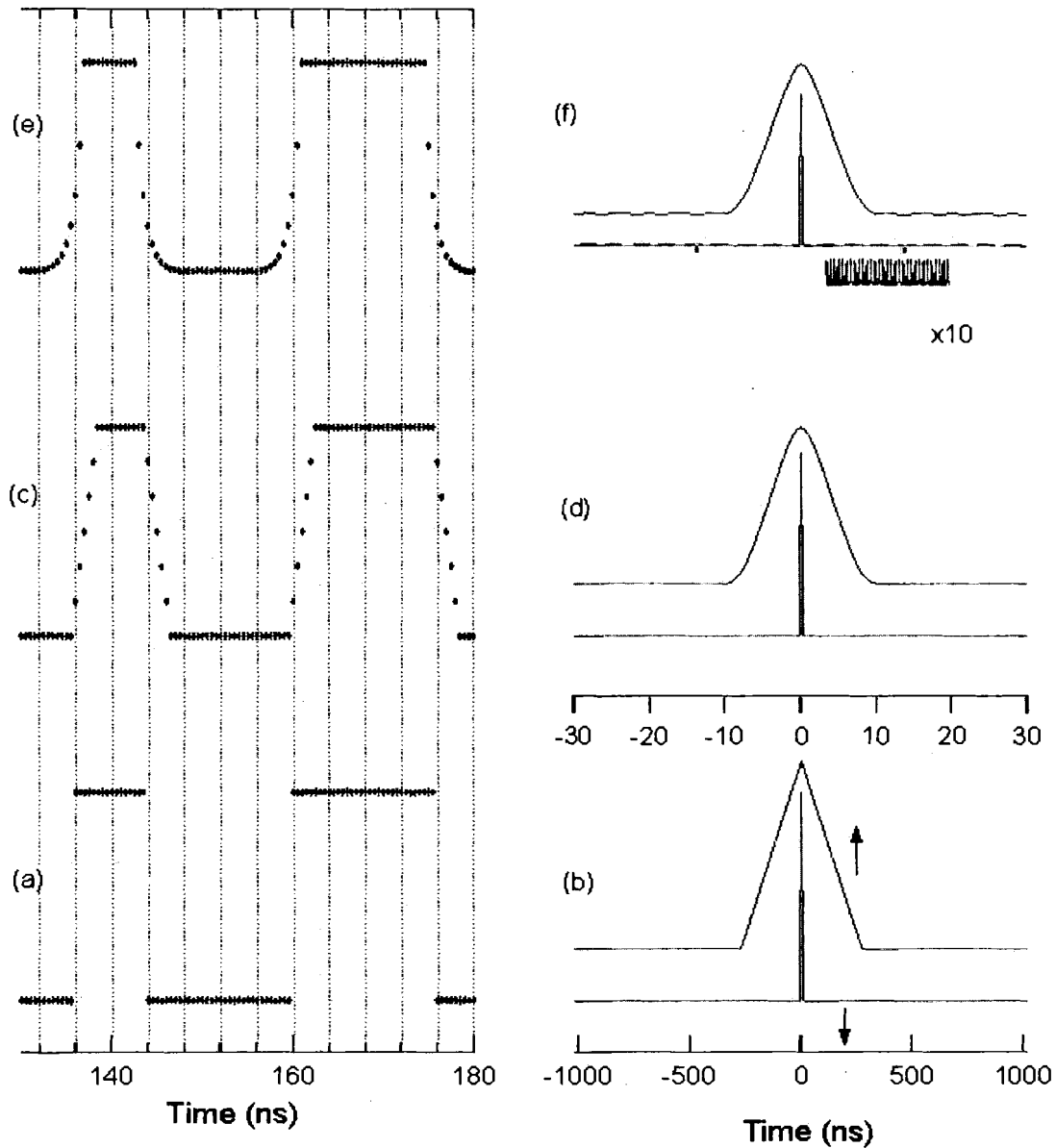


Figure 3.1 Illustration of the non-ideal chopper response on the autocorrelation function: a) segment of an ideal 2^8-1 bit PRBS sequence which is over sampled by a factor of 16 and b) its autocorrelation function; c) the effect of a linear rise time on d) the autocorrelation function; and e) the effect of exponential rise and fall times with a duty cycle less than 50% producing artifacts in f) the autocorrelation function. Central section of each autocorrelation function expanded to show peak shape.

chopper disks, used for example in molecular beam scattering [64]. These negative artifacts can be assessed from the autocorrelation of the (imperfect) PRBS sequence, and removed *a posteriori* [64], although the effects of the finite disk thickness lead to a velocity dependent error.

ii) The interaction of charged particles with an electrostatic gate causes a change in the energy of the particles when the potentials are switched. The change in energy, which we term "energy corruption"[75], leads to degradation of the information carried by the charged particle, i.e. its energy or velocity, which is the quantity measured in TOF spectrometry. Because the corruption depends upon the position of the electron, relative to the plane of the chopper, at the time the potential is switched on or off, a statistical distribution of energy corruption can be determined directly from the potential for spatial regions as a function of the distance from the chopper.

Figure 3.2 shows energy corruption histograms for regions corresponding to the distance traveled in 0.5 ns time steps for a 2eV electron beam by an interleaved comb chopper with wire spacing of 1.2 mm and radius 25 μm with applied voltages of ± 0.4 V and an analyzer acceptance angle of $\pm 1^\circ$. From these results, it is clear that the energy corruption is large compared to the energy resolution of modern HREELS monochromators for the first 2-3 ns before or after switching the potentials. Since during the first 2 ns and last 2 ns of a pulse the energy distribution is heavily corrupted, the fraction of the pulse in which "good" information is obtained is $(\text{pulse width} - 4 \text{ ns})/(\text{pulse width})$. Thus, reducing the time base of the PRBS sequence below about 8 ns (for this chopper) significantly degrades the effective resolution of the analyzer for the affected electrons. However, energy corruption is introduced only at the beginning and

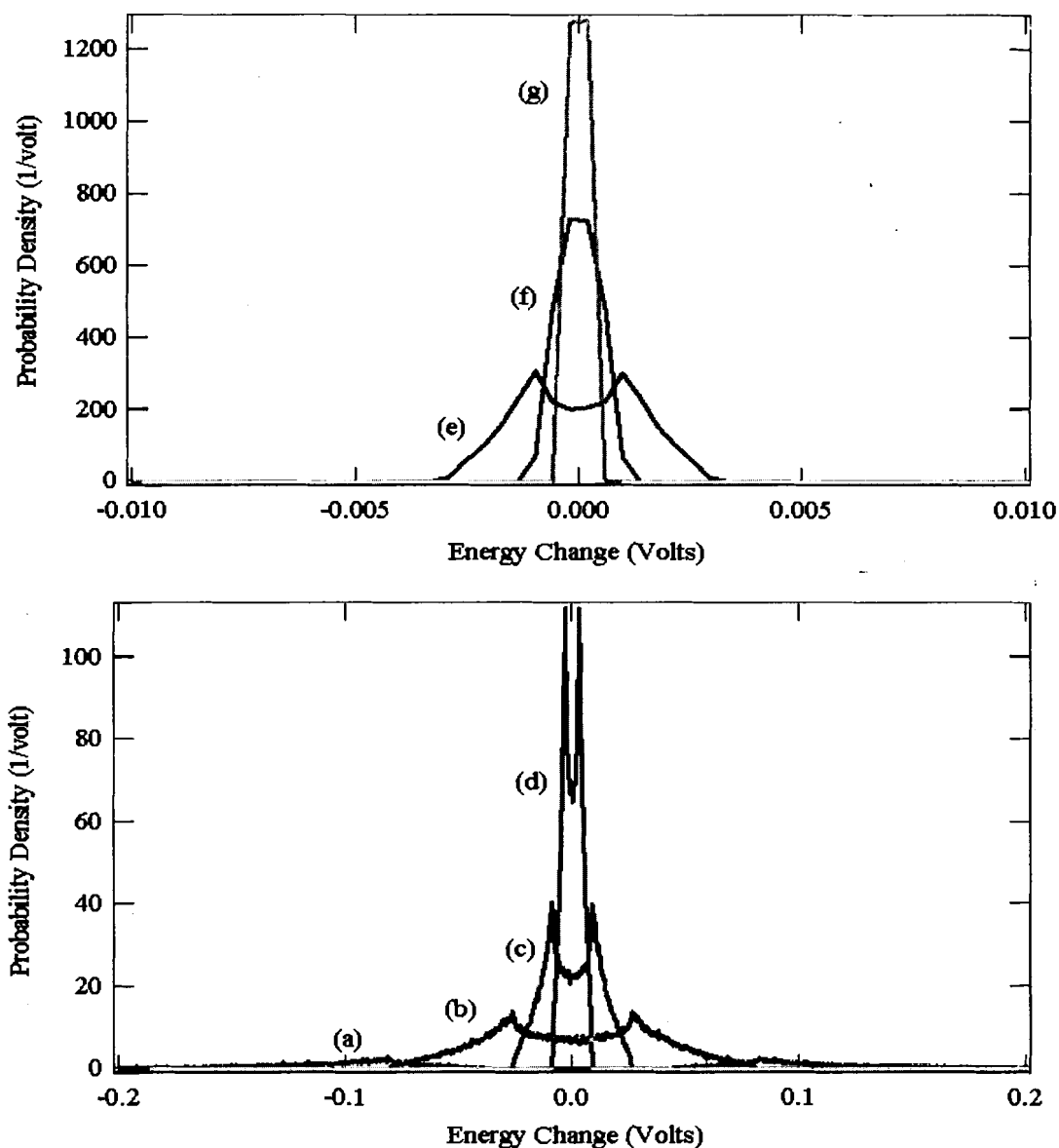


Figure 3.2 Energy corruption histograms for a 2 eV electron as a function of distance from the chopper or, alternatively, time of arrival at the plane of the chopper before or after the potentials are switched. Histograms obtained via a Monte-Carlo sampling of the model potential [75] for 2 eV electrons arriving at the chopper within the time intervals a) 0-0.5ns, b) 0.5-1 ns, c) 1-1.5 ns, d) 1.5-2 ns, e) 2-2.5 ns, f) 2.5-3 ns, and g) 3-3.5 ns.

end of multiple 1's in the PRBS modulation sequence, i.e. when the chopper voltage is changed. There are 2^{n-1} edges in a sequence of length 2^n-1 [64], so the fraction of electrons which pass the chopper un-corrupted depends upon the time base, τ , but is about 50% less than would be the case for a single pulse TOF experiment. Our on-going research, to be reported elsewhere, shows that the energy corruption and other artifacts introduced by this chopper can be significantly reduced by improved chopper design.

iii) If the detector is limited by quantum counting processes, as is the case with photomultipliers or electron multipliers operated in a pulse counting mode, and sometimes with continuous (analog) amplifiers, then the correlation between the noise and signal power spectra leads to artifacts in the cross-correlation recovery method. This effect is known as the "Multiplex Disadvantage". These artifacts arise from using least squares methods, or more precisely, the assumption that the autocorrelation of the noise is zero, which is true for Gaussian distributed, but not Poisson distributed noise. Maximum likelihood inversion methods, for example as applied to Fourier Transform IR spectrometers [79] and previous work in deconvolution of conventional HREELS data [36], can overcome this noise limitation.

3.3 Simulation of PRBS Modulated TOF Data

Define the chopper response function, p , as the effect of the time-dependent chopper potentials on the detected electron beam current. More precisely, p is the chopper transmission function, $p(t) = I_{\text{det}}(t) / I_0(t)$. For the data described in this paper, p is given by a 255 bit (2^8-1) PRBS ("shift register") sequence, with either an ideal step function response, or including one or more of the artifacts described in Sect. 2. Data were generated with the PRBS time base of $\tau = 8$ ns, and oversampled by factors of 8, 16

or 64, corresponding to detector time bins of 1 ns, 0.5 ns, and 0.125 ns, respectively. A typical HREELS loss spectrum was simulated with a Gaussian elastic peak ($E_p = 2$ eV; FWHM = 2 meV; 100 kCts/s) and a set of smaller Lorentzian peaks of relative intensity 0.1-10% and FWHM 3 meV, representing inelastic gains and losses. Several doublets, whose separation was greater than or equal to their FWHM, were included to test the resolution enhancement capabilities. Previous experience with the Bayesian/maximum likelihood algorithms [35] indicates that two peaks must be separated by at least their FWHM to be resolvable. One asymmetric lineshape and a feature in the tail of the elastic peak were also included to test the ability of the deconvolution algorithms to distinguish overlapping peaks from asymmetric ones.

To generate PRBS modulated, time-series data, $(p \otimes o)$, the following procedure was followed. The kinetic energy distribution (energy loss spectrum) was converted into a TOF distribution, $o=N(t)$, with an integer number of counts in each of the discrete flight time bins (note that the object function is defined in the time domain, not the energy domain). A probability function, $f(t')$, was generated by creating a cumulative sum of counts over the array of flight times, $f(t') = \int_0^{t'} N(t)dt$. The probability function, $f(t')$, represents a look-up table, such that a random number chosen over the domain of f implies a flight time, t . To include energy corruption effects, each of the eight energy corruption histograms, corresponding to the seven energy corrupted spatial regions of Fig. 3.2 and the uncorrupted distribution, were convoluted with the original energy distribution before being converted to TOF distributions.

For a beam current of 100 kCts/s, the probability of detecting one electron per PRBS cycle is, in this simulation, $(10^5 \text{ s}^{-1})(255 \text{ bins / cycle} \times 8 \text{ ns / bin}) = 0.2 \text{ / cycle}$.

This shows that the noise should obey Poisson statistics and indicates that accumulation over millions of PRBS cycles is required for sufficient signal to noise to recover the object spectrum. Simulated data was produced by cycling through the response function, p , where on each time step, i , $p(i)$ ranged between 0 and 1. If $p(i)$ was greater than a random number between 0 and 1, the gate was "open" and the electron's flight time, t' , was chosen randomly from $f(t')$. (Because the probability of selecting any one flight time from the distribution is small, a plot of the variance of the number of counts in each channel, for a single pulse TOF spectrum, was equal to the average count rate in each channel, demonstrating that a Poisson noise distribution was obeyed.) Then to generate PRBS modulated data, a count was added to the channel corresponding to the flight time plus the position in the modulation sequence, p . If the channel number exceeded the length of the sequence, the value was wrapped around by the PRBS sequence length (8, 16 or 64 times 255). The process was continued, cycling through p until the desired number of total counts was recorded, producing data sets with 2 million to 256 million counts (MCts).

3.4 Results of Cross Correlation vs. Maximum Likelihood Recovery

We now compare the results of the standard cross correlation method with a maximum likelihood deconvolution. The cross correlation method [21] was performed in MatLab (MathWorks, Inc., 5th ed., Natick, MA) , resulting in a recovered spectrum, $r = (p \oplus p) \otimes o$. A maximum likelihood estimate of the object function, o , was obtained from the modulated data, $(p \otimes o)$, using the well known, iterative LUCY algorithm [67, 80] described previously [36]. The Lucy algorithm maximizes the probability, $P(y|o)$,

of obtaining the data, $y = o \otimes p$, given an object function, o , for a Poisson noise distribution:

$$P(y_i | o) = \frac{(o \otimes p)_i^{y_i} \exp \{-(o \otimes p)_i\}}{y_i!} \quad (3.1)$$

by an iterative process in which the estimate at o^k is used to generate the next estimate, o^{k+1} :

$$o_i^{k+1} = o_i^k \left(\frac{y}{(o \otimes p)} \right) \oplus p. \quad (3.2)$$

For deconvolution of the PRBS modulated data, the initial guess was obtained from the result of the cross correlation method, r , and a prime factor transform was utilized instead of the usual FFT algorithms, since the sequence length is not a power of 2. Because the PRBS modulated data is periodic (edge effects associated with the start of data acquisition are or can be made negligible), no packing of the array is required.

Consider first the effects of the Poisson noise distribution on the cross correlation method. Figure 3.3 compares the object spectrum with the spectra from a single pulse TOF experiment (broadened by the 8ns gate time) and that recovered from a PRBS modulated experiment. The PRBS modulated data was generated using the ideal, step function sequence for p and the object function, o , shown. The single pulse TOF spectrum, generated with a square gate function of 8ns duration, results in degraded resolution and poor signal/noise compared to the PRBS recovered data. Despite the fact that the cross correlation method is not strictly valid due to the Poisson noise distribution, the method works reasonably well, presumably since the Poisson noise distribution approaches a normal distribution for sufficiently large count rates.

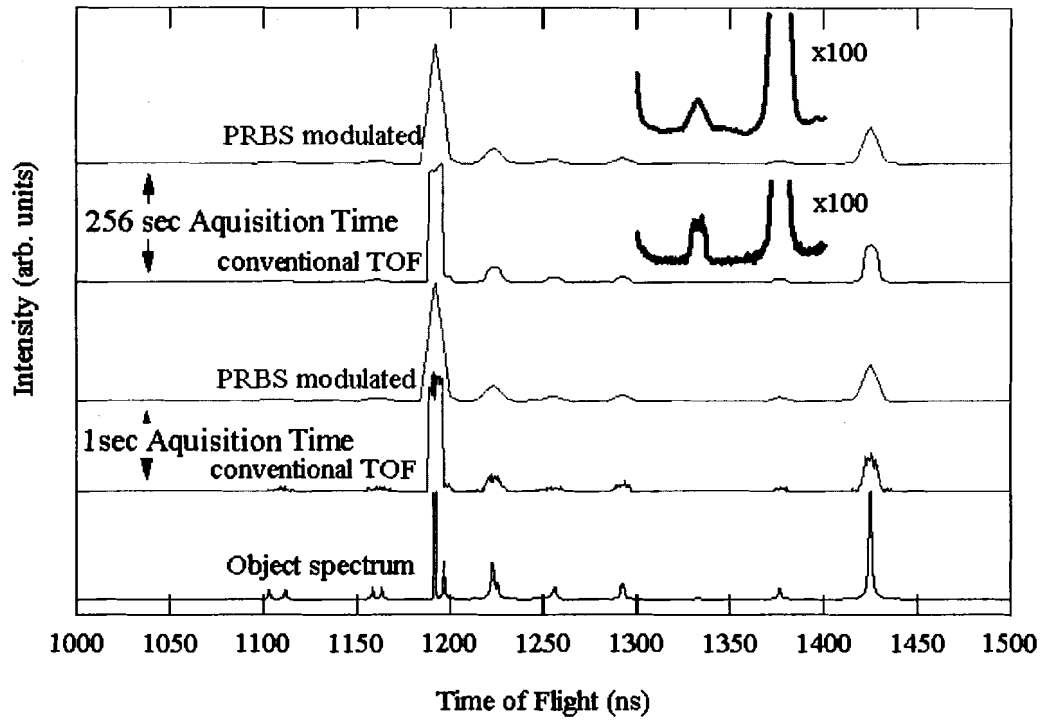


Figure 3.3 Comparison of the object spectrum with simulated single pulse TOF spectra (gate open 8 ns) and the spectra recovered from a PRBS modulated experiment using the cross correlation method. Acquisition times of 1 and 256 sec are shown for an incident beam current of 10^6 counts/sec. Here, the response function is the ideal (step function) PRBS sequence as in Fig. 3.1a.

Figure 3.4 compares the results of maximum likelihood recovery with the cross-correlation method. In this example, the modulation function, p , contained linear rise times of 1 ns (c.f. Fig. 3.1c) but maintained a 50% duty cycle. Results given in Figure 3.4 are for 256 MCts in the modulated data. The resolution of the cross-correlated spectrum is degraded, as expected, by convolution with an approximately triangular autocorrelation function (c.f. Fig. 3.1d). In the maximum likelihood recovery method, the results improve with both the total number of counts in the data and the number of iterations. As iterations proceed, the Lucy algorithm refines the spectral estimate, significantly improving spectral resolution, while artifacts remain at a level of less than 0.01%. Note that the gain peaks at 1160 ns, corresponding to 18 meV separation, are clearly resolved.

Finally, we describe the results of maximum likelihood recovery when the modulation function, p , includes both energy corruption effects and the time lags predicted by the model potential for an interleaved comb with applied voltage, $V_{\text{app}} = \pm 0.4$ V, wire spacing, $d = 1.2$ mm, radius, $R = 25$ μm and an acceptance angle of $\pm 1^\circ$ [75]. The modulation function p , used for deconvolution, was generated in the same way as the data, except that it included only the elastic peak energy distribution. Thus, p characterizes both the monochromator energy distribution and the non-idealities of the chopper, and would be measured in practice simply by directing the monochromatic beam directly into the TOF detector. Figure 3.5A compares the true object spectrum with results of the Lucy algorithm as a function of the number of iterations. This data was generated with a detector time bin of 0.5 ns, and the reproduction of the object function is excellent. Note that the feature in the base of the elastic peak is well resolved and the resolution of the doublets are comparable to that in the true object spectrum (the doublet

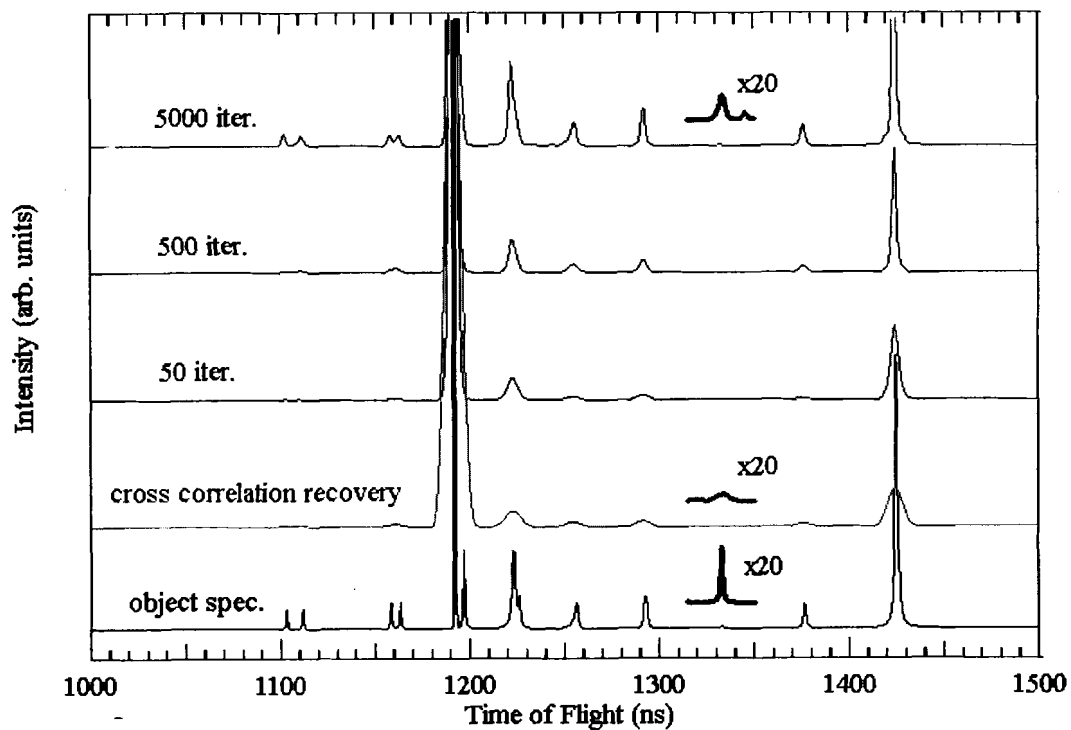


Figure 3.4 Comparison of the object function with estimates recovered from PRBS modulated data using the cross correlation method and the maximum likelihood method (for 50, 500 and 5000 iterations). The modulation function contains linear rise times as in Fig. 3.1c. Data shown for 256 MCts total in the modulated data.

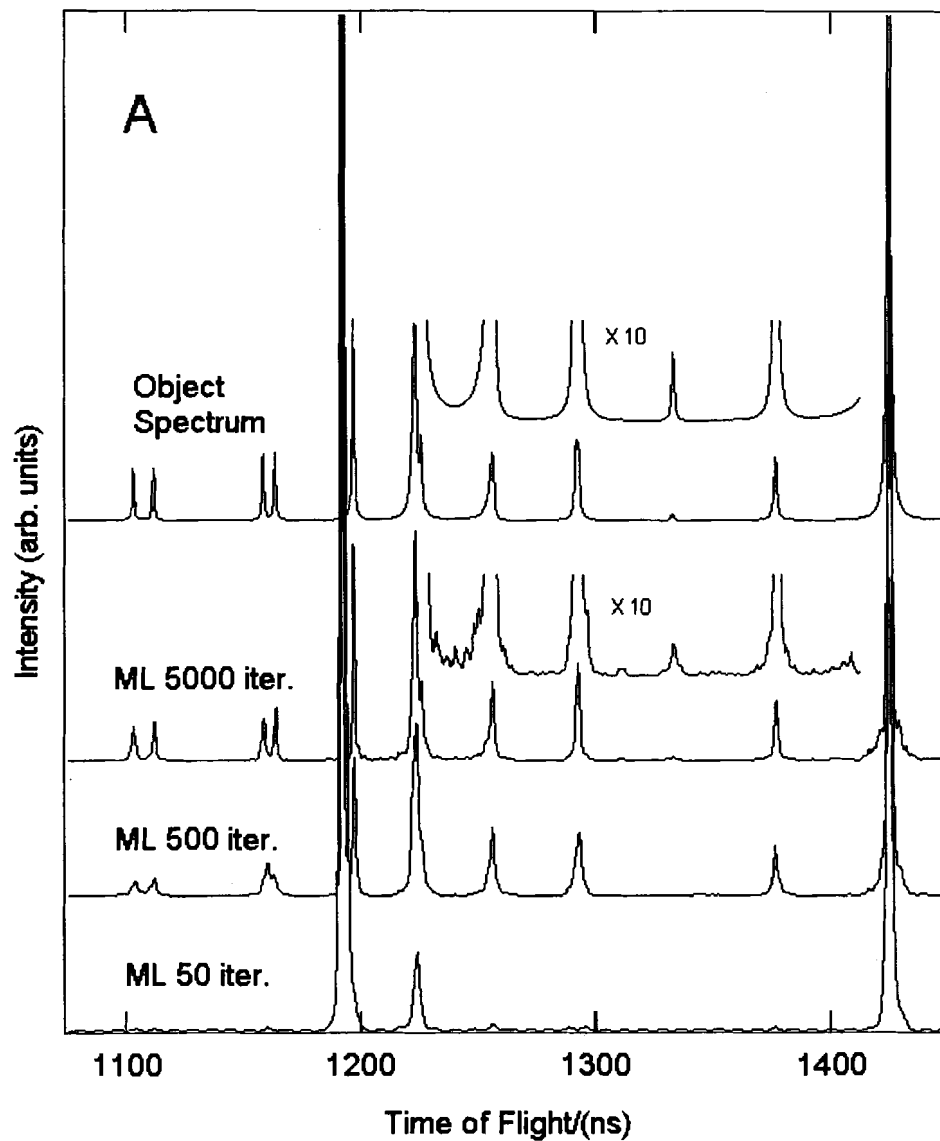


Figure 3.5 A) Comparison of the object function with estimates recovered from PRBS modulated data that includes the non-ideal chopper response using the maximum likelihood method (for 50, 500 and 5000 iterations). The modulation function contains both energy corruption and the time lag in opening and closing based upon our model of the interleaved comb chopper [75] and the energy distribution of the monochromatic beam. Data shown for 256 MCts total in the modulated data.

at 1230 ns corresponds to 9 meV separation). Even the feature at 1340 ns with intensity 0.1% of the elastic peak is recovered with an intensity roughly an order of magnitude greater than the noise. Thus, the Lucy algorithm is able to account for both the rather substantial energy corruption effects of the chopper and the Poisson noise distribution. By contrast, Figure 3.5B shows the cross correlation results using the ideal PRBS response function to process the same energy-corrupted, PRBS modulated data. The negative artifacts appearing between channels 1700 and 1900 ns are consistent with the non-ideal behavior of the chopper, leading to an autocorrelation function similar to that shown in figure 3.1f. To illustrate the importance of accurately defining the modulation function, we also show the results of the maximum likelihood deconvolution using the ideal PRBS (c.f. Fig. 3.1a) sequence. Artifacts appear at the positions of the negative artifacts in the cross correlation recovery and the true features are split.

3.5 Conclusions

We have simulated the effects of the Poisson noise distribution and non-ideal behavior of the "interleaved comb" chopper on PRBS modulated TOF-HREELS data. We have shown for the first time that maximum likelihood methods can be combined with PRBS modulation to achieve resolution enhancement, while properly accounting for the Poisson noise distribution and artifacts introduced by the chopper [76]. The results suggest that resolution similar to that of modern high resolution electron spectrometers can be achieved with a dramatic performance (throughput) advantage over conventional, serial detection analyzers.

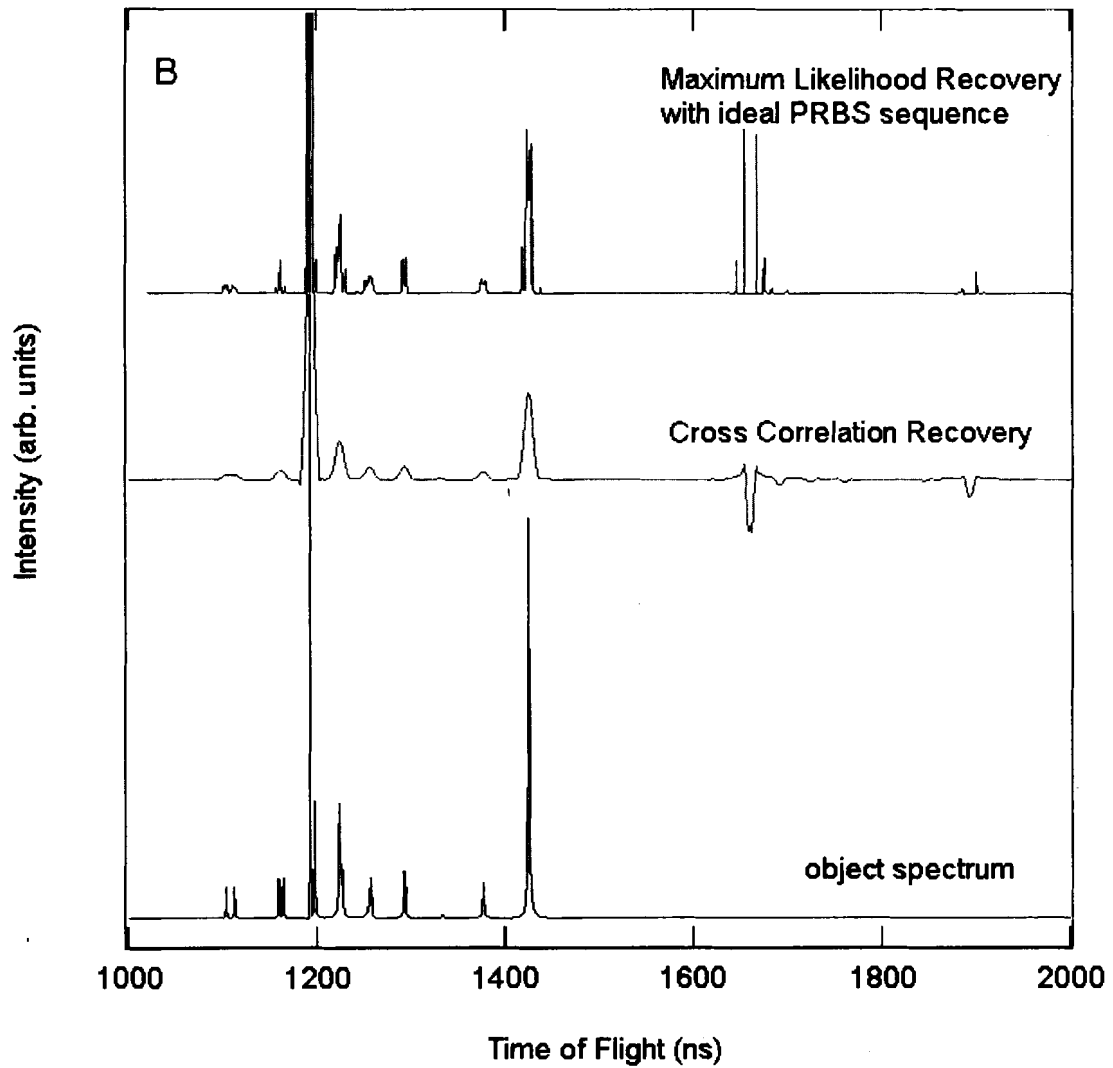


Figure 3.5 (continued) B) Illustration of the negative-going artifacts in the cross correlation recovery due to the non-ideal response of the chopper (middle curve) and the importance of accurately determining the response function: results (upper curve) of using the ideal (step function) PRBS (Fig. 1a) sequence in the maximum likelihood method.

Chapter 4

DESIGN OF A TOF-HREELS SPECTROMETER

4.1 Introduction

In this chapter we describe the first generation instrument designed for time of flight electron energy loss spectroscopy, based upon the results of the work in Chapters II and III. The theoretical model of the interleaved comb chopper and the trajectory simulations presented in Chapter II indicate that sub-nanosecond rise times can be achieved. Comparison of the static and dynamic properties with experiment suggests that the model provides a good description of the optical properties of the chopper. However, the energy corruption effects are particularly severe with this chopper design. Nevertheless, incorporation of the energy corruption histograms into a stochastic model, as presented in Chapter III, indicates that at a beam energy of 2 eV and a flight length of 1m, the maximum likelihood recovery algorithms are able to compensate for the non-ideal characteristics of the chopper and improve the time resolution by at least a factor of 8 over the nominal 8ns time step chosen for the PRBS generator clock.

The major components of the instrument are a conventional HREELS spectrometer (LK Technologies, Model EELS3000), comprised of a double-pass monochromator and double-pass analyzer, and the TOF analyzer, comprised of a set of collimation slits, the chopper assembly, an output Einzel lens, a magnetically and electrically shielded flight tube, and a custom-modified micro-channel plate detector, shown schematically in Fig. 4.1. In the following sections, we will describe the conventional HREELS spectrometer and vacuum system, the TOF analyzer and the associated electronics.

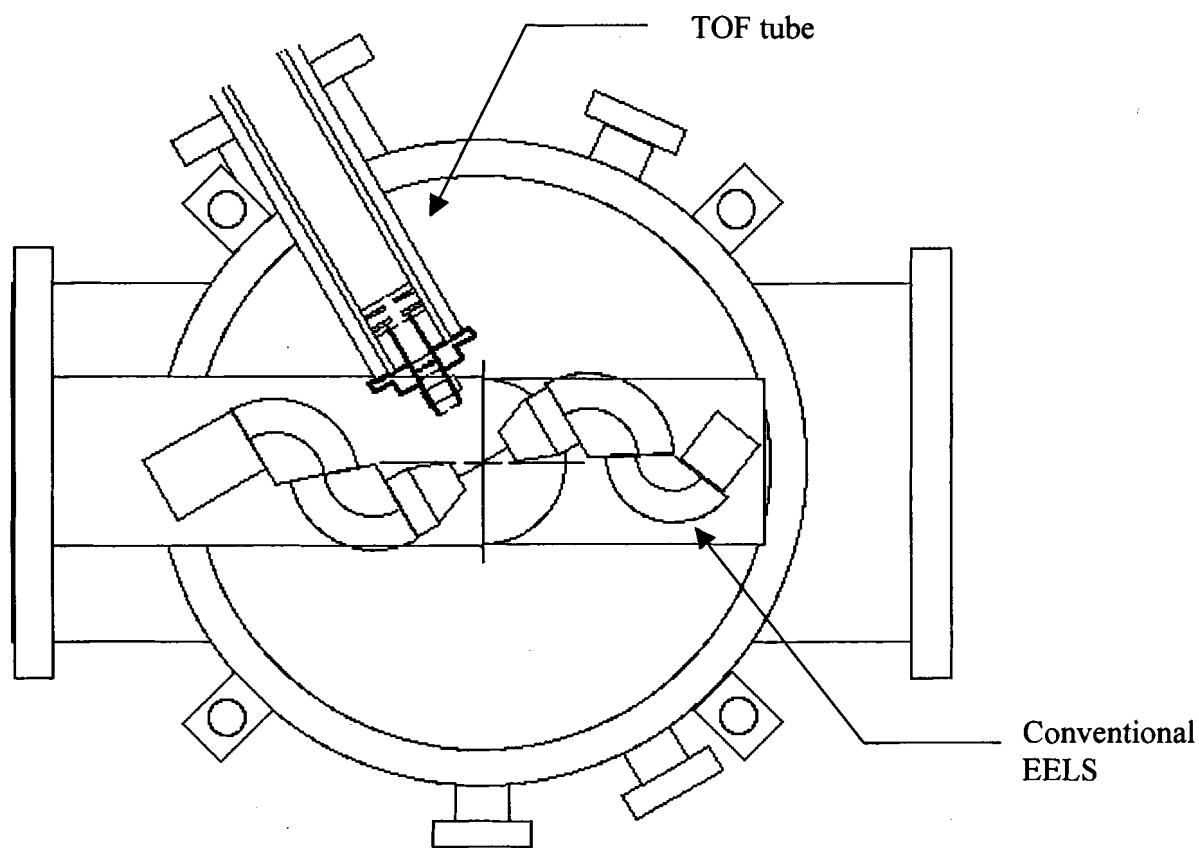


Figure 4.1 Schematic drawing of the TOF-HREELS system, comprised of a rotatable double pass monochromator, a double pass analyzer, and a TOF analyzer. The TOF analyzer includes entrance apertures to limit the angular distribution at the chopper to $\pm 1^\circ$

In the HREELS system, a LB_6 filament is used to generate high density electron beam. Monochromation of electrons emitted by thermionic emission is achieved by passing through two cylindrical-sector electron energy analyzer (called monochromators) - typical radius 35 mm, typical pass energy 0.38 eV. Electrons are retarded before entry into sector, and then accelerated to sample. Same two cylindrical-sector electron energy analyzer (called analyzers) are used to analyze electron kinetic energy. The monochromators can be rotated by an angle of 110° so as to direct the electron beam into either the conventional analyzer or the TOF detector. The schematic of the experiment is shown as in Fig 4.1. Samples to be studied are positioned at the center of the rotation. After the electron resolution are optimized by tuning straight through the conventional analyzer, the electron beam are directed to impact the sample and the scatted electrons are collected either by a conventional HREELS detector or by the TOF detector located at the end of a 1.2 m flight tube. An interleaved chopper assembly is put in front of the flight tube. When a PRBS modulation signal is applied to the chopper, the TOF detector will collect the electron spectrum modulated by the chopper. With the help the deconvolution software, the object spectrum can be post-processed. The entire instrument is magnetically shield.

4.2 Description of the Conventional HREELS Instrument

The HREELS spectrometer (ELS3000, LK Technologies, Bloomington, IN) makes use of a highly optimized double-pass monochromator design described by Ibach[12]. The “penultimate” model ELS3000 instrument was chosen, rather than the “ultimate” spectrometer, because in the ELS3000 the monochromator is rotatable which

was more conducive to retrofitting the TOF detector. Several design changes were specified for the spectrometer and the vacuum chamber. We first describe the features of the standard instrument, and then give the modifications chosen for the TOF spectrometer development project.

The monochromatic source consists of an electron gun with a LaB₆ cathode and mounted in a repeller electrode geometry designed to accelerate and focus the thermionically emitted electrons into the pre-monochromator[12]. The pre-monochromator operates as a "retarding" monochromator, such that the electrons are decelerated by a factor of 1-2 at the entrance of the pre-monochromator. At the exit of this stage, as they approach the entrance slit of the second monochromator, the energy of the electrons is again reduced to about 1/5 of the nominal pass energy of the pre-monochromator. To compensate for space charge effects, Ibach modified both the overall deflection angle from the ideal 127° cylindrical deflector and the position of the exit slit in the pre-monochromator. The pre-monochromator has a total deflection angle of 119° with the exit slit offset by 1.1 mm. In addition, the design utilizes compression plates above and below the cylindrical sectors, adjusted to a negative potential relative to the beam energy, to reduce the vertical spread of the beam and generate a parallel beam in the non-dispersive direction at the exit slit. The second monochromator acts as a non-retarding monochromator. The deflection angle is increased to 140°, again to compensate the space charge effects. The monochromator also has compression plates; however, the magnitude of their potentials, relative to the potential of the beam, is much smaller than in the pre-monochromator. The analyzer is also a double-pass geometry with the design of each sector identical to the main monochromator. A symmetrical system of input-

output "zoom" lenses, positioned between the monochromator and analyzer, is used to focus and accelerate and decelerate the electron beam to and from the sample surface, respectively[12]. These lenses are non-circularly symmetric with different focal lengths in the dispersive and non-dispersive plane.

The whole ELS3000 unit is mounted on a 12 inch (305 mm) O. D. vacuum flange. Construction materials are all non-magnetic to ensure the lowest possible stray magnetic fields. Dual magnetic shields are provided at the flange to interface with the chamber magnetic shields. The monochromator rotates by means of a precision, linear-feedthrough/rack-and-pinion gear system. The range of motion was increased from the standard instrument to a full scale range of 110° , such that the monochromator could rotate beyond the "straight through" position by 10° , through the position of the TOF detector, 90° away from the straight through, to a position 10° beyond the position of the TOF detector. A direct readout of the monochromator angle is provided by a scale, which is viewed through a port on the mounting flange. A custom motorized linear motion feedthrough was specified for future work to allow automated control of the monochromator position.

The scattering chamber was also modified with a slot to allow the lens of the TOF detector access to the sample. The scattering chamber is biased at ground potential, rather than at the nominal beam energy implemented by Ibach[12].

Since the purpose of the project was to develop a new TOF detector, we anticipated opening the vacuum chamber frequently and needing access to the spectrometer and components of the TOF detector. Therefore, we specified the vacuum

chamber in an inverted orientation, so that the manipulator, top flange, and covers of the μ -metal shielding could be removed, gaining access directly to the instrument.

4.3 The TOF Analyzer

4.3.1 Chopper Assembly

The specification of a lens for a “wide band” analyzer presents a technical challenge, since the relative range of electron energies can vary by 100%. For example, if the primary energy is 1eV, then we expect the vibrational loss spectrum to extend roughly 0.5 eV to lower energy. Furthermore, to achieve sufficiently high time resolution, the free flight energy cannot exceed a few eV. Therefore, the possibility of accelerating the electrons in order to reduce the variation in the loss energy spectrum, relative to the elastic peak, limited the relative energy range to about 25%. If we further add constraints to have a well-defined angle of acceptance from the sample across the energy range and a $\pm 1^\circ$ input acceptance angle to the chopper, then the input lens design becomes much more difficult.

In order to avoid the complications of designing a wide band lens during the initial development of the instrument, the angles of acceptance were set by a set of three copper beryllium slits. Each of the three slits has a lateral width (i.e. in direction of the chopper deflection) of 0.5 mm and a height of 1.9 mm. Two of the three slits provide collimation to a maximum lateral angle of 1° from an edge of the first slit to the opposite edge of the second slit. This collimation ensures that the chopper will not deflect any part of the electron beam into the detector when the chopper is closed, i.e. when the deflection voltages are present. The first slit is 43mm from the axis of rotation of the

monochromator (the nominal sample position); the second is 28.6mm further; the chopper plane is 6.35mm beyond the second slit; and the last slit is 35.2mm from the chopper plane. The included angle of the last slit from the sample is 0.26° in the deflection direction, while the included angle of the last slit from the center of the chopper is 0.83° . Both of these included angles are within the included angle of the 18mm diameter detector from their respective origins.

The chopper was constructed in the manner described in Chapter II, using lift-off methods to pattern the gold bus bars and attachment pads on the square ceramic substrate. The chopper wires were 25 μm diameter, wire bonded to pads placed on 250 μm centers. The driver signals were coupled from impedance matched SMA feedthroughs to the chopper via shielded 50 Ω cable.

4.3.2 Magnetic Shielding

The magnetic shielding was designed to provide attenuation of the local magnetic field (0.6 gauss oriented roughly vertically) so that a 1eV electron will fly longitudinally down the 1 m long horizontal tube with less than 1mm of lateral deflection. This specification implies that the strength of a uniform vertical field be less than 0.07 milligauss, which requires an attenuation of at least 8500.

The magnetic shielding for the flight tube consists of two coaxial μ -metal tubes, each separately reduced down to overlap with a corresponding μ -metal collar. Each collar is fit into the TOF port of the corresponding layer of the double μ -metal shields in the main HREELS chamber. This layer-by-layer coupling of the flight tube shields to the main chamber shields ensures a continuous magnetic field attenuation of $>20\,000$. The

overlapping collar joints provide a magnetic path with approximately half of the reluctance of either its associated tube or chamber shield, thus providing good flux containment where the tube enters the chamber. The flight tube μ -metal shields were constructed by Amuneal Manufacturing Corporation with their 0.062 inch thick AMUMETAL. The inner shield has an I.D. of 4.18 inch and the outer shield has an I.D. of 5.00 inch and each extends from the main chamber shield 55 inches. Each tube is constructed in two sections to allow hydrogen annealing after construction. The sections were joined with an overlapping collar and secured by machine screws. In hindsight, we found that it would have been preferable to have an 8 inch Conflat port for the flight tube in order to avoid the reduction of the μ -metal shield at the entrance to the chamber.

4.3.3 Faraday Shielding

The low, 0.5 eV kinetic energy specification for the optics of the flight tube further requires a highly uniform work function along the flight tube and adequate shielding from both static electric and AC electromagnetic fields. The inner flight tube was constructed from a 60 inch long, 2.865 inch I.D., 0.0940 inch thick, OFHC copper tube that was bright dipped and coated with colloidal graphite. The colloidal graphite was applied in a custom-built apparatus to rotate the horizontal tube on its axis while the alcohol evaporated from the graphite suspension.

4.3.4 The Detector

A chevron design, micro-channel plate detector (MCP) with a cone-shaped high-speed anode (AP-TOF, Gallileo Corp., Sturbridge, MA) was modified to be biased for negative particle detection. The output was coupled to a 50 Ω Kapton transmission line with a 47pf capacitor. The anode bias forms the shunt part of a pole-zero canceled output

circuit to reduce ringing in the output pulse signal. This provided pulses with a nominal 800 ps FWHM. The detector assembly is mounted on an electrically isolated frame that is connected to the copper flight tube with a spring contact made from a loop of copper beryllium sheet. The front and back bias points of the MCP were bypassed to the detector frame with 47 pf capacitors. Careful consideration was given to the copper enclosure around the anode connections to ensure that any current flowing on the outside of the shield of the detector signal coaxial cable does not flow into the enclosure.

4.4 The Electronics

A functional block diagram of the electronics is shown in Figure 4.2. The chopper driver circuitry consisted of a 125 MHz clock, generated by the Time-to-digital converter (TDC), which provided the time base for the PRBS sequence generator. At the core of the PRBS generator was designed to have daughter cards to select the feedback circuit for different shift register lengths. Only the 8-bit shift register length, generating a sequence of period $2^8 - 1 = 255$ clock cycles, was implemented. The output of the shift register was inverted and then coupled, via a balun, to generate two synchronous output signals of equal and opposite magnitude. Each output signal provided the input to a pulse generator (E&H 1560, E&H International Inc) modified to utilize only the output stage of the pulse source. The $50\ \Omega$ output signals could be tuned to balance the amplitude of the drive potentials.

The detector pulse output signal was capacitively coupled to a 1 GHz bandwidth preamp (Ortec 9306, Oak Ridge, Tennessee) with a gain reduced to approximately 8. The output signal was then passed to a discriminator/amplifier (Ortec 9307, Oak Ridge,

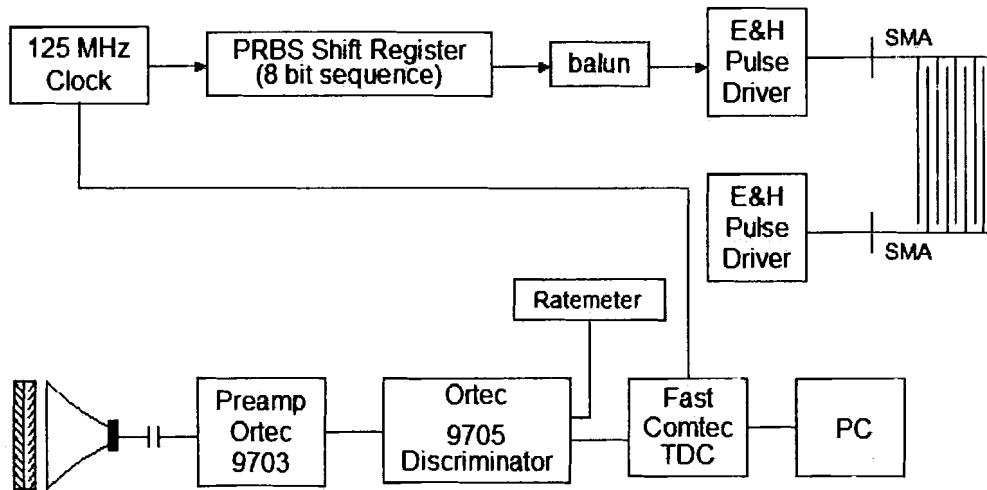


Figure 4.2 The functional block diagram of the chopper driver circuitry and pulse counting electronics.

Tennessee) that generated NIM pulses which supplied the event signal input to the TDC (FastComtec, Oberhaching, Germany) installed in a personal computer (Tratos system). The TDC was configured to start timing on the rollover pulse of the PRBS generator (all 1's in the shift register) and stop upon receipt of an event pulse. The TDC time resolution was 250 ps, corresponding to an oversampling factor of 32, relative to the 8 ns time base of the 125 MHz clock. Software provided with the TDC was used to accumulate the TOF data into a histogram. In this configuration, the dead time required to reset the TDC after each stop event resulted in loss of 50% of the TOF events. This mode was convenient for examination of the TOF spectrum during data acquisition; however, the board could be configured to take data continuously for approximately 60 seconds without losing events. The maximum burst rate of the device was 2 GHz.

The monochromator was tuned up using the conventional HREELS analyzer and standard electronics supplied with the ELS3000 instrument. The lens voltages applied to the output Einzel lens were generated from the McAlister HREELS electronics of the system described in the measurements of Chapter II.

Chapter 5

FACTORS AFFECTING INVERSION OF PRBS MODULATED TOF DATA WITH THE LUCY ALGORITHM

5.1 Introduction

Pseudo-random binary sequence (PRBS) modulation is a well known method to gain a throughput advantage in time-of-flight (TOF) instruments[42, 55-57, 77, 78], and is closely related to Hadamard spectroscopy[58]. The method utilizes special sequences, p , that admit particles to the flight path 50% of the time to gain a throughput advantage over single pulse TOF that can be as large as 500 or 1000, depending on the nature of the underlying time-of-flight spectrum, which we will refer to as the object function, o .

In the ideal case, the time-modulated data, $y = o \otimes p$, is a convolution of the object function with the modulation function, p . These special sequences, known as Hadamard PRBS, or maximal length shift register sequences[58, 59], have the unique property that their autocorrelation is approximately a delta function. In principle, the object function can be recovered simply by cross-correlation; *i.e.* $p \oplus y = (p \oplus p) \otimes o \approx o$.

In reality, the response of choppers, or modulators, is limited by finite thickness effects[64, 81] and interactions between the chopper and the particles[81], which lead to artifacts in the cross-correlation method[41, 64]. Recently, we have demonstrated the use of probability-based spectral estimation methods[76, 82] to recover the object function by iteratively deconvoluting the raw time-modulated data, y . Using the Lucy algorithm, we find significant improvement in reducing the effects of noise and chopper-particle interactions. Additionally increased time resolution over the cross-correlate method can be obtained.

We present a theoretical analysis of the interactions of a particular modulator (the “Bradbury-Nielsen gate”[83] or the “interleaved comb” chopper[40]) with an electron beam and their effect on the ability of the Lucy algorithm to invert the raw time-modulated data, for applications in High Resolution Electron Energy Loss Spectroscopy (HREELS). We compare the results with experimental TOF-HREELS data for a polytetrafluoroethylene (PTFE) spectrum[33, 34]. The results are particularly relevant to applications in ion TOF mass spectroscopy and, in a more general way, to PRBS modulation in neutron scattering or molecular beam studies.

The Chapter is organized as follows. We begin with a theoretical model of the chopper interaction and distinguish features of the response that causes the unusual data to deviate from what would be obtained by convolution. Next, we present the experimental and theoretical methods. The results are given in section IV and the implications for data recovery and instrument design follow.

5.2 Theoretical Background

In Chapter II[81], we have given an analytical expression for the potential of a Bradbury-Nielsen gate in which an infinitely repeating set of wires, with bias, V_{app} , alternatively positive and negative, are of finite diameter and infinite length. For the limiting case in which the wire radius, R , is small compared to the wire spacing, d , the potential, $\psi(x,y)$ is obtained from a conformal map as

$$\psi(x, y) = \frac{\lambda}{2\pi\epsilon_0} \ln \left[\frac{\cosh(\pi x/d) + \sin(\pi y/d)}{\cosh(\pi x/d) - \sin(\pi y/d)} \right] \quad (5.1)$$

where the line charge is defined as, $\lambda = \frac{2\pi\epsilon_0 V_{app}}{\ln \left[\frac{1+\cos(\pi R/d)}{1-\cos(\pi R/d)} \right]}$. The potential is shown in Fig. 5.1A as a contour plot, where $2R/d = 0.1$. When equal and opposite potentials are applied to the

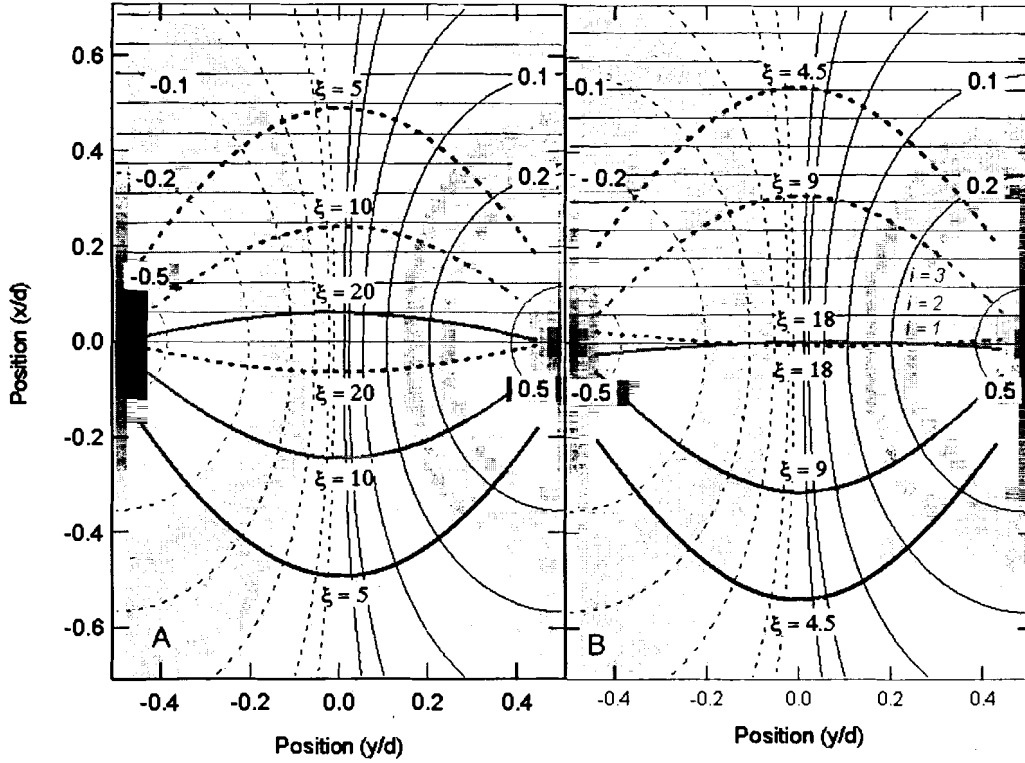


Figure 5.1. Contour plots of the potential for a wire diameter-to-spacing ratio of 0.1.

Contour lines are plotted relative to the applied voltage, $\pm V_{app}$, and dimensions are scaled relative to the wire spacing, d . The critical boundaries, beyond which an electron must be when the potential is turned on (dashed curves) and before which an electron must be when the potential is turned off (bold solid curves) to reach the detector are shown for the ratios $\xi = \frac{KE}{V_{app}} \cdot \theta_{acc}$ as indicated. To illustrate the effect of the energy variation across the vibrational loss spectrum, we compare the critical boundaries for the experimental case of $V_{app} = \pm 0.4V$ for $\theta_{acc} = 0.5^\circ, 1^\circ, 2^\circ$ at A) the primary beam energy of 4 eV, and B) for an inelastically-scattered electron beam of energy 3.6 eV. The rectangular regions for time steps of 12.5 ps and $d = 250 \mu m$ are also shown for A) a kinetic energy of 4 eV and B) 3.6 eV.

grid wires, charged particles traveling in the $+x$ direction are deflected in $\pm y$ directions. For small deflection voltages, the angle is proportional to the ratio[81] of eV_{app}/KE and an appropriate aperture can be selected to exclude the deflected particles. The advantage of this gate over a set of deflection plates is the more rapid spatial decay of the applied potential, $V(x) \propto 4\lambda \exp(-\pi|x|/d)$, so that the particles do not interact strongly with the gate until they are within approximately one d -spacing of the plane of the chopper.

In the simplest approximation, the time-dependent chopper voltage modulates the transmission of the gate such that the time-modulated data, y , is a convolution of the PRBS sequence, p , with the intrinsic time-of-flight distribution, $o(t)$, as long as the applied voltage is sufficiently large to exclude all particles in the energy distribution, $o(E)$. We will denote a time of flight distribution as $n(t)$ and the corresponding energy distribution as $n(E)$. Given the flight path length L and particle mass, m , they are related by

$$n(E)|dE| = n(t)|dt| \quad (5.2)$$

A more detailed examination of the mechanics[81] reveals that the finite extent of the fields leads to deviations from the convolution in two distinct ways. First, if an electron is near the gate and the potential is applied instantaneously, the electron either gains or loses potential energy depending upon whether it is closer to a negative or positive wire, respectively. This means that the energy spread of a monochromatic beam, $o(E) = \delta(E - E_0)$, is increased after it passes through the chopper. Because the energy change, or “energy corruption,” depends upon the particle’s distance from the chopper at the time the potential is switched, the spread in the energy domain varies with time. Since the energy determines the flight time, the particle’s flight time distribution broadening

depends on both its distance from the chopper at the time the potential switches and its original energy. Alternatively, the point spread function in the time domain varies with the relative time between a particle's arrival at the plane of the chopper and the time the potential switches, as well as with its original energy. Clearly, the spread in flight times varies with time and is energy- dependent; therefore, the modulation function can not be strictly described as a convolution in the time domain.

When the time to cross the field-affected region is small compared to the time base of the modulation sequence (which becomes true for choppers of sufficiently small wire spacing, d), we can define a critical boundary[81] between the positions of particles at the time the potential is switched, that will reach the detector from those that will not. These boundaries are shown as the bold solid curve (potentials turning off) and the dashed curve (potentials turning on) in Fig. 5.1. For the case in which the potentials are turned off, the particle will reach the detector if it is before the solid curve at the time the potential is switched; whereas, when the potential is turned on, the particle get through if it is beyond the dashed curve. This leads to behavior (for $\xi < 20$) in which the gate opens late and turns off early, and vice versa for ($\xi > 20$) which we refer to as a “lead / lag” effect.

The energy corruption effect may be approximated as a convolution in the energy domain for a small interval of arrival times, δt . Consider the situation for a single energy particle beam, *i.e.* $\phi(E) = \delta(E - E_0)$, where E_0 is the monochromatic energy of the particles. We subdivide the modulation sequence time step, τ , into m subintervals, $i = 0, 1, \dots, m$, of width ($\delta t = \tau / m$), as shown in Fig. 5.2A. We then divide the potential along the x -direction into equal intervals of width, $v \cdot \delta t$, where v is the particle's velocity, as

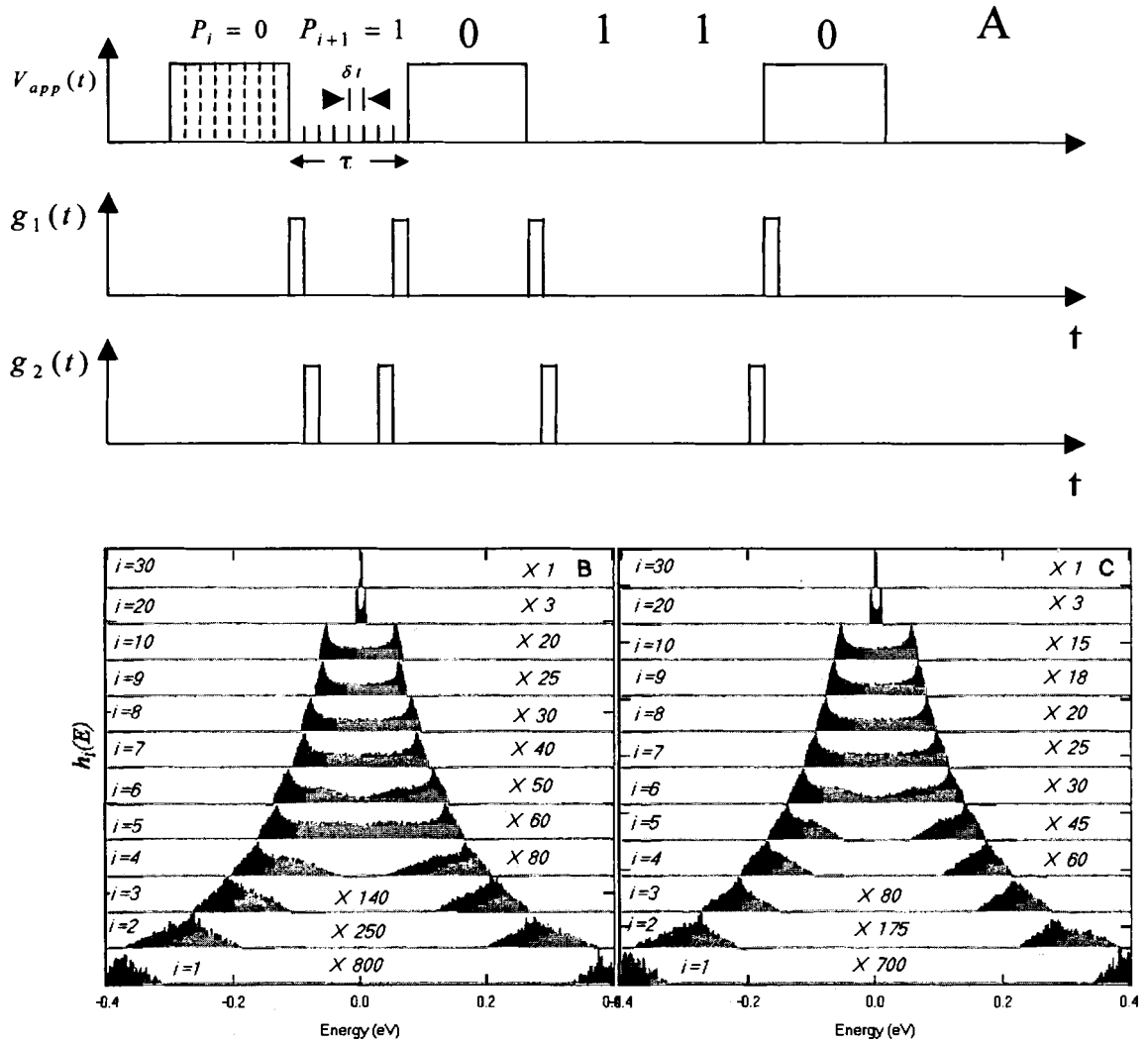


Figure 5.2. A) Schematic illustration of the relationship between the time dependence of the potential applied to the chopper, $V_{app}(t)$, and the functions $g_i(t)$, that represent the periods during which energy corruption histogram, $h_i(t)$, broadens the object function (See text for details). Energy corruption histograms, $h_i(E)$, are shown for time steps of 12.5 ps, $\theta_{acc} = 1^\circ$, $V_{app} = 0.4$ V, and a wire spacing of $d = 250$ μm for a kinetic energy of B) 4 eV and C) 3.6 eV. The vertical scales have been multiplied by the factors indicated.

indicated by the rectangles in the upper half of Fig. 5.1A for $i = 1, 2, 3, \dots$. If the particle is within region i at the time the potential is turned on, then statistically it gains or loses an energy chosen randomly from the distribution of potentials within the region of area $\mathfrak{A} = v \cdot \delta t \cdot d$, given generally by

$$h_i(E) = \frac{1}{\mathfrak{A}} \int_{S_n(E)} \frac{1}{\nabla \psi(x, y)} dx dy \quad (5.3)$$

where $S_n(E)$ is a region between contours of constant energy E and $E + dE$. The energy corruption histogram was computed by Monte-Carlo integration over the portion of region i after the critical boundary, $x = c(y)$, where

$$h_i(E) = \frac{1}{\mathfrak{A} \cdot n} \sum_{j=1}^n \begin{cases} 1, & E \leq \psi(x_j, y_j) \leq E + \delta E, \quad x_j > c(y_j) \\ 0, & \text{otherwise} \end{cases} \quad (5.4)$$

and n points (x_j, y_j) are chosen randomly within region i [81]. The lead/lag effect was incorporated by including in \mathfrak{A} , only those portions of the region $x_j > c(y_j)$ for which particles will reach the detector, which reduces the area of the histogram. The integral area of $h_i(E)$ therefore includes the transmission of the grid for time interval i . We illustrate these histograms in Fig. 5.2B and 5.2C. (Note that the condition becomes $x_j < c(y_j)$ when the potential is turned off)

In any time step of the modulation sequence in which the particle arrives at the plane of the chopper $i \cdot \delta t$ after the potential is switched off (or $i \cdot \delta t$ before the potential is switched on, due to the symmetry of the potential), the beam of energy, $o(E) = \delta(E - E_0)$, will have a final energy distribution $o(E) \otimes h_i(E)$. While the energy corruption causes the same spread for particles of any energy, the definition of the *spatial region* to which the histogram $h_i(E)$ applies depends upon the particle's velocity.

Therefore, only for $o(E)$ within a limited energy range is it possible to approximate the new energy distribution as $o(E) \otimes h_i(E)$ for an arbitrary distribution $o(E)$. In Fig. 5.1A, we show the size of the intervals $v \cdot \delta t$ for 4eV and 3.6 eV electrons, energies typical of vibrational loss spectrum for a primary beam energy of 4eV. If the chopper response varies significantly over the energy range of $o(E)$, we must divide $o(E)$ into separate intervals $o_j(E)$ and sum the resulting convolutions, $o_j(E) \otimes h_{i,j}(E)$, for a particular arrival time, $i \cdot \delta t$. After calculation of the energy- broadened object function for each time interval, we need to transform the energy distribution ($o(E) \otimes h_i(E)$) to the time domain. Since the energy corruption histograms vary with the energy of the particles, the modulation is not strictly a convolution in energy either.

Finally, to construct the entire PRBS time-modulated data, we note that the energy corruption histogram $h_i(t)$ applies to all time intervals that occur $i \cdot \delta t$ after (or before) the potential is switched off (on) in the entire, oversampled PRBS sequence. We therefore construct a time modulation function $g_i(t)$ which contains a square pulse of unit area and width δt at all positions $i \cdot \delta t$ after a falling edge in the potential and $i \cdot \delta t$ before a rising edge, as illustrated in Fig. 5.2A. The modulated data, $y(t)$, is therefore expressed as a sum of convolutions:

$$y(t) = \sum_{i=1}^N z_i(t) \otimes g_i(t) \quad (5.5)$$

where $z_i(t)$ is obtained for a monochromatic beam from transformation of $o(E) \otimes h_i(E)$ to a TOF distribution. When $o(E) = \delta(E - E_0)$, $y(t)$ is the chopper response

function, $p(t)$, this is the signal that is measured with a monochromatic beam of energy E_0 .

In summary, the chopper response function $p(t)$, deviates from a convolution in time because different energy corruption histograms must be applied for different arrival times at the chopper, due to the spatial extent of the field. To calculate the time-modulated data, $y(t)$, for an arbitrary object function, $o(E)$, equation 5.5 is valid only if the variation of the energy corruption histograms with the particle's energy is small; otherwise the object function must be divided into a set of energy intervals. Again, the formalism holds only when the time for the particle to cross the field-affected region is small compared to the PRBS base time step, τ .

5.3 Methods

5.3.1. Experimental

A schematic diagram of the system is shown in Fig. 5.3. The system is comprised of a double pass HREELS spectrometer (LK Technologies, Model EELS3000) and a custom-designed TOF analyzer. The TOF analyzer optics consist of a set of collimation slits ($\theta_{acc} = 1^\circ$), a chopper assembly, and an Einzel lens to deflect and focus the beam onto the microchannel plate detector. Detailed information about the design of the TOF-HREELS system is given in a separate paper [84]. The monochromator rotation was extended to a range of 110° to allow the beam to be directed into either the conventional analyzer or the TOF analyzer. The spectrum of a thin, azimuthally-aligned film of PTFE (Teflon®, Goodfellow), described elsewhere[33, 34], was measured with both analyzers. In the experiments, the chopper consisted of 80 gold wires, of 25 μm diameter and 250

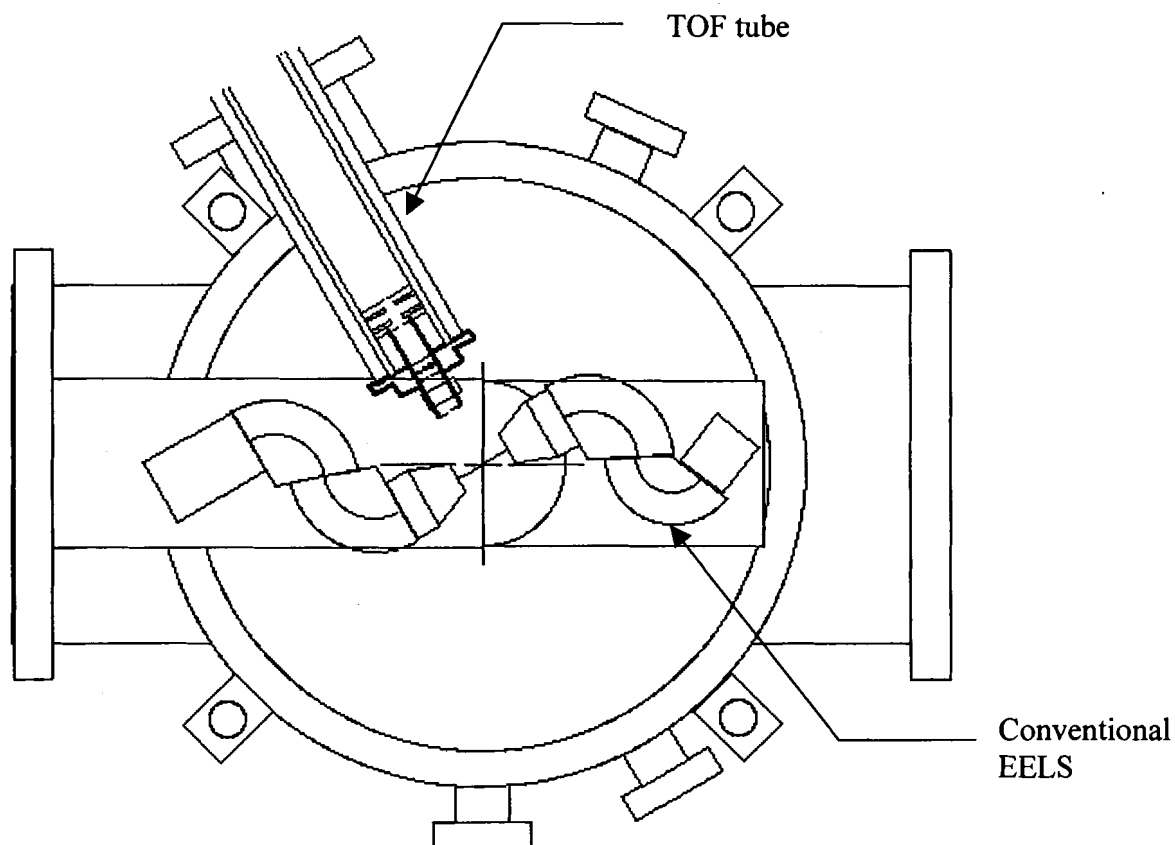


Figure 5.3. Schematic drawing of the TOF-HREELS system, comprised of a rotatable double pass monochromator, a double pass analyzer, and a TOF analyzer. The TOF analyzer includes entrance apertures to limit the angular distribution at the chopper to $\pm 1^\circ$ in the horizontal plane, a Bradbury-Nielsen gate chopper, an output Einzel-type lens with deflection capabilities, and a microchannel plate detector.

μm spacing, fabricated on patterned alumina substrates as described in Chapter II[81]. The exit slit was selected to exclude electrons deflected by more than $\pm 1^\circ$. The PRBS signal was generated by an 8-bit shift register and output drive electronics which allowed the magnitude of the $\pm V_{\text{app}}$ potentials to be varied as required. The TOF detector was based upon a micro-channel plate detector (AP-TOF, Gallileo Corp., Sturbridge, MA), which was custom-modified for negative particle detection. The pulse signal coming from the detector was amplified (Ortec 9306) and discriminated (Ortec 9307) and then directed to a TDC card (FAST Comtec, Oberhaching, Germany) in a PC. The response function, $p(t)$, was measured with the monochromator directed straight into the TOF analyzer. After acquiring TOF data from the PTFE sample, a custom- designed implementation of the Lucy algorithm[82] was used to recover the time of flight spectrum.

5.3.2. Trajectory Simulation Methods

In order to simulate the noisy data obtained in the experiment and to test the recovery algorithm, we developed a stochastic simulation based upon trajectory calculations over the potential of an infinite array of finite diameter wires, described in section II. Wires of diameter $2R$ and alternating potential, $\pm V_{\text{app}}$, are spaced along the y -axis with a periodicity of d as shown in Fig. 5.4. Electrons passing in the positive x -direction would be deflected in the $\pm y$ directions. Electrons with an initial velocity at randomly selected times fall along a line $x = x_l$, for $-d < y < d$. The two bounds, between which explicit trajectory calculations were run, were defined at $x_l = -Nd$ and $x_r = Nd$, according to two criteria. First, the magnitude of the potential should be less than 0.1

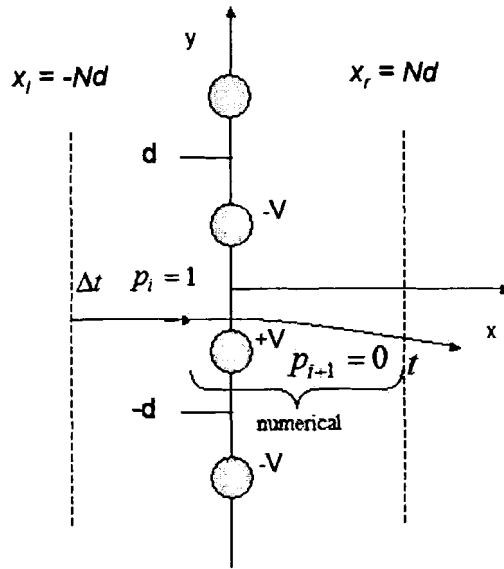


Figure 5.4. Schematic drawing of the trajectory simulation model used to generate noisy data. Electrons are started randomly in time at a position $x = x_l$ and y chosen randomly between $\pm d$. Trajectory calculations are carried out numerically within the “field affected region”, $x_l < x < x_r$, if the potential is on or analytically if the potential is off. In the example shown, the electron trajectory is calculated analytically for a time, Δt , during the remainder of the first modulation sequence step with potentials off, $p_i = 1$ (voltage off). In the next time step the potentials are applied ($p_{i+1} = 0$) and so the trajectory is calculated numerically for the portion of time step, τ , before the particle reaches the right boundary of the field affected region, x_r , and it is calculated analytically thereafter to the end of the modulation time step.

meV to assure the accuracy of the calculations. Examination of the potential shows that $\psi(x) \propto 4\lambda \exp(-\pi|x|/d)$ where λ is proportional to the magnitude of the applied voltage, V_{app} . In the simulations described here with $V_{app} = 0.4\text{V}$, when $x = -4d$, ψ is approximately 1.83×10^{-6} V which is already negligible. Second, the boundary should be chosen sufficiently far from the grid such that the final trajectory is independent of the initial x -position. For electrons of a particular energy and applied voltage, V_{app} , this condition was checked by comparing the chopper response as a function of the initial x -position, $X_i = -Nd$, with N varied between 1 and 40. Within statistical uncertainties, when $N \geq 2$, the difference of chopper response functions caused by the different initial positions is completely negligible. Thus, the electrons are treated as if there is no electrical field beyond the two lines and they can be considered to fly freely.

To allow for a distribution of energies and the random arrival of electrons at the chopper, we developed the following method, illustrated in the flow chart of Fig. 5.5, to generate PRBS-modulated data while minimizing the amount of trajectory calculation work. The region between x_l and x_r is treated as the field-affected region. For the electrons with velocity, v , we define $t_{aff} = \frac{2Nd}{v}$, which represents the time for the electrons to pass through the field-affected region. The time dependence of the potential is determined by the modulation sequence, which may change state on multiples of the time step, τ . In the experiment, the beam current is low ($\leq 10^6$ cts/s) and the arrival times are accumulated in a histogram over many cycles. In the simulation, it is more convenient to calculate the trajectory of a large number of electrons, n , at each step and cycle through the modulation sequence only once. In experiment, space charge effects are negligible and are therefore not considered in these calculations. In the i^{th} step of the

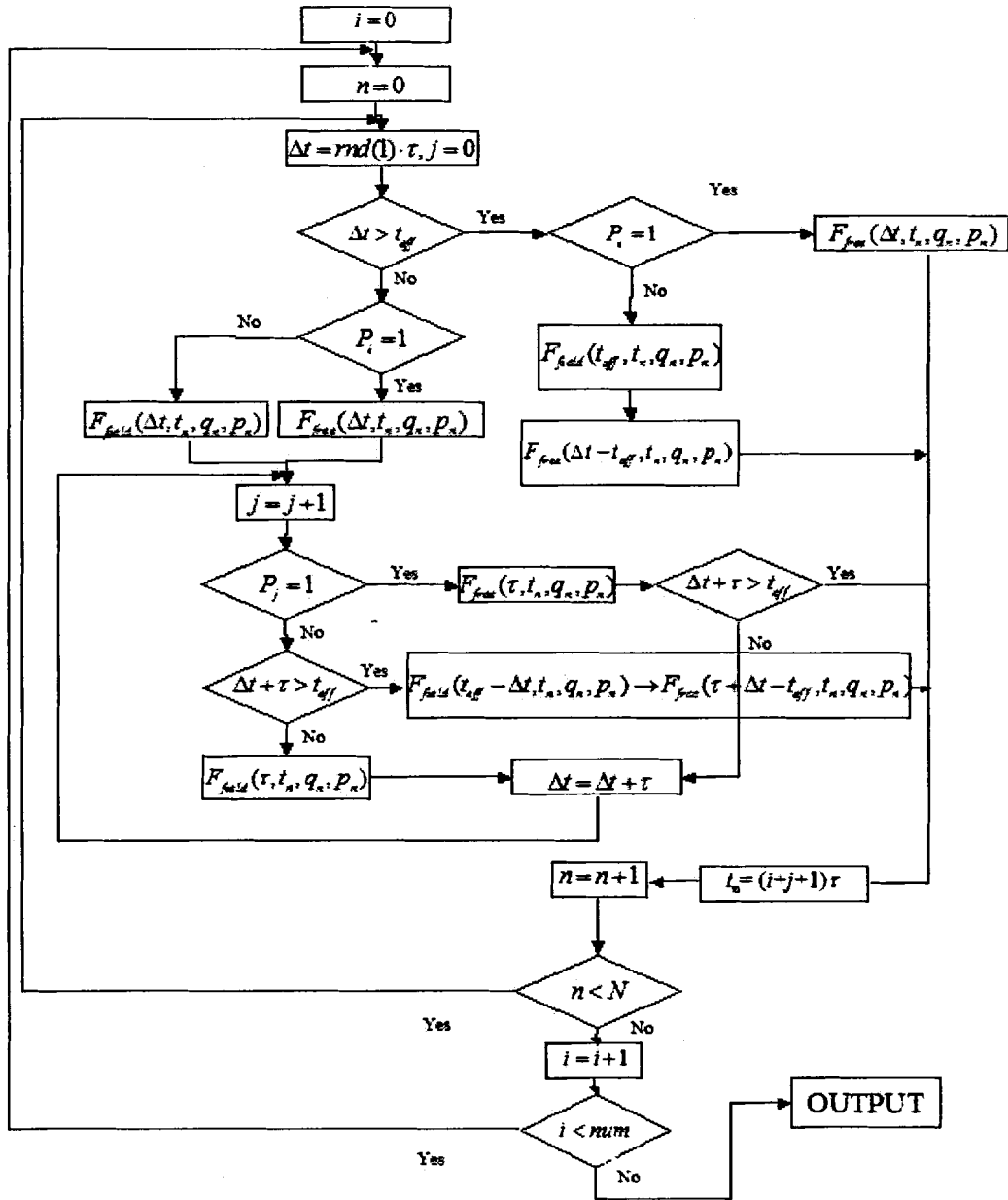


Figure 5.5. Flowchart of the trajectory simulation method. We define $F_{free}(\Delta t, t_n, q_n, p_n)$ and $F_{field}(\Delta t, t_n, q_n, p_n)$ as the functions that calculate the final time, t_{ns} , the coordinates, q_n , and momenta, p_n , after a time Δt_n , given the initial coordinates, q_n , and momenta, p_n , at time t_n , for the cases in which the potentials are off ($P_i = 1$) and on ($P_i = 0$), respectively.

modulation sequence, each of the n electrons arrives (is created) at $x = x_i$ randomly in time within the time step, τ , according to a random value, Δt , such that $0 < \Delta t < \tau$, and Δt is taken to be the time remaining within the i^{th} step of the modulation sequence. Two different possibilities exist. First, if $\Delta t > t_{aff}$, then the electrons will pass through the field-affected region within the i^{th} time step. If the chopper is open ($p_i = 1$), then the trajectory can be calculated analytically for Δt . If the chopper is closed ($p_i = 0$), then the trajectory is solved numerically over the applied potential for Δt . Second, if $\Delta t < t_{aff}$, then the electrons' information has to be recorded when the i^{th} PRBS time step ends so that during subsequent PRBS time steps, the motion of the electron can be treated according to whether the chopper potential is on or off. In successive steps, the accumulated time is compared to t_{aff} , and the trajectory calculations, either analytical (potentials off) or numerical (potentials on), are carried out until the electron clears the field-affected region. Any portion of a time step that remains is then calculated analytically, since the particle is, by definition, in the field free region. At the end of the first time step in which the electron has left the field-affected region, the position, velocity, and the time values are recorded.

In both the experiment and the simulation model, the PRBS sequence was the 8bit maximal length shift register sequence[58], with a total of $2^8 - 1 = 255$ time steps in the whole sequence. Each time step, τ , represents 8 ns, so the total length of the PRBS sequence is 2040 ns. In the experiment, the data was oversampled by a factor of 32, resulting in a bin size of 0.25 ns with a total of 8160 channels collected. The trajectory calculations were performed using an adaptive, fourth order Runge-Kutta method (Mathcad v. 2000, Mathsoft).

The results of the simulation were analyzed in a subsequent processing step. The instrument is designed to accept or reject electrons based upon their deflection angle, θ_{acc} . For a particular acceptance angle, the results of the trajectory calculation were sorted to include only those electrons with $\tan(v_y/v_x) < \theta_{acc}$ in the final time of flight histogram. The arrival time at the detector is calculated based upon the recorded time, position and the x component of velocity. Due to the cyclic nature of the PRBS sequence, the arrival time is calculated modulus the period of the sequence (here, $255 \times 8 \text{ ns} = 2040 \text{ ns}$), and binned into 0.25 ns intervals.

5.4. Results

We begin by presenting experimental data that illustrate the performance of the chopper and our ability to recover the object spectrum. We then turn to simulation results to illustrate the effect of several non-ideal characteristics of the chopper on the data inversion process.

5.4.1. Experimental Results

Fig. 5.6a shows the electrical signals applied to the chopper and, in 5.6b and 5.6c, the accumulated TOF signal at the detector for a section of the PRBS sequence with a potential of $\pm 0.4\text{V}$ applied to the chopper. The base time step is 8 ns. The traces in Fig. 5.6a, were measured with a 1.8GHz, 8G sample/s digital storage oscilloscope (LeCroy LC584AM, Chestnut Ridge, NY). They show that the signals applied to alternate pairs of wires are well balanced, with a rise time of 1 ns (10-90%), and a fall time (returning to 0V) of 1 ns. The sum of the two signals is the net potential on the grid. For our experimental conditions this is on the order of 10 meV. The field due to this potential

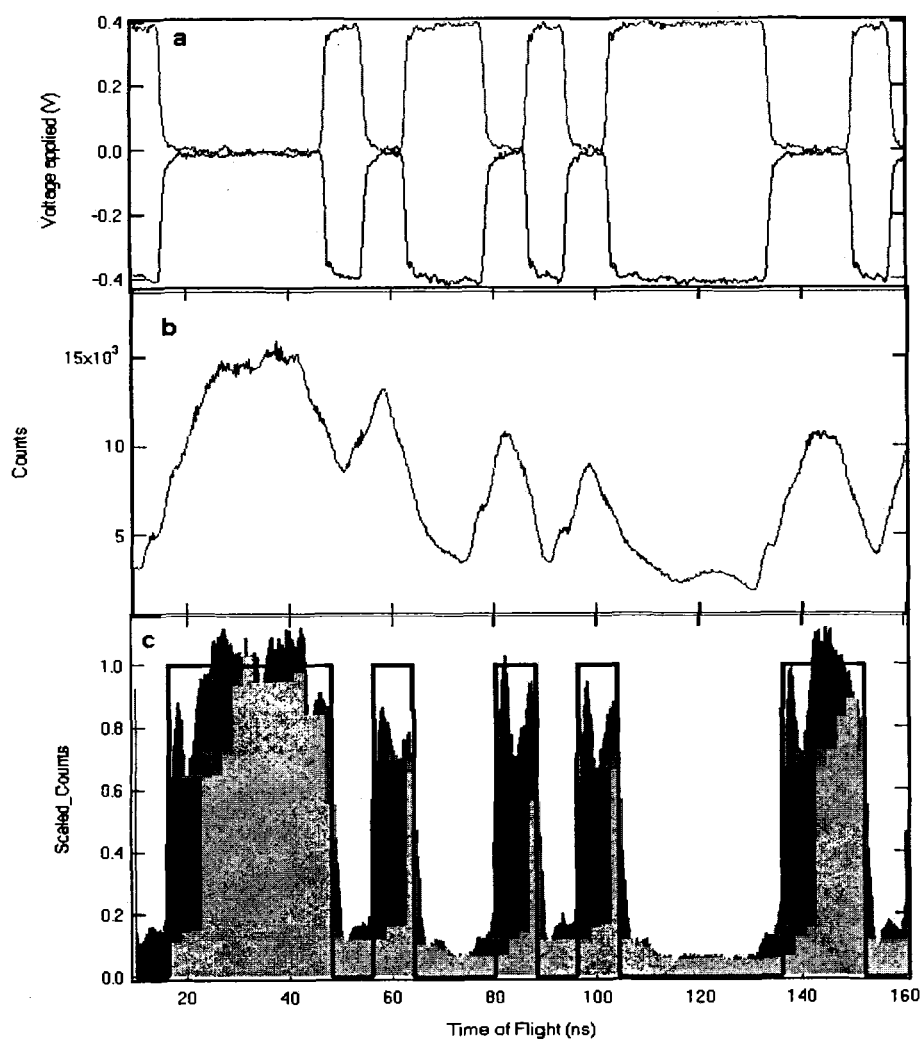


Figure 5.6. A section of the 255-bit PRBS modulation function showing a) the time dependence of the voltages applied to the chopper wires, b) the corresponding section of the TOF histogram measured at the detector with the 4 eV electron beam from the monochromator aimed directly into the chopper with the lens potentials off to illustrate the effects of scattering from the flight tube, and c) the improved TOF spectrum with the lens after the chopper is optimized. The effects of several non-ideal factors in the instrumental response function, as compared to the ideal PRBS modulation function (solid curve), are discussed in relation to the ability of the Lucy algorithm to recover the TOF data.

decays away as $1/x$, while the potential due to equal and oppositely charged parallel wires decays as $\exp(-\pi|x|/d)$. The TOF histogram in Fig. 5.6b shows the chopper response with the monochromator rotated so the beam is directed straight through the chopper. The time bin for acquiring data was 250 ps. The ideal PRBS sequence is shown in Fig. 5.6c (the black square curve). Although the collimation slits in front of the chopper limit the horizontal angular distribution to $\pm 1^\circ$, the vertical spread, together with any residual field, resulted in scattering from the flight tube walls. An Einzel lens directly after the chopper significantly improves the response function of the system, as illustrated in Fig. 5.6c. However, comparison with the ideal PRBS signal, also shown in Fig. 5.6c, reveals several non-ideal characteristics: 1) The rise time is finite; 2) the pulse widths differ from multiples of the nominal 8 ns time base; 3) the height of the single open bit is less than that of multiple open bit slots in the sequence; 4) there are oscillations accompanying the onset of the pulse; and 5) there is significant background during the “off” bits. We quantify two of these factors in Fig. 5.7.

As discussed in our previous paper[81], the chopper response has a lag or lead with respect to the applied voltage depending upon the position of the critical boundaries (see also section II and Fig. 5.1). This effect depends on the ratio of the particle’s kinetic energy to the potential on the chopper, the scale of the chopper and the acceptance angle. For the conditions of our experiments, $\xi = \frac{KE}{V_{app}} \cdot \theta_{acc} = 10$, the chopper is effectively open for periods of time which are less than an integer multiple of 8 ns; and effectively closed for periods which are greater than an integer multiple of 8 ns. Because the capacitance of the shift register may cause a different lag depending upon how long the gate has been open, it is important to distinguish lags in the drive electronics from that of the chopper

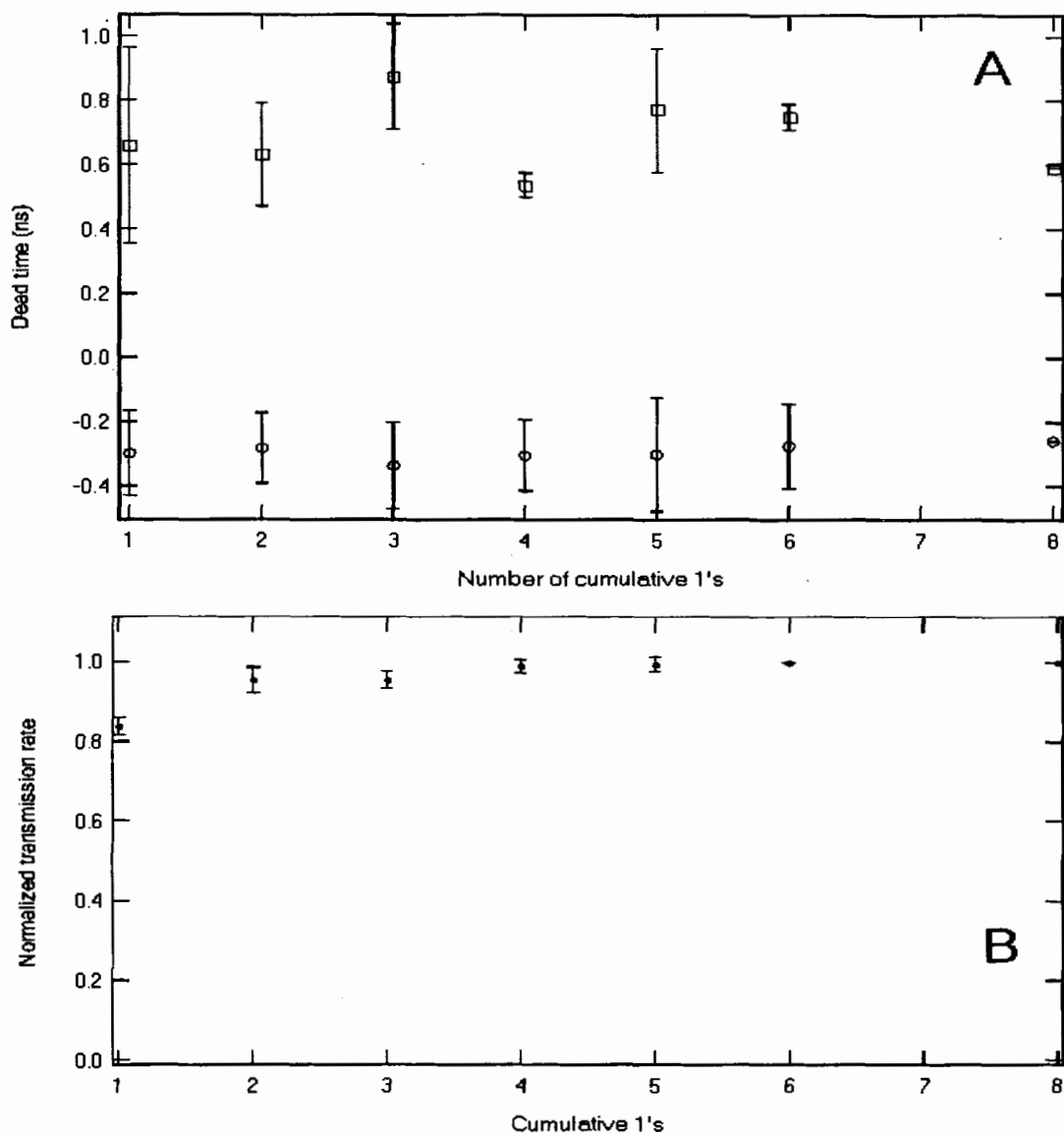


Figure 5.7. Analysis of the effects of A) the dead time of the drive electronics (circles) and the response function of the system (squares) as a function of the number of consecutive 1's (transmission on) in the PRBS sequence; and B) the transmission during the open periods. The data show that the response function turns on late and turns off early (positive deadtime) and that the transmission is significantly lower for a single 1 than for multiple consecutive 1's in the sequence. The transmission rate is normalized to unity at average count rate of the 8 consecutive open time bits in the PRBS spectrum.

itself. In Fig. 5.7A, the relationship between the deadtime and the number of cumulative 1's was quantified for both the PRBS signal applied to the chopper and the chopper response. Here, we defined the deadtime as $8 \cdot N - t_{open}$, where t_{open} was measured as the time between the half-height (0.2V) of the falling edge and the next rising edge of the electrical signals (circles) and as the FWHM of the pulses in the TOF histogram for the chopper response (squares). The error bars are the standard deviation in values for all occurrences in the PRBS sequence (except for 8 cumulative 1's, which only occurs once in the sequence). The variation in the deadtime is small for the drive signal, suggesting that the variation in the chopper response is mostly due to the difficulty in quantifying the peak widths. The chopper shows a significantly larger deadtime than the electronics. The magnitude is approximately that expected from the position of the critical boundaries, shown in Fig. 5.1 (Section II), for a particle velocity of $2 \times 10^6 \text{ m/s}$ and $d = 250 \mu\text{m}$. The resulting decrease in duty cycle (below 50%) due to the lead/lag effects discussed just above will generate characteristic artifacts in the spectra, when recovered by the cross-correlation method, which can be seen in the auto-correlation function described below (Fig. 5.8).

The variation in the height (or transmission) of the pulses is shown in Fig. 5.7B. The average height of the single open slots (time width 8 ns) is significantly smaller than the height of the multiple open slots (16 ns or more). This difference in height is significantly larger than the Poisson noise distribution width (cf. Fig. 5.6c). The origin of this artifact is partly the finite rise time, which derives from the finite extent of the chopper potential as well as the rise time of the chopper signals. However, it may also be due to the oscillations in the onset of the pulse, which may be associated with cavity

modes in the chopper assembly[84]. The background (cf. Fig. 5.6c) is attributed to scattering off the flight tube walls.

We now turn to the characteristics of the entire PRBS modulation function, which will be used for data recovery. In order to evaluate how the PRBS modulation function depends on the range of angles impinging on the entrance apertures, we varied the monochromator angle about the straight through position. To reveal the variation among the chopper response functions at different angles, we give the normalized autocorrelation functions in Fig. 5.8. The autocorrelation function of the ideal discrete PRBS sequence is a δ function. However, in our experiment, the gate remains open for a finite time (*i.e.* the entire 8 ns time step), and the TOF histogram is oversampled by a factor of 32. The corresponding autocorrelation function becomes a triangle function with base equal to twice the time step (16 ns). Over the 90-91.5° range, the oscillation amplitudes are approximately 5 percent of the central peak height, but do not vary substantially with angle. Between 89.5 and 89°, the features change with angle; however, the transmission is substantially reduced. Based on theoretical simulations, the reduction in the duty cycle due to the deadtime causes the artifacts near ± 495 ns and the decrease in transmission for a single open slot produces artifacts near ± 856 ns and ± 936 ns in the auto-correlation function. All these artifacts are small in the experimental data. We have not yet found a completely satisfactory experiment for the features near ± 610 -700 ns.

After optimizing the chopper response by tuning the Einzel lens on the monochromatic beam, we measured the PRBS-TOF spectrum of an azimuthally- oriented sample. Fig. 5.9 compares the loss spectrum measured with the conventional analyzer to

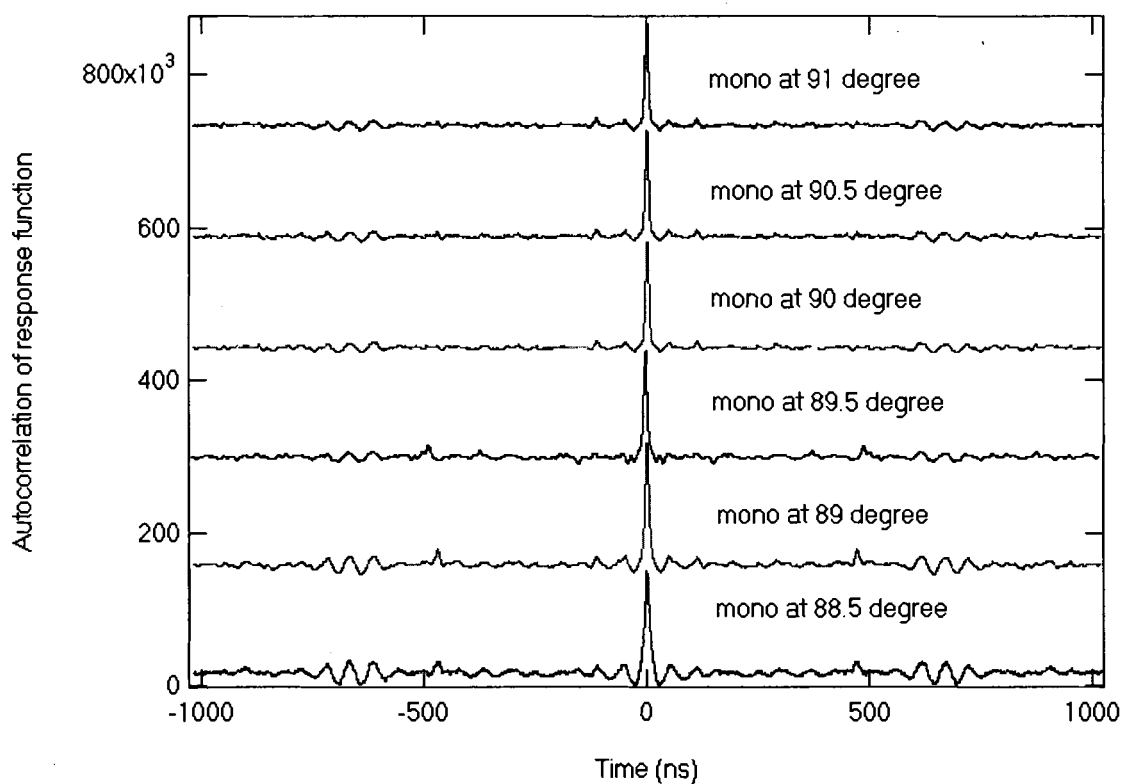


Figure 5.8. Auto-correlation functions corresponding to chopper response functions measured for a range of different monochromator angles, illustrating substantial artifacts that vary significantly with the angular distribution feeding the chopper.

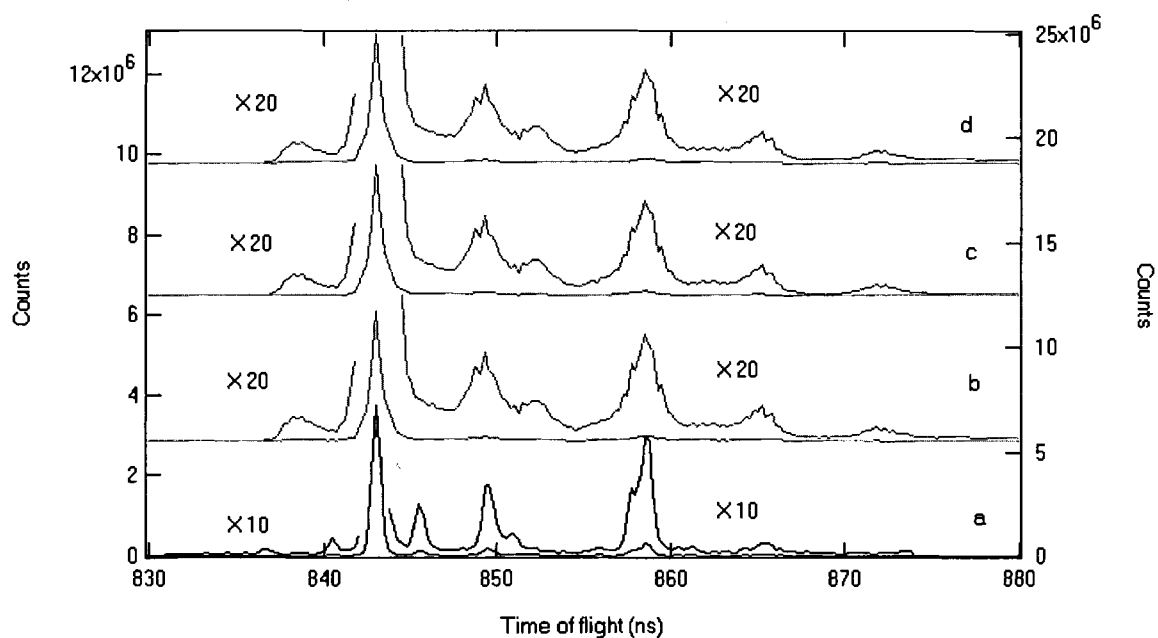


Figure 5.9. Comparison of the vibrational loss spectrum of an azimuthally-oriented PTFE film, measured on-specular (60°) with a primary beam energy of 4 eV using a) the conventional HREELS analyzer, with the spectra measured by the TOF detector and recovered using chopper response functions for mono angles of b) 89.5° , c) 90° , and d) 90.5° . The PRBS-TOF spectrum was collected in 1 minute, compared to the conventional spectrum data acquisition time of 2.3 hrs.

the spectrum obtained by Lucy algorithm to deconvolute the PRBS-modulated data from the PTFE film using the chopper response functions measured at several monochromator angles. The conventional spectrum, curve a, was measured in 2.36 hours; by contrast, the PRBS-TOF spectrum required approximately 1 minute of data collection time, an improvement in throughput of approximately 85. The major peaks' flight times of 849 ns (65 meV loss) and 858 ns (150 meV loss) associated with the CF₂ rocking / wagging modes and the CF₂ stretches[85], respectively, are recovered with some decrease in resolution. In all of the PRBS-TOF spectra, additional artifacts are found at 838, 854, and 873 ns, with extra intensity in the peak near 866 ns. The loss and gain features at ± 2.5 ns are not resolved from the base of the elastic peak.

To summarize the experimental results, we demonstrate a significant performance (throughput) advantage, although the resolution of the spectrum is not as good as the conventional HREELS spectrum. The collimation slits restrict the angular distribution to achieve a response function independent of the source (or sample) position for the angles of largest transmission. Variations that occur for smaller angles do not affect the quality of the recovered spectrum. The loss in resolution, the presence of artifacts at the 5% level, and variations in relative intensity are significant problems. We use theoretical simulations to consider the origin of these problems in the following section.

5.4.2 Simulation Results

We begin with simulations of the chopper response function and the PRBS-modulated data corresponding to the PTFE spectrum. In Fig. 5.10a, the chopper response, $p(t)$, includes an incoming electron beam, $o(E)$, at 4 eV with a Gaussian energy

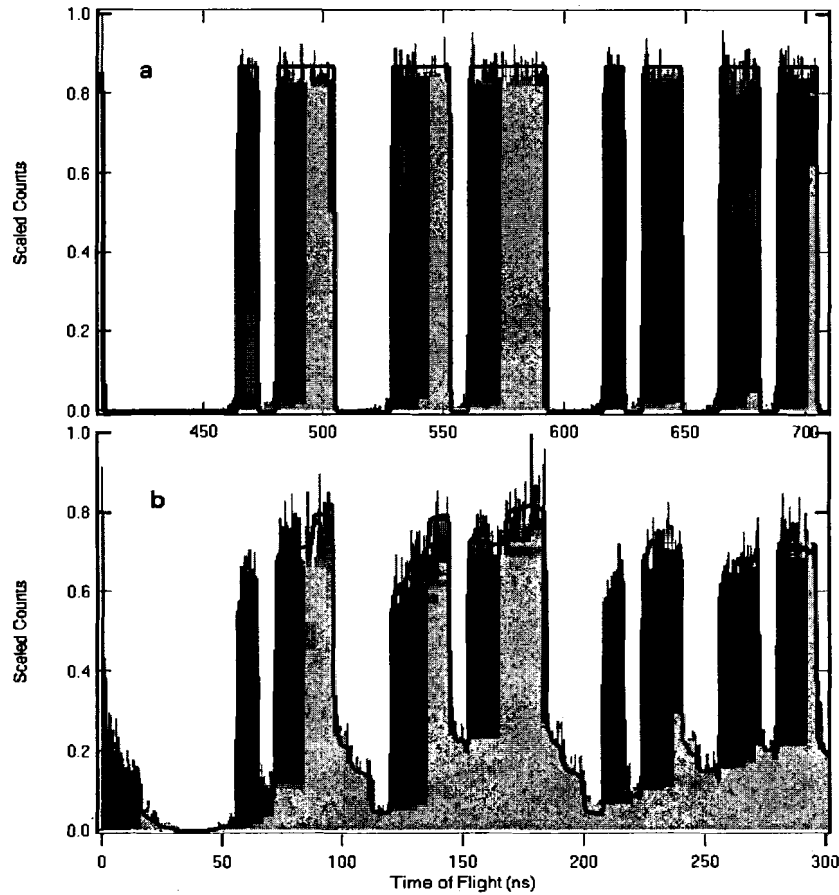


Figure 5.10. Simulation of a) the chopper response function for a 4 eV beam with a Gaussian distribution of 4 meV FWHM, and b) the corresponding TOF histogram with an energy distribution corresponding to the Teflon spectrum in Fig. 9 a. Trajectory simulations (histograms) were calculated as described to include the Poisson noise distribution (shown for a total of 4×10^6 counts distributed among 8160 time bins), energy corruption effects, lead/lag effects, and the contribution of the finite field penetration of the $d = 250 \mu\text{m}$ chopper used in the experimental setup. For comparison, the ideal PRBS modulation function is shown (solid curve) after convolution with the TOF spectrum corresponding to the energy distributions for a) the monochromatic beam and b) the Teflon HREELS spectrum of Fig. 9a.

distribution ($\phi(E)$) of 4 meV FWHM. In Fig. 5.10b, the energy distribution ($\phi(E)$) of the PTFE spectrum, measured with the conventional analyzer, was converted to a TOF distribution. The sections of the time-modulated data shown in Fig. 5.10 have been calculated in two ways. The solid curves are simply a convolution (using FFT's) of the appropriate energy distribution (converted to time-of-flight) with the ideal PRBS sequence. The histograms in Fig. 5.10 were calculated with the method described in Section III B.

The trajectory calculations include the lead and lag effects, energy corruption, the Poisson noise distribution associated with the counting experiment, and deviations from a true convolution (as discussed in Sect. II). The simulations do not include the experimental factors of the finite rise time of the chopper voltages, the $\pm 1^\circ$ angular distribution of the electrons incident on the chopper (all electrons have a component $v_y = 0$), electrical signal errors such as miscancellation of the applied voltage and possible coupling to cavity modes, or scattering from the chopper wires themselves. The data were calculated for a chopper of dimensions similar to the experimental data of Fig. 5.6 ($d = 250 \mu\text{m}$, $R = 12.5 \mu\text{m}$, $\theta_{acc} = 1^\circ$, $V_{app} = \pm 0.4\text{V}$) with a total of 4 million counts in the entire 8160 bin histogram.

Comparison of the convolution (solid curve) and trajectory simulation data in Fig. 5.10 shows good agreement, demonstrating that the time-modulated data is, to a very good approximation, a convolution. The energy corruption generates a tail to shorter flight times, most clearly seen in histogram a. Although the probability of gaining or losing energy is equally likely, conversion of a symmetric distribution of energies to a time-of-flight distribution results in an asymmetric distribution. Expansion of the

histograms shows that the solid curves (convolution) pass through the noise, and a histogram of counts/bin during the open time (Fig. 5.10a) confirms that the simulation has a Poisson noise distribution. The lag effect is also evident upon careful examination of the simulated data. The width of the histogram pulses are approximately 0.9 ns narrower than the convolution data in the chopper response function (part a), which is similar to the 1.2 ns difference shown in the results of Fig. 5.7A.

With the simulated chopper response functions and the PRBS-modulated PTFE data of Fig. 5.10, we used the Lucy algorithm to estimate the TOF spectra, shown in Fig. 5.11. Curve a is the object function used in the simulation and b is the recovered spectrum from the experimental data. Curve c shows that the Lucy algorithm is able to accurately recover the object spectrum when the data, $y(t)$, was generated by convolution of an ideal chopper response function, $P_{id}(t)$, with the TOF object function (curve a) and no noise was present. Curves d, e, and f correspond to results from the trajectory calculations for choppers of different scale; Curve f ($d = 250 \mu\text{m}$) corresponds to the experimental chopper dimensions. The assumption of the convolution should improve as the scale of the chopper is reduced. These recovered spectra show the more intense features in the correct positions, but the splitting of the band at 857-858 ns is lost. The recovered spectra of curve d ($d = 50 \mu\text{m}$) and curve e ($d = 5 \mu\text{m}$) are improved to some extent, especially on the 2.5 ns gain and loss peaks, but the weak dependence on the scale of the chopper suggests that other factors are more important.

The factor which most dramatically affected the recovery of the simulated data is the estimation of the chopper response function from the noisy data. The assumption of the Lucy algorithm is that both the underlying object function and the response function

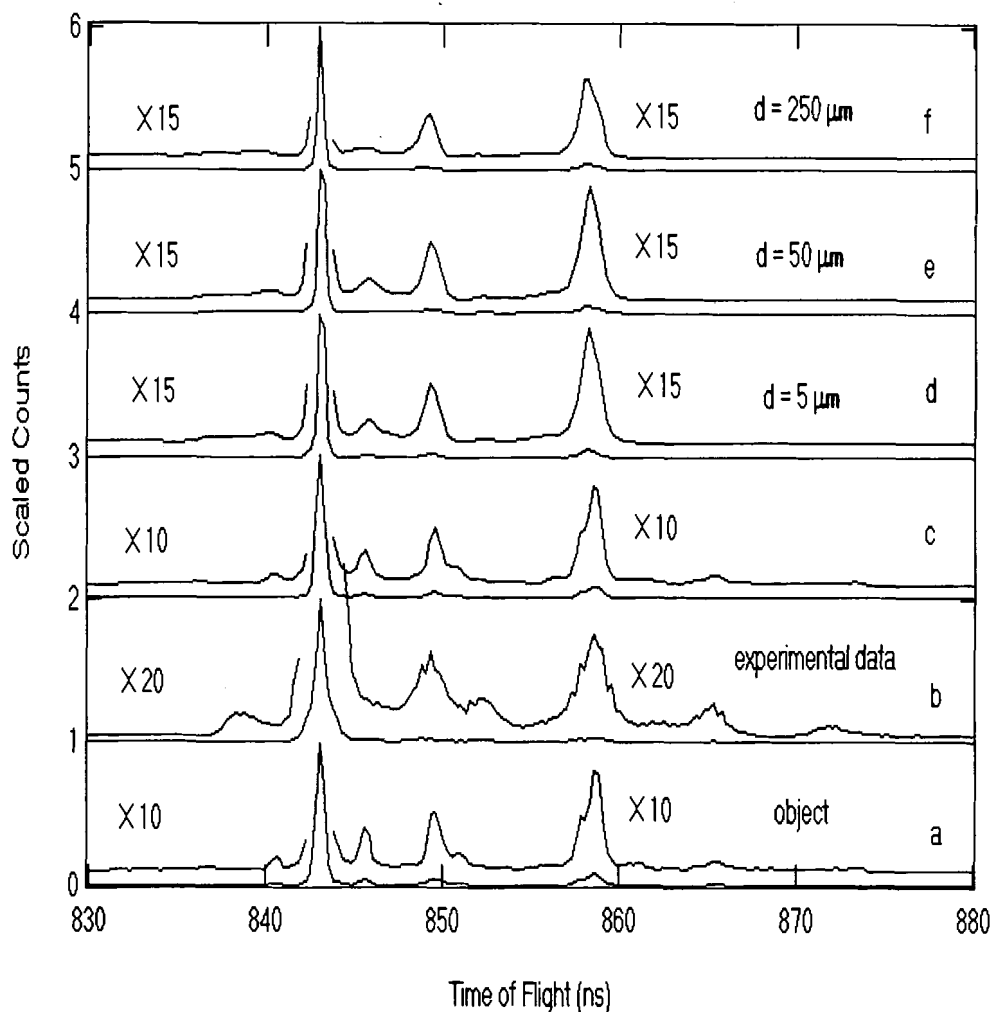


Figure 5.11. Comparison between a) the TOF spectrum (object function) corresponding to the Teflon HREELS spectrum of Fig. 5.9a, b) the recovered PRBS-TOF spectrum of Fig. 9c, and the results of using the Lucy algorithm to recover simulated data, c) from the convolution data (solid curve, Fig. 5.10b) using the response function (solid curve, Fig. 10a), shows that, at 4 eV a 1 m flight path, a PRBS time step of 8 ns, oversampling of the data by 32 (0.25 ns time bins), and in the absence of noise, the Lucy algorithm recovers the features very well. By contrast, the recovery of simulated data generated with the trajectory method for choppers of different wire spacing (d-f) results in somewhat degraded resolution, but not the artifacts found in the experimental results.

are noise-free. In a separate paper[86], we have shown that the presence of Poisson noise in the response function, even at a S/N ratio in excess of 1000, causes noise and peak distortion in synthetic data. Most smoothing algorithms are not useful here since they degrade the resolution of the response function and create artifacts in the recovered spectra.

Frederick and DeNoyer [86] have shown that a better estimate can be obtained by using the ideal (square wave) PRBS sequence to deconvolute the chopper response function. In essence, an effective broadening function, $s_{eff}(t)$, is estimated from

$$p(t) = \sum_{i=1}^N h_i(t) \otimes g_i(t) \approx s_{eff}(t) \otimes p_{id}(t) \quad (5.6)$$

where $z_i(t)$ (in Eq. 5.5) reduces to $h_i(t)$, and where $o(E) = \delta(E - E_0)$. Note that $\sum_i g_i(t) = p_{id}(t)$ is the ideal PRBS response function. Thus, $s_{eff}(t)$ contains the energy distribution of the primary beam, the energy corruption and other system limitations. After obtaining $s_{eff}(t)$ using the Lucy algorithm, the estimated response function, $p_{est} = s_{eff}(t) \otimes p_{id}(t)$, is calculated. Examination of the residuals shows that the noise is zero-distributed with Poisson character. Comparison with the true response function in synthetic data revealed that the maximum relative error, $[p_{est}(t) - p(t)] / p(t)$, could be reduced to less than 10^{-3} with this method.

For the spectra shown in Fig. 5.11, curves d-f, the method was further refined, since the deadtime results in a pulse width narrower than in the ideal PRBS sequence. Thus, $s_{eff}(t)$ was obtained by deconvolution of the simulated response function, $p(t) = s_{eff}(t) \otimes p_d(t)$, using a PRBS sequence, $p_d(t)$, in which the duty cycle was

reduced from 50% to 47% by narrowing the width of the pulses (as discussed below with regard to Fig. 5.13). While this approach to estimating $p(t)$ tremendously improved the spectra recovered from the simulated data, the procedure did not eliminate the artifacts in the experimental spectrum.

To distinguish between the various artifacts observed in the experimental data, we performed a direct convolution of the object function (*i.e.* the PTFE TOF spectrum of Fig. 5.9a) with chopper response functions which were non-ideal in some respect. Fig. 5.12 shows the results for a response function in which the data cycle was decreased (part A) and increased (part B) by introducing a lead or lag. In the case of a decreased duty cycle, the artifacts generated in the autocorrelation are negative-going, while a duty cycle greater than 50% creates the artifacts which are positive-going[64]. The position of these artifacts in the cross-correlation result, shifted by 62 bits, is well defined and occurs at ± 495 ns with respect to each of the real features[64]. In the spectra of Fig. 5.12, this artifact is negligible after 10,000 iterations and the features are accurately reproduced, suggesting that the deadtime of the chopper is not a major experimental concern.

Figure 5.13 shows results in which the response function is ideal in all respects except that the height of the single open slots are reduced relative to the rest of the sequence. The recovered spectra for 80% reduction of the single open slots are shown for a range of iterations in part A. While the estimate at 1,000 iterations is comparable to the object function, further iteration leads to better resolution (particularly in the 845.5 and 858.5 ns peaks), but then artifacts appear (eg. at 835ns) and the 851 ns feature splits and the intensity redistributes. As the reduction in height deviates further from an ideal modulation sequence, as shown in Fig. 5.13B, the estimate after 1000 iterations degrades.

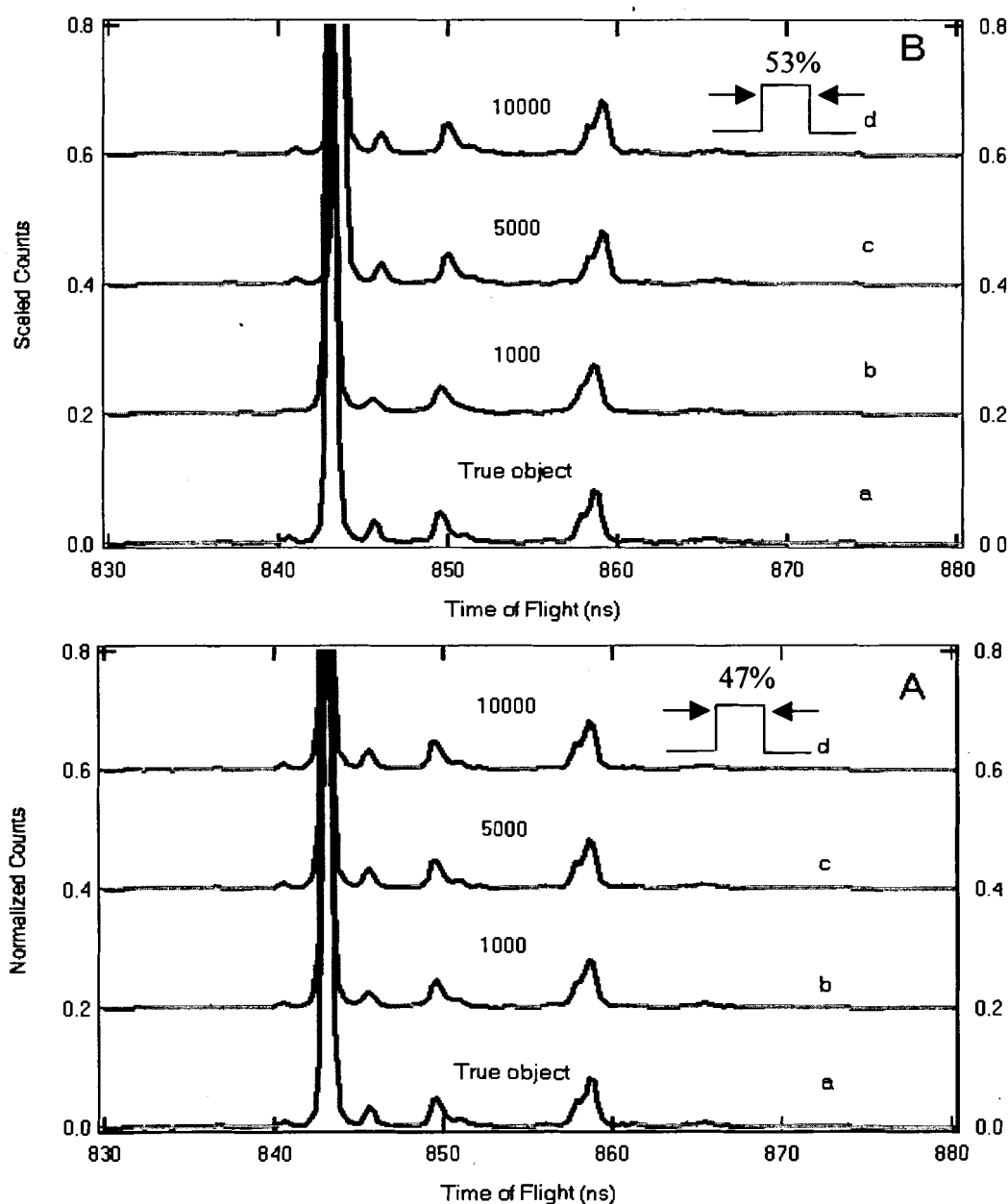


Figure 5.12. A) Comparison of a) the object function used to generate noise-free modulated data by convolution with a PRBS response function that is ideal except that the dead time leads to narrower pulse widths, resulting in a duty cycle of 47% rather than 50%, with recovered spectra using the Lucy algorithm after b) 1000 iterations, c) 5000 iterations, and d) 10,000 iterations. B) The corresponding results in which the duty cycle is increased to 53%.

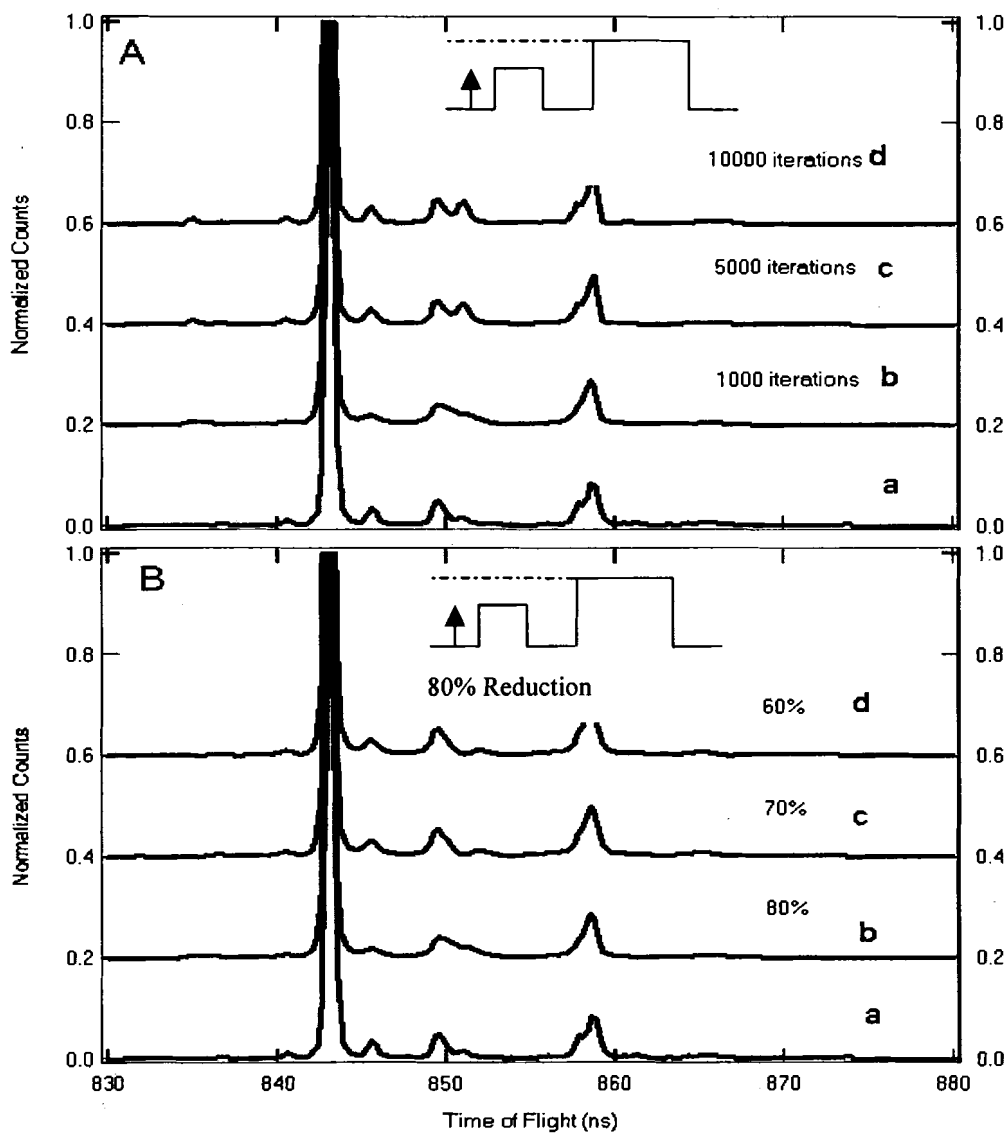


Figure 5.13. A) Comparison of a) the object function used to generate noise-free modulated data by convolution with a PRBS response function that is ideal except that the height of single 1's is reduced to 80%, with recovered spectra using the Lucy algorithm after b) 1000 iterations, c) 5000 iterations, and d) 10,000 iterations. Notice that loss of information results in artifacts and re-distribution of the peak intensities. B) Results after 1000 iterations for data generated as in A) but for the height of single 1's reduced to b) 80%, c) 70%, and d) 60%.

This suggests that a major limitation of the current experimental system is the chopper response time, leading to decreased transmission in the single open bits of the PRBS sequence (as illustrated in Fig. 5.6c).

5.5 Discussion and Conclusions

In designing an instrument, the principal performance characteristics are the resolution, sensitivity, and integrity of the measured spectrum. We first address the factors that contribute to the intrinsic time resolution of the instrument, which would be observed in a single pulse TOF experiment, and then discuss the additional factors which effect the resolution of the recovered spectra in the PRBS-modulated mode. Next, we discuss the origin and fundamental limits that artifacts place on the dynamic range of the instrument, using the Lucy algorithm for data recovery. Finally, we assess the multiplex advantage obtained in the present instrument.

5.5.1. Intrinsic Time Resolution (Single Pulse Mode)

The traditional definition of resolution in a single pulse TOF instrument is simply the width of the pulse[64]. However, in our implementation of the Hadamard or PRBS modulation approach, the information concerning the flight times of different energy (or mass) particles is contained in the phase shifts of the cyclic PRBS sequence formed by particles of different energy. Therefore, the rise time of the pulse is of greater interest in our ability to recover the spectrum than the pulse width, as we will discuss in section B. To characterize the time resolution, we will associate the derivative of the step response function with the point spread function in the time domain.

The dominant contribution to the time resolution of the present instrument is that of the chopper response function. In Sect. II we developed a model of the chopper response function, in terms of the applied voltage, kinetic energy, wire spacing and wire diameter. We distinguished two non-ideal characteristics of the response function of the chopper, $p(t)$: the lag of the signal with respect to the time that the voltages are applied, and energy corruption due to the spatial extent of the fields. The critical boundaries determine, for a specified acceptance angle and ratio of chopper voltage to kinetic energy, which electrons reach the detector. The critical boundary can be before or after the plane of the chopper, so at short distances the response can lead or lag the applied voltage. However when the distance from the chopper to the detector is large, the energy corruption will always causes a lag in the effective chopper response. To illustrate this, we show in Fig. 5.14 the energy corruption histograms of Fig. 5.2, converted to TOF histograms for a 1 m flight path. The fraction of electrons within a spatial region that are after the critical boundary ($x > c(y)$) at the time the potential is switched off is initially small, but increases to 100% over the first 5 regions of 12.5 ps time width. Therefore, the transmission of the grid reaches 100% within approximately 60 ps. However, the response function at the detector is much slower.

As curve a in Fig. 5.14 shows, the transmitted electrons arrive at the detector over a large range of times. The corresponding TOF histogram for the 6th time bin, in which the transmission is nearly 100%, has a time width of approximately 24 ns. As the potential decays spatially from the plane of the chopper, the corresponding TOF histograms narrow (and shift) and their contribution to the height of the time dependent response function increases. We show in the Fig. 5.14B the cumulative TOF histograms,

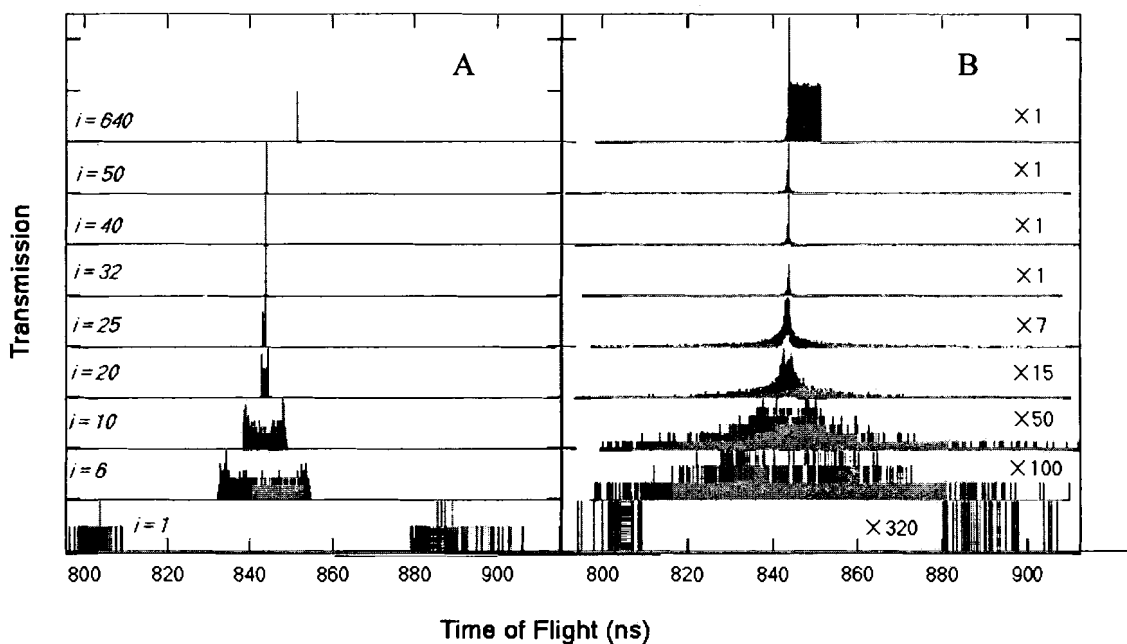


Figure 5.14. A) The TOF histograms converted from the energy corruption histograms of Fig. 5.2. for selected rectangular regions. In the Monte Carlo integration, 10,000 electrons were chosen randomly in each region. B) The corresponding cumulative TOF histograms from 1 to i^{th} bin, as indicated in A) to illustrate the contributions of different spatial regions to the overall TOF histogram. The vertical scales have been multiplied by the factors indicated.

i.e. $\sum_{i=1}^n h_i(t)$. In this case, it is not until the electrons from the 33rd rectangular region (curve c) are added to the distribution that the response function reaches 0.5, of the steady state height. This implies that the lag of the chopper response is $33 \times 12.5 \text{ ps} = 412.5 \text{ ps}$. In the case of a Gaussian point spread function, the rise time from 10 to 90% corresponds to 1.68σ where σ is the standard deviation of the distribution. In this case, the 10-90% rise time is approximately 0.5 ns which gives the $\sigma = 0.3 \text{ ns}$. In general, as the d -spacing is decreased, both the lag and the rise time decrease. We show in Fig. 5.15 the onset of a pulse, calculated in the same way as in Fig. 5.14, for choppers of three different wire diameters, but all with $2R/d = 0.1$. The lag and rise time are shown in parts B and C, respectively, as a function of d . The lag time and the rise time both can fit as a quadratical function of the d -spacing. According to the fitting, when d approaches zero, the lag and rise time approaches zero ps. Therefore, we predict that decreasing the wire dimensions will be a benefit in getting a reduced lag and rise time, which is helpful in achieving a higher resolution.

In these simulations, we have assumed that the chopper voltages are turned on instantaneously. In the experiment, the slew rate of the output driver electronics is approximately 0.4 V/ns. For finite rise times, we can estimate the contribution to the chopper response function in the following way. The deflection angle of the beam varies with applied voltage as $\theta = \frac{V_{app}}{KE} k$, where k is characteristic of the chopper transmission. For $2R/d = 0.1$, $k = 17^\circ$. If a beam of width w is to be excluded by a slit, also of width w , and the initial angular distribution has limits of $\pm 0.5^\circ$, then the deflection angle must be 1° to completely turn off the beam. Since the deflection is approximately linear in

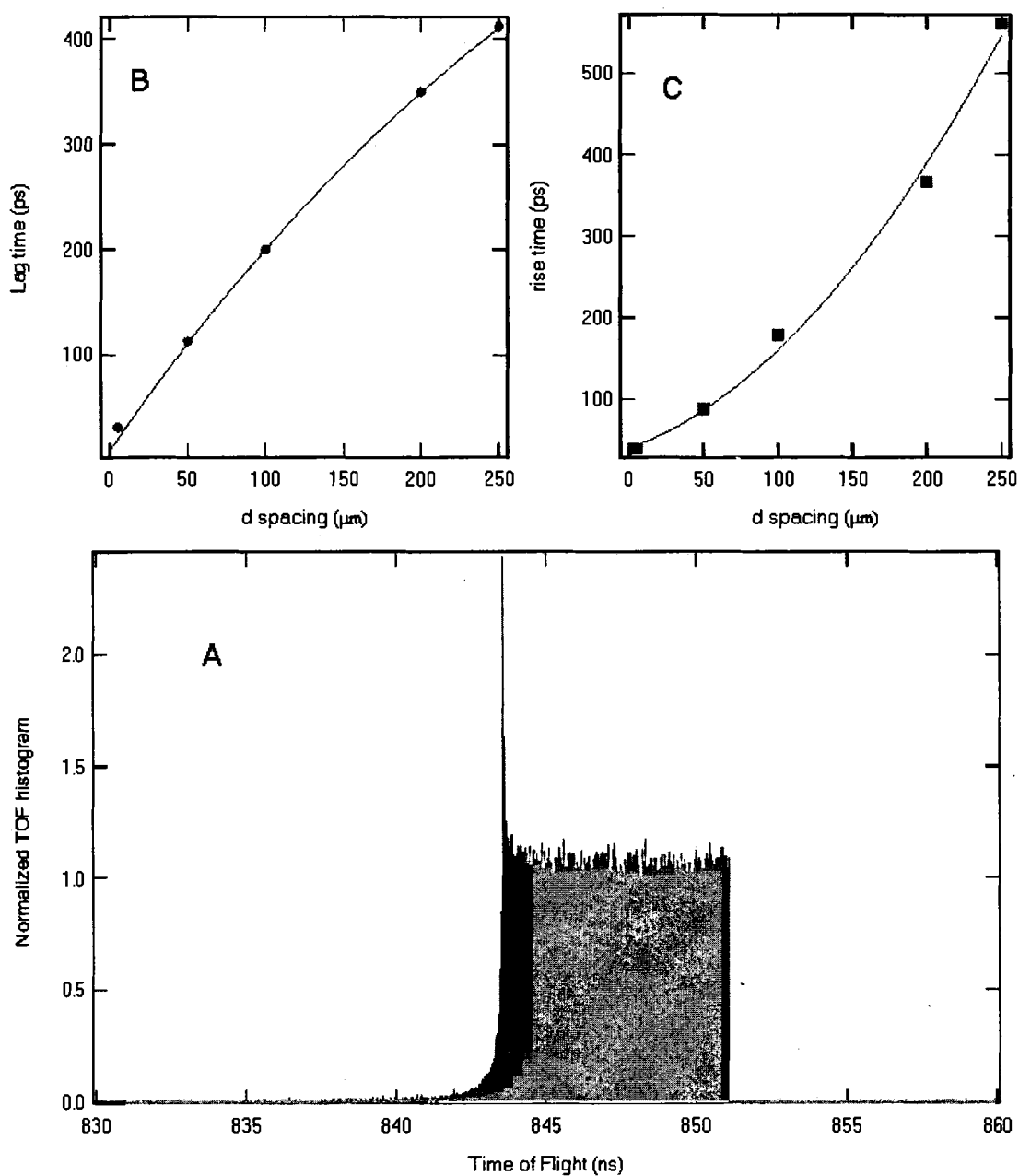


Figure 5.15. A) The onset of a chopper response function for 4 eV beam with $2R/d = 0.1$. B) The relationship between the lag time and d -spacing. C) The relationship between the rise time and d -spacing. Both B) and C) are based on the 4 eV beam simulation.

voltage (for the small angles), the contribution of the voltage time dependence to the chopper response should be approximately linear. Therefore, the time to turn off the electron beam completely is about 0.6 ns. Since the observed time is of this order, it appears that the minimum fall time is limited by the finite rise time from the drive signal. The next largest contribution to the measured step response function is the energy spread of the primary beam. The dependence of the rise time (10-90%) on both beam energy and the FWHM, ΔE , of the monochromatic beam, is shown in Fig. 5.16. At higher beam energies, the energy spread contributes less to the time-dependent response function. For the 4 eV, 4 meV beam, conditions that apply to the experimental data, the rise time is 0.3 ns, which is a small but significant contribution to the observed chopper response function.

We have also quantified a number of other potential sources of broadening. Probably the largest of these is the jitter in the time-to-digital converter. The base time clock of the Fast Comtec TDC was adjusted to 125 MHz, and an internal phase lock loop provides interpolation of events to achieve a bin size of 250 ps. Examination of the jitter in the phase lock loop suggests that the uncertainty in the TDC is closer to 350 ps, as characterized by the standard deviation of the Gaussian-like jitter histogram. By contrast, the jitter in the PRBS generator (shift register), the chopper driver output stage electronics, and the pre-amp and discriminator is of order 10's of ps. The pulse width of the AP-TOF detector is approximately 750 ps, with a rise time of 350 ps. Recently, improvements in commercially available multichannel plate detectors have demonstrated pulse widths of 400 ps with a rise time of 200 ps.

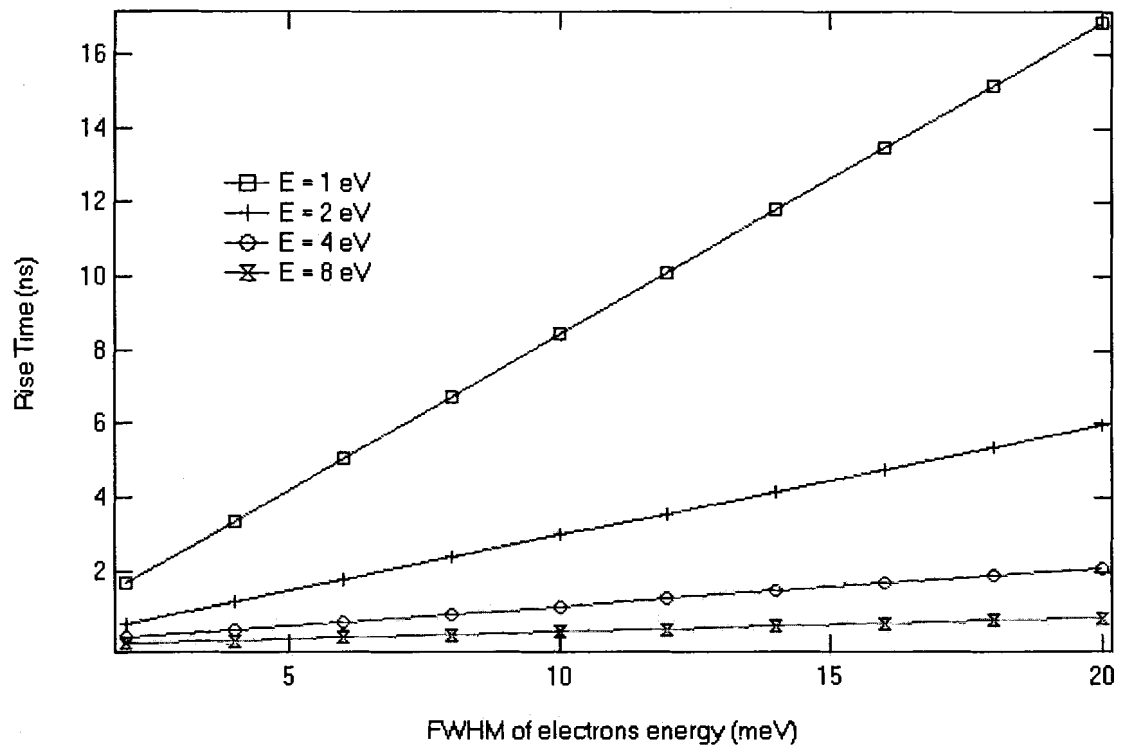


Figure 5.16. The dependence of the rise time (10%-90%) on beam energy and the FWHM of the monochromatic electron beam.

5.5.2. Resolution in Spectra Recovered from PRBS Modulation

The performance of the maximum likelihood (ML) algorithm is dependent upon a number of factors. The resolution depends strongly upon the frequency content of the chopper response function, but also on the signal-to-noise level of the data and the number of iterations. The effect of these factors can be quantified in a relatively straightforward way. Other factors, such as a broad signal background, deviations from the assumption of a convolution, and errors in defining the response function, are more difficult to assess. In a separate paper[86], we have used synthetic data to quantify the resolution enhancement and dynamic range that can be expected for a simpler case in which there was no background present, the spectrum consisted of several Gaussian peaks, and the assumption of a convolution was valid. First, we make comparisons to those results and then discuss the effects of the background and the validity of the convolution assumption.

In the situation that the PRBS time step, τ , can be made small with respect to the width of the narrowest features in the spectrum, the cross-correlation recovery method should be able to accurately measure the width of the features. In our case, the interactions between the chopper grid and the charged particles preclude operation in this regime. Typically, τ is chosen to be as much as a factor of 8 larger than the desired time resolution and the Lucy algorithm is used to improve the resolution relative to the nominal time resolution, τ . For the case of a feature whose width is narrow compared to τ , we have defined the resolution enhancement as the PRBS time step divided by the width of the recovered peak. The resolution enhancement has been shown to depend strongly on the ratio of the rise time to τ [86]. In the synthetic data, the ideal response function was

broadened by a Gaussian. As a result, the rise time is simply related to the rise time of the Gaussian (measured between 10 and 90%). This Gaussian rise time is equal to 70% of the FWHM of the Gaussian.

In the experimental data of Fig. 5.6, the rise time is approximately 1 ns, although the oscillations that occur at the leading and following edge decay over several nanoseconds. An alternative way to assess the bandwidth of the chopper response function is to plot the magnitude of its Fourier transform, as shown in Fig. 5.17. The magnitude of the Fourier transform of the ideal response function is $|\sin(x)/x|$. We model the real PRBS response function as the convolution of a Gaussian with the PRBS sequence. The time step, τ , was chosen to be 64 and the FWHM of the Gaussian broadening was varied from 4 to 16m such that the ratio of the rise time to time step varied from 1/16 to 1/4. In the frequency domain, the $\sin(x)/x$ is multiplied by a Gaussian, which rapidly decrease the higher frequency content of the chopper response function. This in turn means that the higher frequency information in a particular object function will also be lost. When the ratio of the rise time to τ reaches 1/8, the amplitude becomes small by the first zero in $\sin(x)/x$. Therefore, comparing the Fourier transform of the experimental response function to the Gaussian-broadened response functions, an estimate of the rise time/ τ ratio of 1/16, or an effective rise time of ~ 0.5 ns is perhaps reasonable. We note that this is similar to the rise time in the trajectory simulation for the 250 μm chopper.

In the absence of noise and with an ideal PRBS response function, the TOF spectrum can be recovered with errors of order 10^{-6} , as shown in Fig. 5.11. However, as the rise time increases and the signal-to-noise ratio decreases, the resolution of the

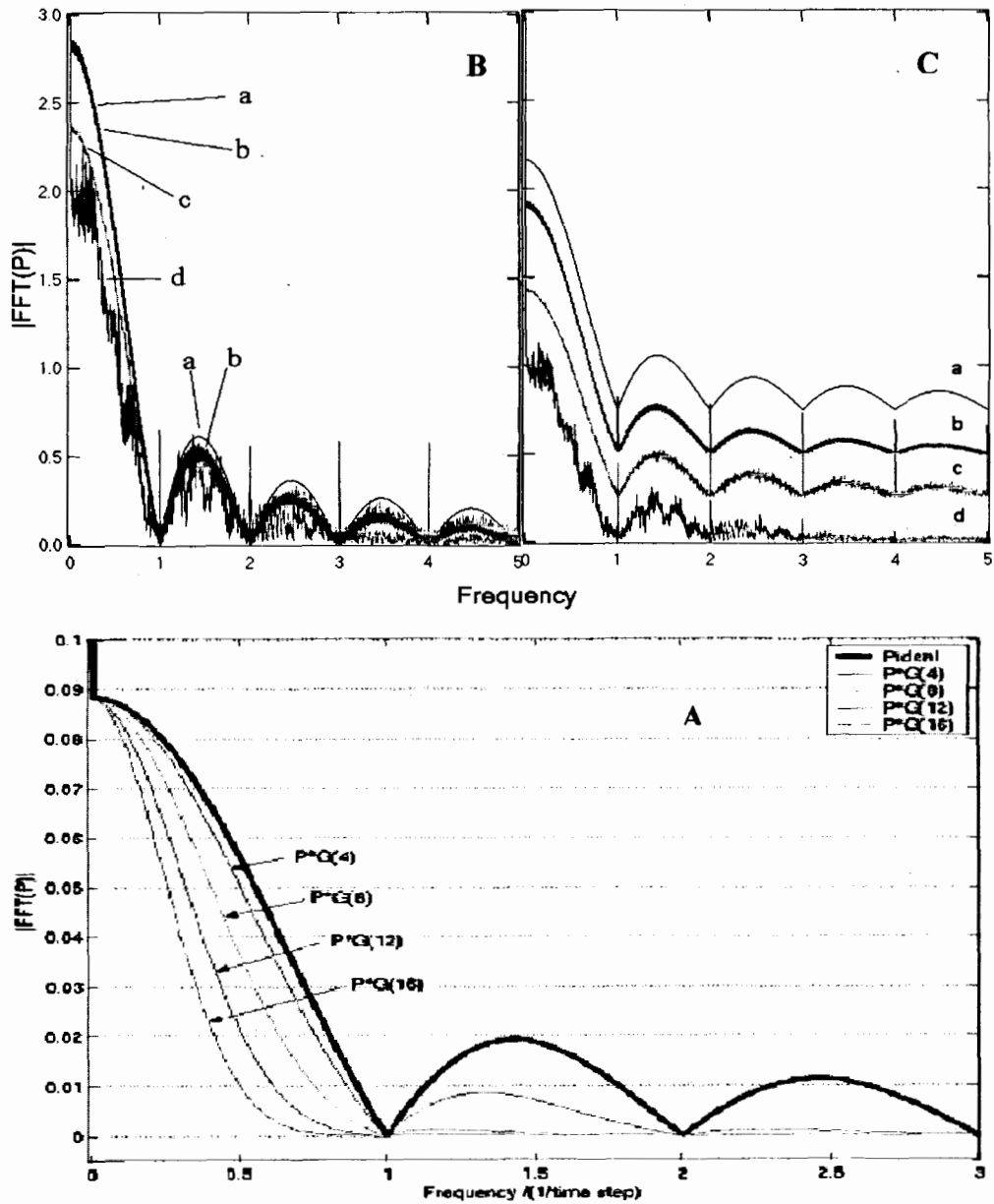


Figure 5.17. A) The Fourier transform of the chopper response from synthetic data. Each chopper response function is a convolution of the ideal PRBS sequence, P , with a Gaussian. $G(n)$ means the FWHM of the Gaussian is n which should be compared to the time step $\tau = 64$. B) Comparison of the Fourier transform a) of the ideal PRBS sequence, b) trajectory simulation data, c) convolution simulation data and d) experimental data. C) Data from B) offset for clarity.

recovered spectrum degrades. For data obtained in a counting experiment, the signal-to-noise varies with the intensity (counts) in the peak. Therefore, for a chopper response function of a specified rise time, the resolution of the most intense peaks will be better than that of the weaker peaks. For the ratio of rise time/ $\tau = 1/16$, a resolution enhancement of 11 was obtained for a peak of intensity 100,000 counts in synthetic data after 1000 iterations, whereas for a peak of intensity 10,000 counts, the resolution enhancement factor was only 10 after the same number of iterations. On this basis, we would expect an effective time resolution of 0.7 ns (*i.e.* 1/10 of the 8 ns time base) for the elastic peak, but 0.8 ns or larger for the losses that are about 5% of the elastic peak intensity. Examining the resolution of the elastic peak in the trajectory simulation data, the FWHM of the elastic peak is approximately 1 ns; however, the resolution in the losses is not as good. This can be seen from the fact that the splitting in the 857-858 ns peaks is not resolved. The effective resolution of 2 ns expected in the loss peaks is consistent with this observation. As the dimensions of the chopper are reduced from 250 μm to 5 μm (Fig. 5.11, curves f-d), the reduction in the rise time leads to a more ideal response function and greater resolution can be achieved in the loss peaks. This is most apparent in the gain and loss features in the base of the elastic peak at 840.5 and 845.5 ns. In principle, further iterations should lead to better resolved spectra; however, in both the experimental and trajectory simulation data, further iterations lead to an increase in artifacts.

There are several reasons that artifacts appear in the recovered spectra. In synthetic data[86] containing a Poisson noise distribution, finite rise times, but no background, the dynamic range (defined as the ratio of the most intense peaks to the

magnitude of the largest artifacts) was found to be between 10^3 and 10^4 , depending weakly on the total number of counts in the peaks. This appears to be a fundamental limitation of the information inherent in data obtained with PRBS modulation due to Lucy algorithm. The presence of background in the PRBS data, as well as in the object function itself, causes further degradation in the dynamic range. When there is a constant background added to the PRBS-modulated data (although still with a Poisson noise distribution), the algorithm tries to form more narrow spectral features. In our instrument, the transmission was less than 1% (for a V_{app}/KE ratio of 0.1 and θ_{acc} of 1°), which leads to a background of order 1% of the total counts in the spectrum. When a background was added to the synthetic data [86] at a level of 1% of the total counts in the PRBS spectrum, there was a modest decrease in the dynamic range, but it was still of order 10^4 . However, when the background was increased to 10%, the dynamic range degraded to about 2000. Therefore the broad spectral background of continuum losses in most HREELS spectra represent a potential problem for the Lucy algorithm[35], however, the artifacts in the experimental data appear to be larger than expected simply from the presence of the background. Indeed, in the trajectory simulation data, the presence of the background does not appear to present significant difficulties.

The primary source of artifacts appears to be the oscillations on the edges of the response function, which lead to a decrease in the height of the single open bits in the PRBS sequence. The effect of this is shown in Fig. 5.13. There is no noise and the rise time is zero, so the presence of artifacts implies that there is a fundamental loss of information. We conclude that it is critical to choose a time base that is sufficiently large compared to the rise time of the system, preferably by at least a factor of 8.

Finally, we examine the convolution assumption and the extent to which it contributes to artifacts in the spectra for the case of HREELS. As discussed in Sect. II, the response function deviates from a convolution in at least two different ways. First, the response function has an energy dependence, we have calculated the shape of the rising edge of the chopper response function for two energies, 4 eV and 3.6 eV, which correspond to the elastic peak and the largest energy loss in a typical HREELS spectrum. As shown in Fig. 5.18, the difference in the lag of the chopper response is only about 10 ps. Since the experimental (and trajectory simulation) data is histogrammed on a 250 ps time scale, we do not expect these differences to be significant. For larger relative changes in energy, this may no longer be true. Second, the data deviates from a convolution in the sense that the energy corruption histograms vary in time. For a particular energy electron, the response function consists approximately of a sum of convolutions (Eq. 5.5). These effects, if strong enough to change the shape of the rising and falling edge for different energy electrons, would lead to artifacts in the recovered spectrum. Note that Fig. 5.18 shows the shape of the edges are very similar for different energies.

5.5.3. Performance of the PRBS-TOF Instrument

We wish to distinguish the throughput advantage from the multiplex advantage (or disadvantage) of the TOF instrument, operated in either the single pulse or PRBS modes, and compare it to the conventional energy dispersive instrument. In order to compare our new instruments to the conventional HREELS, we first give some definitions for the conventional HREELS instrument. Then the corresponding properties

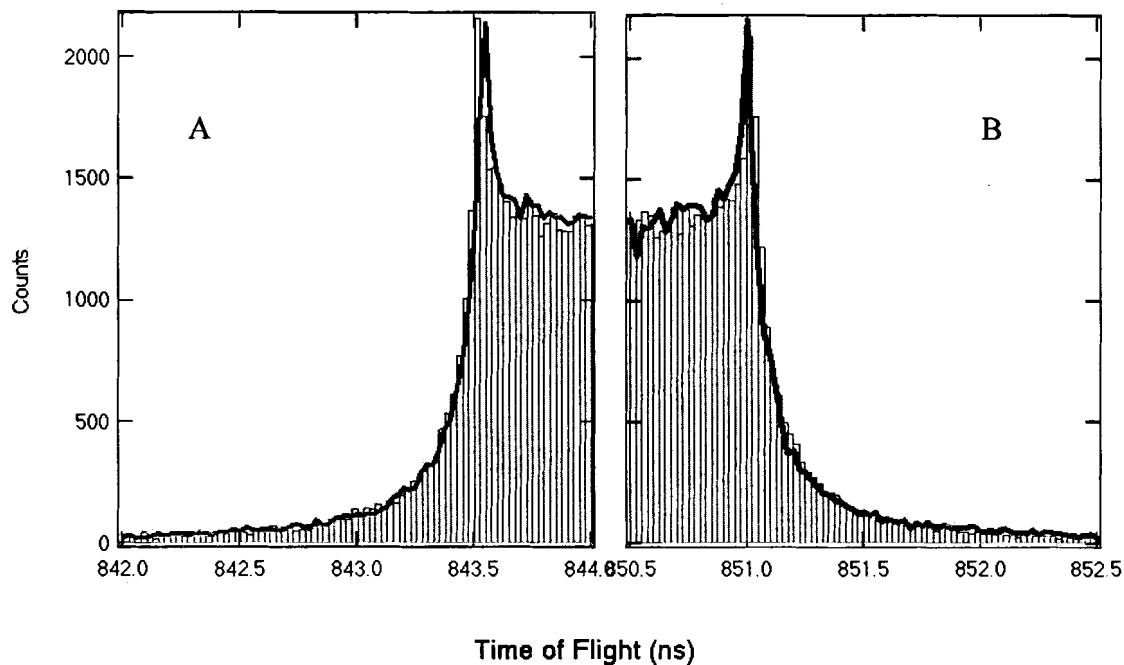


Figure 5.18. Comparison of the shape of the A) rising edge and B) falling edge of a single pulse calculated with the Monte Carlo method on a 25 ps time bin size for a kinetic energy of 4 eV (bars) and 3.6 eV (solid curves) to show that the energy dependence of the shape of the response function is negligible under the conditions of this experiment. This simulation is based on a chopper size of $d = 250 \mu\text{m}$, $V_{app} = \pm 0.4 \text{ V}$ and $\theta_{acc} = \pm 1^\circ$.

of the single pulse TOF are discussed. Next, by applying the ML method in the single pulse mode TOF instrument, the throughput advantage and signal-to-noise improvement are discussed. Finally, the advantages of the PRBS-TOF method are demonstrated.

5.5.3.1. Conventional HREELS Spectrometer

In conventional HREELS, we define

$$C_i = P(E_i)T(E) I_0 \quad (5.7)$$

as the count rate in the i^{th} energy channel. Here, $P(E_i)$ is the loss probability for electrons in the E_i energy channel for a particular sample spectrum, $T(E)$ is the transmission function of the instrument and I_0 is the primary beam density. Therefore, under the Poisson noise conditions, the signal-to-noise ratio is determined by $S/N = \sqrt{C_i}$. If the dwell time in each channel is Δt , then the total counts in one scan is

$$N_{con} = \sum_{i=1}^n C_i \Delta t. \quad (5.8)$$

If the resolution of the energy analyzer ΔE is defined as the FWHM of a Gaussian energy Transmission function, then the energy step size should be chosen $\leq \Delta E/5$. Note that the apparent energy resolution of the elastic peak in HREELS is $\sqrt{2}$ times larger than the energy resolution of the monochromator and analyzer, if they are tuned to be similar. If the energy range of interest is $E_{high} - E_{low}$ then the number of channels required are

$$n_{conv} \geq \frac{5 \cdot (E_{high} - E_{low})}{\Delta E}. \quad (5.9)$$

The time to acquire a spectrum is then

$$T_{conv} = n_{conv} \Delta t. \quad (5.10)$$

Because the energy analyzer is based on electrostatic deflection, only one channel can be measured at a time, so the duty cycle is $1/n_{conv}$. For example, suppose the maximum count rate in the elastic peak $N_{elastic} = 10^5$ cts/s for $I_0 = 10^8$ - 10^9 cts/s with $\Delta E = 1$ meV. (This would correspond to an apparent energy resolution of 1.4 meV in the straight through tuning.) The energy scan range $E_{high} - E_{low} = 0.5$ eV; the total number of channels is at least 2500. For dipole losses that are 1% of $N_{elastic}$, if the dwell time per channel is 1 second, the maximum count rate in the losses is of order 10^3 counts and a signal-to-noise ratio of 33 can be achieved. This leads to typical data collection times, on-specular, of 1 hour. For non-dipole losses (0.1% of $N_{elastic}$), collection times will be ten times longer to achieve the same signal-to-noise ratio. Typical times are 12-24 hours. Clearly, the sample and instrument stability are important.

5.5.3.2. Single Pulse TOF Instrument

For a single pulse TOF instrument, the resolution of a TOF analyzer is energy dependent. If we choose the time resolution of the TOF analyzer to be comparable to the resolution of the conventional analyzer at the energy of the elastic peak, then the resolution in the TOF spectrum will be higher in the loss region at lower kinetic energies. Suppose the time resolution is determined such that

$$\tau = L \sqrt{\frac{m}{8E^3}} \cdot \Delta E. \quad (5.11)$$

Here, L is the length of the flight path, and we assume ΔE is the FWHM of the point spread function (Gaussian energy transmission function) and take τ to be the width of an ideal square pulse. If in the conventional spectrometer $\Delta E = 1$ meV for a 4 eV beam, then τ is 21 ps for $L = 1$ m, which is only two orders of magnitude above the quantum limit.

The duty cycle is limited by the range of flight times. The minimum and maximum flight times to cover the same energy range are

$$ToF_{\max} = L \sqrt{\frac{m}{2E_{\text{low}}}} \text{ and } ToF_{\min} = L \sqrt{\frac{m}{2E_{\text{high}}}}.$$

Unless the energy distribution is limited, for example by a dispersive sector, the range of flight times may be considerably larger. Therefore, the minimum number of channels in the time domain is at least as large as

$$n_{ToF} \geq \frac{ToF_{\max} - ToF_{\min}}{\tau} = \frac{2E_{\text{elastic}}^{3/2}}{\Delta E} \cdot \left(\frac{1}{\sqrt{E_{\text{low}}}} - \frac{1}{\sqrt{E_{\text{high}}}} \right) \quad (5.12)$$

and the duty cycle is $\frac{\tau}{ToF_{\max} - ToF_{\min}}$. The count rate in the single pulse mode is related to

the total count rate in the conventional spectrum by

$$C_{ToF} = \left(\sum_{i=1}^n C_i \right) \frac{\tau}{(ToF_{\max} - ToF_{\min})} \quad (5.13)$$

for the case in which the etendue of both instruments are identical. In fact, the etendue of a conventional energy analyzer is energy dependent, whereas that of a (simple) TOF analyzer is constant with mass and energy. (In our case, the TOF acceptance angle is approximately 1/3 that of the conventional analyzer, however comparison of the DC current suggests that the etendue of the TOF is about 0.02 times that of the conventional analyzer at the present stage.) Therefore, the time to collect a spectrum with the same number of counts as was obtained with the conventional spectrometer, Eq. 5.8, is

$$T_{ToF}^S = \frac{(ToF_{\max} - ToF_{\min})}{\tau} \Delta t. \quad (5.14)$$

Now we can define the throughput advantage, $G_{th}^{s,conv}$, of a single pulse TOF instrument compared to a conventional energy analyzer as the ratio of T_{conv}/T_{TOF}^S :

$$G_{th}^{s,conv} = \frac{T_{conv}}{T_{TOF}^s} = \frac{5}{2} \cdot \frac{\sqrt{E_{low}E_{high}} \cdot (\sqrt{E_{low}} + \sqrt{E_{high}})}{E_{elastic}^{3/2}} \quad (5.15)$$

For comparison with the PTFE sample in which $E_{elastic} = 4$ eV, $E_{high} = 4.1$ eV and $E_{low} = 3.6$ eV, the throughput advantage of the single pulse TOF instrument over conventional HREELS is 4.7. Assuming the necessary time resolution can be achieved, and the etendue is equal, only 12 minutes are required to collect the same total number of counts as obtained in 1 hour with the conventional HREELS spectrometer. In single pulse mode, the signal-to-noise is still controlled by the Poisson distribution, so the S/N in the i^{th} bin is $\sqrt{N(t_i)}$, where $N(t_i)$ is the number of counts in the i^{th} time bin. However, if the time resolution improves at lower energy (relative to the width of the features) then the same number of counts are distributed amongst more time bins than there were energy bins in the conventional energy spectrum. Although this leads to a lower S/N in the time bins, conversion of the TOF histogram back into an energy distribution should give a spectrum with the same S/N in the corresponding energy bins. Therefore, the performance advantage is due simply to the reduction in time to acquire the spectrum, given by the throughput advantage (Eq. 5.15)

In our spectrometer, the current chopper response time of 1 ns limits the width of the pulse. However, we can use a pulse of large width and then recover the resolution using ML or Bayesian algorithms. The resolution enhancement is a non-linear function of the S/N (or counts) in each time bin, as well as the shape of the point spread function. Fig. 5.19 illustrates how the resolution enhancement that can be achieved depends on these

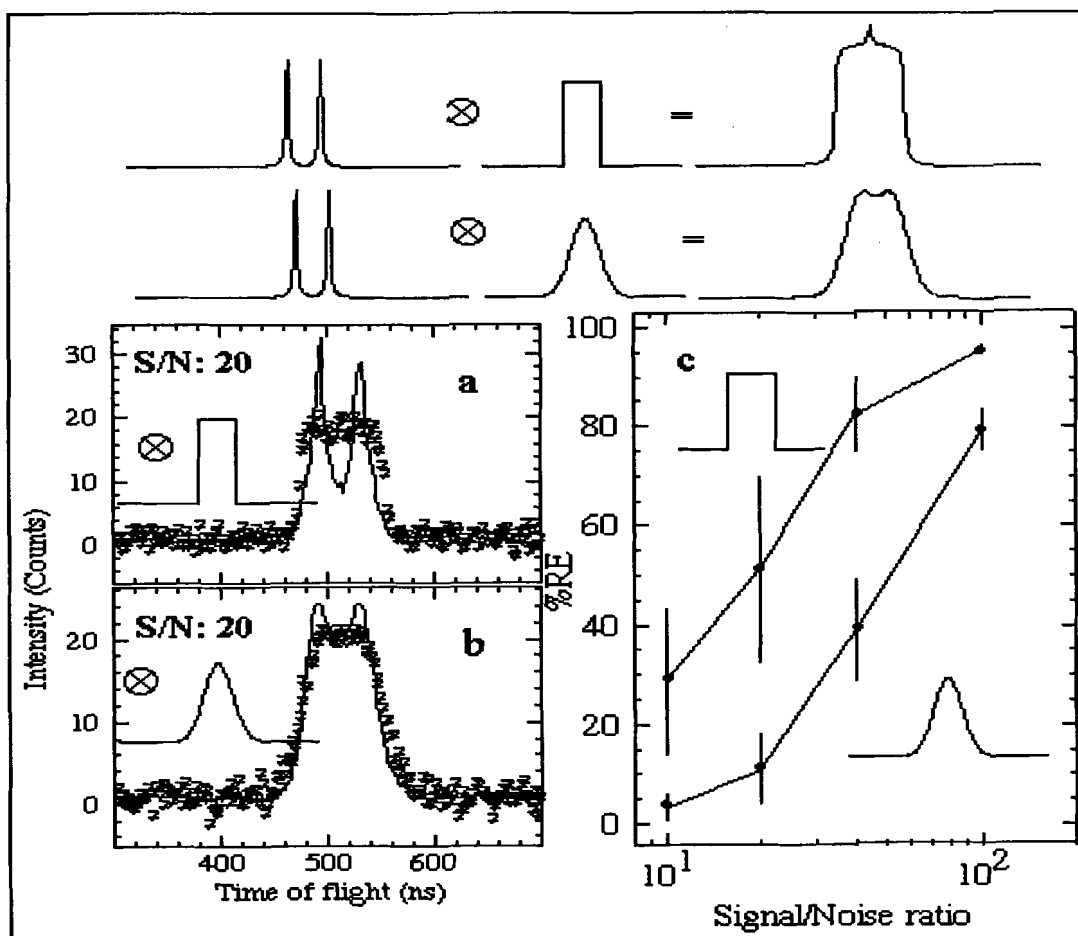


Figure 5.19. The extent to which the underlying spectrum can be recovered depends strongly upon the signal-to-noise ratio (S/N) and the shape of the instrumental response function. Noisy spectra were generated by convolution of a pair of Lorentzians with a square pulse or Gaussian, in a and b, respectively, and adding noise with a normal distribution, for a S/N of 20. c) After deconvolution with the Bayesian maximum entropy algorithm[36], the resolution enhancement was quantified as the depth of the valley is compared to the average height of the pair of Lorentzians as a function of the S/N[87]. The resolution enhancement depends on S/N, but is significantly higher when the response function is a square pulse (upper curve) rather than Gaussian (lower curve).

factors. A pair of Lorentzians, separated by the FWHM of the point spread function, were convoluted with either a Gaussian or a square pulse point spread function and then noisy data sets were generated. With the square pulse shape, the effective resolution after resolution enhancement can be more than 8 times higher than the normal pulse width.

There is an additional throughput advantage that can be achieved by utilizing these ML and Bayesian algorithms, which is illustrated in Fig. 5.20 for the case of the single pulse TOF instrument. In a single pulse experiment, the object function is broadened by a triangular response function. When the chopper is left open for 8 ns, the spectrum contains 8 times more counts than with width 1 ns. Since the duty cycle is increased, there are 10^4 counts in the center of the most intense peak ($S/N \sim 100$), which is sufficient to fully recover the underlying spectrum, as shown Fig. 5.20. The deconvoluted spectrum shows that the peaks are recovered with approximately 8x greater intensity. For a weaker peak with lower S/N , low resolution enhancement will be achieved, but the throughput advantage is still a factor of 8. This illustrates the fact that the signal-to-noise ratio in any particular peak is a function of the algorithm and other factors described previously[35].

The variation in the recovered spectra from one noisy measurement to another may be quantified in the manner defined by Larson[62]. Because the noise is correlated with the sample, it is necessary to calculate the S/N at each channel in the spectrum. Testing of the Bayesian maximum entropy algorithm has been reported previously, using synthetic data[35]. Larson *et al.*[62] define the S/N ratio as

$$S / N_{ML} = \frac{\langle N(t_i) \rangle}{\langle (E_i^{ML})^2 \rangle^{1/2}} \quad (5.16)$$

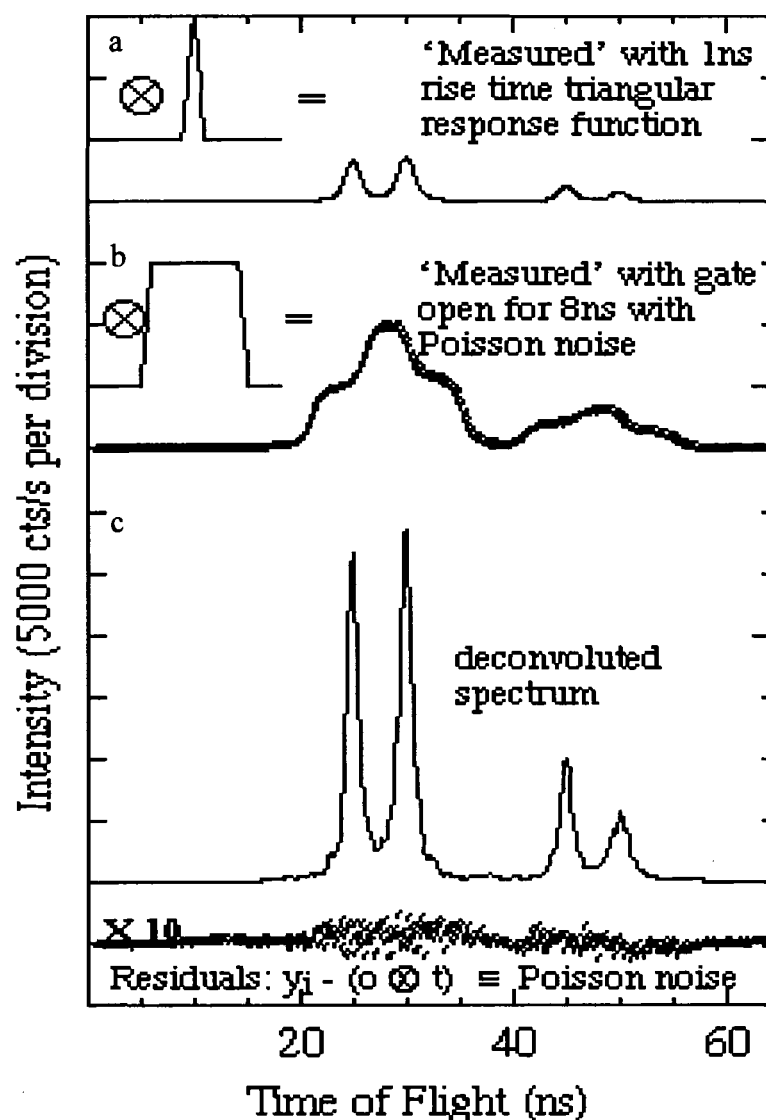


Figure 5.20. Comparison of the convolution of a pair of Lorentzians of equal height and two smaller Lorentzians of differing shape with a) a 1 ns FWHM triangular response function, and b) a 8 ns FWHM pulse (with 1 ns rise times) with Poisson noise. c) After deconvolution with the Bayesian maximum entropy algorithm, the resolution is improved by a factor of 8, yielding a throughput advantage as indicated by the 8x increase in the peaks. (The height difference in the shoulders of the noisy data (b) results in a higher intensity in the 30 ns peaks than the 25 ns peak simply due to statistical fluctuations.)

where $\langle N(t_i) \rangle$ is the average number of counts in the i^{th} channel of a noisy spectrum and the denominator is the standard deviation of the counts in the same channel.

For a single pulse TOF instrument that uses a pulse width larger than the nominal time resolution and then employs probability-based estimation methods to recover the resolution, the overall performance advantage is a product of the throughput advantage (defined in terms of the reduction in the time to collect the same number of counts in a spectrum) and the improvement in the S/N ratio in a particular channel, *e.g.* relative to the S/N in the conventional (or standard single pulse) spectrum. Because the estimation method utilizes *a priori* information regarding the process that led to the measured data, an improvement in the S/N ratio is possible[35]. In the same way that the uncertainty in a parameter in a non-linear least squares fit quantifies the accuracy of the parameters, the fluctuations in a particular channel of the recovered spectrum, due to variations in the noise of the measured spectrum, can be used to define the S/N ratio.

For a set of noisy spectrum (either synthetic or experimental), we can define the S/N ratio as the ratio of the mean value in the i^{th} channel to the standard deviation in the i^{th} channel of the recovered spectrum. Based on work reported previously [35], the mean resolution enhancement, divided by the standard deviation of the resolution enhancement suggests that a S/N ratio of 4-30 can be achieved, depending upon the number of counts in a peak, using the Bayesian maximum entropy algorithm. Note that our definition is different from the more common definition of the S/N ratio often used in instrumentation, namely the ratio of a peak height to the noise level in the baseline near the peak. The latter definition does not consider variations in the height of the peak in the same way. A thorough analysis of the dependence of the ML processing advantage for the single pulse

TOF mode is beyond the scope of the present article; however, because the transmission is linearly dependent on the duty cycle, there is little advantage or disadvantage. We will treat this issue in greater detail for the case of PRBS-modulated data, below. In general, the signal processing advantage depends on the number of iterations (for the Lucy ML method), the S/N in the data, the shape (*e.g.* the rise time) of the point spread function, and, in practice, factors such as the accuracy with which the point spread function can be determined.

5.5.3.3. PRBS-Modulated TOF Instrument

So far, we have discussed and compared the performance of the conventional HREELS spectrometer with the single pulse TOF instrument. Now we turn to the advantage of a Hadamard or PRBS-modulated TOF instrument. First we discuss the throughput and multiplex advantage of PRBS modulation using linear recovery methods. The Hadamard matrix method, using Hadamard transforms, is mathematically equivalent to the cross-correlation method which can be implemented with serial convolutions, or more efficiently with prime factor transforms[82]. To define the throughput advantage of the PRBS spectrometer relative to a single pulse TOF spectrometer and to the conventional spectrometer, both operated with the same resolution, we again define the width of the time step as in Eq. 5.11 and calculate the time to acquire a spectrum with the same total number of counts as in a conventional spectrum. The recovered spectrum will be sampled on the same time increment, τ , as in the single pulse TOF spectrum.

The length of the sequence should be chosen such that the period of the PRBS sequence is larger than the difference between TOF_{max} and the TOF_{min} . Equivalently, the length of the sequence, $2^n - 1$, should be greater than the minimum number of channels in

the single pulse experiment, n_{TOF} , as given by Eq. 5.12. Increasing the length of the sequence increases the computational overhead, so the minimum PRBS sequence length would be typically chosen. Fernandez *et al.*[88] have shown experimentally that, for a given number of PRBS cycles, the S/N increases by a factor of $\sqrt{2}$ when the PRBS sequence length is doubled; however, the data acquisition time for the same number of cycles also doubles. Therefore, there is no advantage in the S/N to increase the sequence length. Furthermore, the sequence length has no significant effect on the average count rate. The duty cycle of the PRBS sequence, generated by a shift register of length n , is

$$\frac{2^{n-1}}{2^n - 1} \approx 0.5. \text{ Therefore, the count rate is related to the conventional spectrum by}$$

$$C_{TOF} = \left(\frac{2^{n-1}}{2^n - 1} \right) \left(\sum_{i=1}^{n_{conv}} C_i \right). \quad (5.17)$$

The time to collect a spectrum with the same number of counts as in the conventional spectrum is

$$\left(\frac{2^n - 1}{2^{n-1}} \right) \Delta t \cong 2 \Delta t. \quad (5.18)$$

Therefore, the throughput advantage relative to the single pulse TOF instrument is approximately

$$G_{th}^{PRBS, Single} = \frac{0.5(ToF_{max} - ToF_{min})}{\tau}. \quad (5.19)$$

The throughput advantage in PRBS mode as compared to the conventional HREELS spectrometer is

$$G_{th}^{PRBS, Conv} = \frac{5}{2\Delta E} (E_{high} - E_{low}). \quad (5.20)$$

In a typical HREELS spectrum, the region of interest is approximately 500 meV wide, so with $\Delta E = 1$ meV, the throughput advantage is 1250. By contrast to the simulation of the single pulse mode, if the energy range of the spectrum exceeds the region of interest the length of the PRBS sequence should be increased, but the throughput advantage is not affected because the duty cycle is still approximately 0.5.

Whereas the throughput advantage is defined based upon the time to collect a given total number of counts, the multiplex (Fellgett) advantage is usually defined in terms of the improvement in signal-to-noise due to simultaneous measurement of multiple signals with a single detector. There are two cases. If the noise is large and independent of the signal, as is the case in infrared spectroscopy[15, 62], the Fellgett advantage is given by $\sqrt{n_{TOF}/2}$. However, when the detector noise is shot limited (or Poisson), Larson *et al.*[62] has shown that the multiplex (*i.e.* Fellgett) advantage varies across the spectrum, and is given by

$$F_i = \sqrt{\frac{N(t_i)}{2\bar{N}}}, \text{ where } \bar{N} = \frac{1}{n_{PRBS}} \sum_{i=1}^{n_{PRBS}} N(t_i). \quad (5.21)$$

Fernandez *et al.*[88] have shown that under their conditions, the advantage is limited by the predictions of Wilhelmi and Gompf [63] and Larson *et al.* [62]. In practice, this means that the strong peaks will be measured with better S/N while the weaker peaks will be measured with worse S/N. In general, there is a multiplex advantage only for sparse spectra with a few strong peaks. In cross-correlate PRBS TOF-HREELS, there will be a large multiplex advantage for the elastic peak, while the loss peaks that contain the “interesting information” will be measured with a multiplex disadvantage, typically of order 0.1! Therefore, the product of the throughput and multiplex advantages is of order

25 compared to the single pulse experiment; approximately 125, compared to the conventional spectrometer.

A further disadvantage of the cross-correlate PRBS approach is that non-ideal characteristics of the chopper lead to artifacts in the recovered spectrum[63, 64, 88] as discussed in Section III. The presence of Poisson noise, which leads to fluctuations in the baseline, was included in the estimate of the S/N by Larson *et al.* [62]. As discussed by Fernandez *et al.*[88] and Brock [42], the S/N (defined in the alternate way noted above) is controlled by counting noise (Eq. 5.16) at low counts, but after data has been accumulated for larger times, the non-ideal characteristics of the chopper limit the S/N and further acquisition time does not lead to improvements in the S/N. These artifacts may, to some extent, be removed[89].

Application of the Lucy ML algorithm to the PRBS-modulated data provides two distinct advantages over the Hadamard or cross-correlation method. First, by explicitly including the Poisson noise distribution in the model of the process that generated the data, the algorithm is able to overcome the multiplex disadvantage. Bialkowski[79] previously described the advantage of ML methods to overcome the multiplex disadvantage. Second, as was discussed in regard to the limitation of the chopper rise time in single pulse TOF mode, a substantial resolution enhancement can be achieved. We were the first to show[82] that the Lucy algorithm can be applied to PRBS-modulated data, account for the Poisson noise and artifacts in the chopper response function, and achieve resolution enhancement. Here we quantify the multiplex, or signal processing advantage. While these two advantages are distinct, calculation of the multiplex

advantage is straightforward only when the resolution of the recovered spectrum is similar to the single pulse (or conventional) reference spectrum.

In our instrument, the PRBS sequence was applied to the chopper with a time step of 8 ns, which was approximately 16 times longer than the effective chopper response time of 0.5 ns. As was discussed for the case of the single pulse TOF experiment, the resolution enhancement is a non-linear function of the S/N (or counts) in the i^{th} time bin, as well as the shape of the point spread function. For the PRBS-modulated data, the rise time is critical. The resolution enhancement that can be achieved depends on the ratio of the rise time to the period, τ . By contrast to the single pulse mode, there is no additional throughput advantage by increasing the base time period, τ , since the duty cycle is fixed at 50%. When rise time/ τ is 1/16, we have shown [86] that, with the Lucy algorithm and peaks of intensity spanning approximately three orders of magnitude, the underlying spectrum can be fully recovered after 1000 – 10,000 iterations. Again, the variation in the recovered spectra from one noisy measurement to another should be quantified in the manner defined by Larson *et al.*[62]. Because the noise is correlated with the sample, the S/N and therefore the multiplex advantage, F_i , is different for each channel in the spectrum. Calculation of F_i depends upon the characteristics of the algorithm, and thus can only be done numerically. We calculate the S/N ratio, based upon Eq. 5.16, by first generating a set of 8 noisy PRBS-modulated data, all with 2×10^6 total counts, using the trajectory simulation. After recovering each data set with the Lucy algorithm using 1000 iterations, we calculated the mean and standard deviation in each channel, as shown in Fig. 5.21 a) and b), respectively. The SNR_{ML} , obtained in the ML method, is shown in curve c) as the ratio of curve a) to b). The multiplex advantage, using the Lucy method

compared to a single pulse experiment, was calculated as the ratio of the SNR_{ML} to the S/N in the single pulse peaks, which is simply the square root of the number of counts in each channel due to the Poisson noise. For comparison, in Fig. 5.22, we plot the multiplex advantage that is predicted from Eq. 5.21 for the Hadamard transform recovery of this spectrum. Thus, in this example, the Lucy algorithm provides an advantage, particularly in the weak loss region of interest. A more general analysis of this will be given elsewhere[86].

In summary, the performance advantage of the PRBS (or Hadamard) approach, when combined with the ML recovery method is the product of the throughput and multiplex advantages. In practice, the throughput advantage in HREELS will be of order 1000, while the multiplex advantage depends upon the total data collection time, the number of iterations, the rise time of the chopper relative to the PRBS time step, τ , and the relative intensity of a peak in the object spectrum. However, for the weaker peaks a substantial improvement in the multiplex advantage is obtained, which is a significant advantage over cross-correlate PRBS method. Note that because the overall performance advantage increases with data collection time, the data collection time necessary to achieve a particular S/N ratio is not easily predicted.

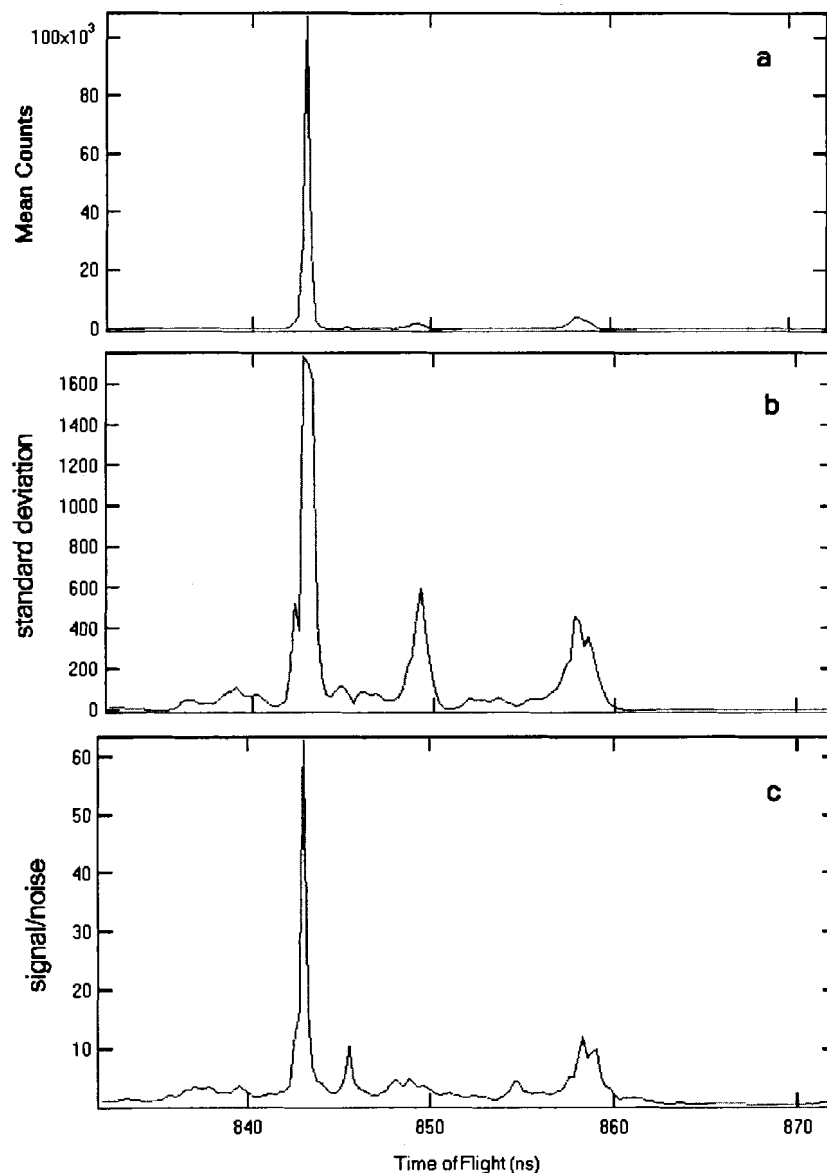


Figure 5.21. Illustration of the numerical method used to assess the signal-to-noise ratio in the synthetic data recovered with the Lucy algorithm. A set of 8 noisy PRBS-modulated data (using the conventional PTFE spectrum as object function) , all with 2×10^6 total counts, were generated by using trajectory simulation. a) The mean value of the recovered spectra in each channel; b) The standard deviation in each channel; c) The ratio of a) to b) showing how the S/N varies across the TOF spectrum.

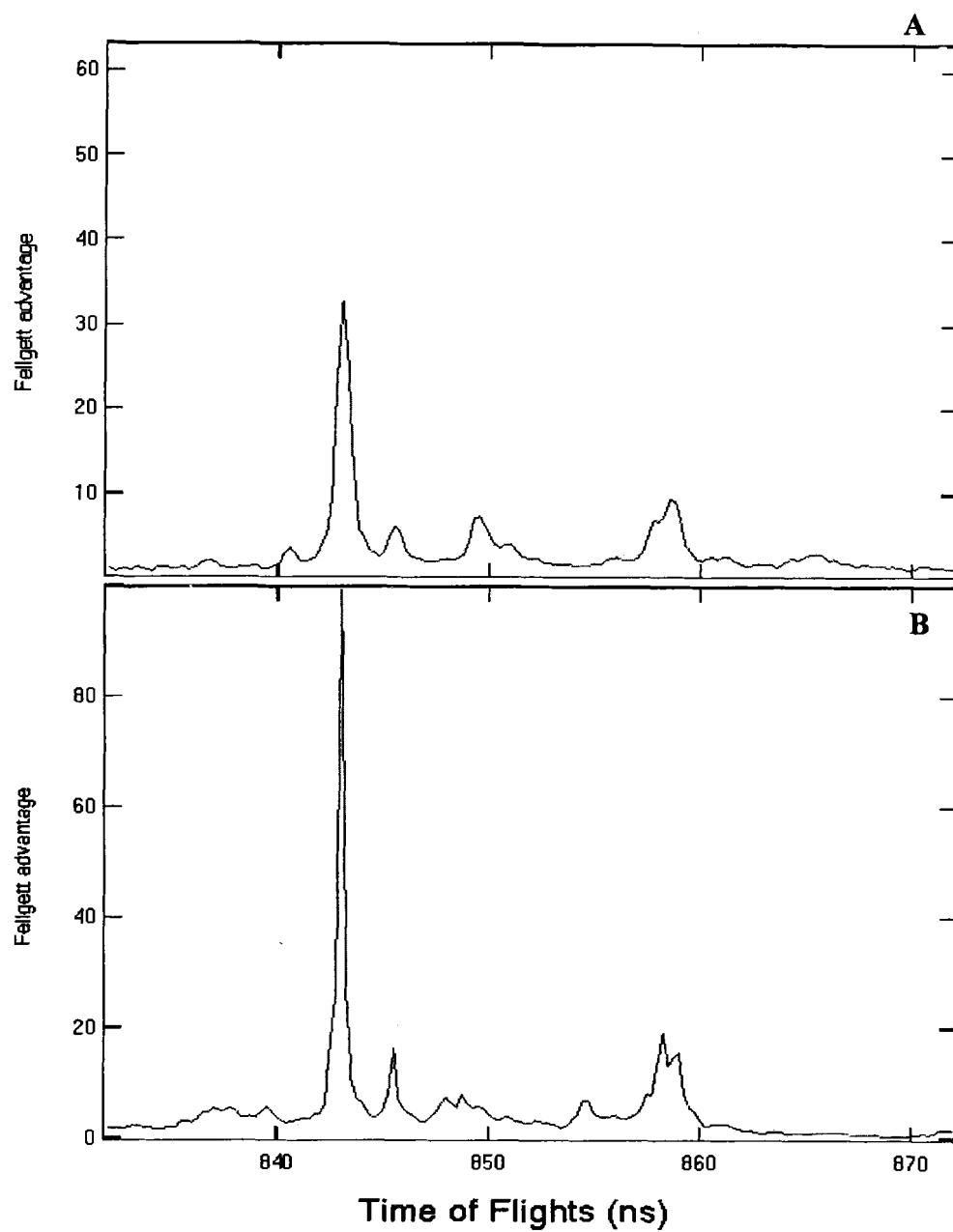


Figure 5.22. A) The multiplex advantage predicted from the Eq. 21 for the Hadamard transform recovery of the PTFE spectrum. B) The multiplex advantage is calculated by taking the ratio of the S/N using Lucy and PRBS modulation to the S/N in a single pulse mode experiment.

Chapter 6

SUMMARY AND FUTURE WORK

6.1 Summary of Results

In this thesis, we started by using a conformal map to solve the potential of an infinite array of alternately positive and negatively charged wires of finite diameter and infinite length. We simulated the trajectory of electrons on this potential to study the characteristics of the interleaved comb chopper. Experimental measurements of the static and dynamic properties were made, which were in good agreement with the theoretical model. We showed that the finite penetration of the field beyond the plane of the chopper leads to non-ideal chopper response, which we characterized in terms of an energy corruption effect and a lead or lag in the time at which the beam responds to the chopper potential.

Next we have shown the feasibility of deconvoluting the PRBS spectrum by using the maximum likelihood method. By simulating the effects of the Poisson noise distribution and non-ideal behavior of the "interleaved comb" chopper on PRBS modulated TOF-HREELS data, we have shown that resolution enhancement can be achieved, while properly accounting for the Poisson noise distribution and artifacts introduced by the chopper [76]. The simulation results suggested that a TOF-HREELS instrument with a comparable resolution and dramatic performance (throughput) advantage over conventional, serial detection analyzers, could be achieved.

On the basis of the chopper properties and the performance of the maximum likelihood deconvolution software, we constructed the first time-of-flight HREELS spectrometer. The spectrometer was tested with a highly oriented PTFE (Teflon) thin

film sample, which was characterized by AFM and Auger, as reported in a separate publication [90]. The data collected with the TOF-HREELS analyzer demonstrated that spectra could be acquired 85 times faster than with the conventional analyzer. However, the resolution of the TOF spectrum was not as high as was obtained in conventional HREELS instrument. Furthermore, the magnitude of artifacts in the recovered spectrum was significant compared to the loss features.

We then presented a general formalism to describe the energy and time-dependent contributions to the chopper response function. Further simulation work was done to analyze the factors that have the most significant effect on the resolution and artifacts. The resolution obtained in the recovered spectrum depends on the signal to noise ratio, the ratio of the rise time to PRBS time base, and the number of iterations in the recovery algorithm. We concluded that the main contributions to the time resolution are the energy corruption effects, the finite rise time of the driver electronics, and the jitter in the TDC. The simulations indicated that reduction of the scale of the chopper should improve the time resolution. From the trajectory simulation data, we determined the relationship between the chopper wire d -spacing and both the lag time and the rise time. These factors limit the duration of the PRBS time base, and therefore, the time resolution that can be achieved.

Several factors were analyzed regarding the artifacts in the spectrum. A major improvement in the recovered spectrum was achieved when better methods of smoothing the response function were devised. Another important factor is the observation that when the transmission of a single open bit is reduced, there is a fundamental loss of information that the Lucy algorithm cannot overcome. While the experimental origin of

the oscillations at the beginning and end of the pulse are not understood, their effect on the recovery algorithm is clearly detrimental. By contrast, the artifacts that would normally be generated by the reduction in the duty cycle due to the lead/lag of the chopper are compensated well by the Lucy algorithm. A careful analysis of the energy dependence of the chopper response function suggests that the deviation from the assumption of the convolution has a negligible effect on the recovery process; i.e. the assumption is valid within the energy range in our HREELS experiment.

We then defined the throughput and multiplex advantages of the instrument and compared the performance of the TOF-HREELS analyzer with the conventional analyzer. For the PTFE spectrum, the throughput advantage was a factor of 85, while the multiplex advantage is frequency dependent due to the Poisson character of the noise, but exceeded the theoretical limit for the Hadamard transform recovery method by a factor of 2. The combination of the throughput and multiplex advantages resulted in an overall performance advantage of approximately 1000 compared to the conventional HREELS instrument.

6.2 Future Improvements to Instrument

6.2.1 Resolution

In order to improve the time resolution, there are a number of directions that should be considered. Since we showed that the rise time decreases non-linearly as the chopper d -spacing is decreased, reduction of the chopper scale, while maintaining the same transmission ratio is perhaps the most important improvement. Micromachining methods may allow significant reductions in wire spacing and diameter. Because the

flight time is strongly dependent on the kinetic energy, a retarding lens before the chopper would also be a benefit to the resolution of the spectrum. Because the recovery algorithms are very sensitive to the rise time and background, an important task is to understand the origin of the oscillations at the edges of the pulse. Solving this problem not only can improve the resolution but also should decrease the artifacts. The other significant contribution to the time resolution comes from the drive electronics and the jitter in the current TDC card. Improved driver output circuits and better quality phase lock loops should be able to reduce the contributions from these sources to less than 100 ps. Finally, reducing the scattering of electrons from the flight tube wall should clean up the signal. This will require either reduction of the collimation slit height or modification of the Einzel lens after the chopper.

6.2.2 Reduction of Artifacts

Since in simulations with synthetic data we showed that the maximum likelihood algorithm will generate artifacts when the response function decreases by as little as 20% in the single open bits, it is critical that the time step be at least eight times larger than the rise time. Understanding the origin of the oscillations and reduction of scattering within the flight tube, as discussed above, will improve the response function from an experimental point of view. The autocorrelation of the chopper response function provides a convenient way to quantify the non-ideal characteristics of the chopper response function.

There are more fundamental questions regarding the information that can be obtained from the noisy, PRBS modulated data. In the absence of noise, the Lucy

algorithm converges to the correct solution with an error that is limited mostly by the numerical precision of the computer, which is of order 10^{-6} . However, when there is noise present, the resolution enhancement improves as a function of the number of iterations. However, tests with noisy synthetic data show that oscillations in the baseline are present at a level of 10^{-3} to 10^{-4} , at least for as many as 10,000 iterations. An analysis of the of the likelihood of the true spectrum and that of the estimated spectra during iteration is needed to determine whether the oscillations arise simply due to the fluctuations in the noise or whether the convergence of the algorithm can be improved.

Comparison of previous work with Bayesian maximum entropy algorithms with results of the Lucy algorithm has shown that the artifacts can be reduced significantly by incorporation of a maximum entropy constraint in the probability function. Dr. Lin DeNoyer, of Spectrum Square Assoc., is currently working on adapting the Bayesian iterative algorithms for the cyclic, PRBS modulated data.

6.2.3 Improvement to Simulation Methods

More realistic simulations are possible. The finite rise time of the chopper voltages could be included, instead of the instantaneously rise time implemented in the simulations described in this thesis. The angular distribution of the electron beam can also be included in the trajectory simulations, which would make the simulated results more realistic. In addition, the effect of scattering from the chopper wires could be included.

6.2.4 Lens Design

In order to achieve a higher throughput advantage and better match the angular distribution under different scattering conditions, it would be desirable to be able to adjust the acceptance angle from the high angular resolution of the current instrument to values of 2-4° for dipole scattering on well ordered surfaces, and even larger values of order $\pm 10^\circ$ on rougher surfaces. A lens in front of the chopper could increase the etendue compared to the conventional HREELS, without affecting the time resolution as long as the angular distribution at the chopper can be kept small. The large relative change in energy, from the elastic peak down through the loss region, presents significant design challenges due to chromatic aberrations in electron optics.

6.3 Applications to Demonstrate Performance Advantages

In this project, we only examined the PTFE spectrum, in which dipole scattering was dominant. As we discussed in Chapter V, the multiplex advantage depends on the nature of the spectrum. To demonstrate the advantages of the Lucy algorithm over the standard cross-correlation recovery, a sample that has a higher density of closely spaced peaks with intensity, relative to the elastic peak that is significantly smaller than in the case of the PTFE spectrum, should provide a more dramatic test. We need to simulate the data to show the multiplex advantage of the Lucy recovery method, compared to the multiplex disadvantage of the standard method.

The advantages of the greater throughput could be amply demonstrated by a study of the negative ion resonances of a complex molecule, such as benzoate on Cu(110). A previous study by Chen, et al.[26, 91], reported data only for the CH stretch region, due

to the prohibitively long data acquisition times required to measure complete loss spectra for a range of incident beam energies and incident angles. A complete data set, that would take months to acquire with the conventional HREELS instrument could be reduced to an afternoon's work. For this to be done efficiently, it would be necessary to improve the tuning of the monochromator, so that the monochromatic beam stays properly tuned when the primary beam energy is scanned.

Other experiments could exploit the fast data acquisition time. For example, if data acquisition times can be reduced to a few seconds, then potentially the PRBS TOF-HREELS instrument could measure useful spectra on insulating materials. On surfaces where charging occurs, the primary beam could be gated on or off for periods of tens or hundreds of milliseconds to allow the surface to discharge before being exposed to a further electron beam exposure. This also offers, at a more fundamental level, an opportunity to study the charging mechanism itself. With fast acquisition times, we could take spectra step by step until the sample is fully charged. By characterizing the morphology of the sample, for example with AFM, the time dependence of the charging process could be quantified by modeling the electron transport properties, for example in thin insulating polymer materials.

Based on the work we have done and the prospects for further improvements to the instrument, we are optimistic that this new approach of TOF-HREELS can achieve resolution comparable to state-of-the-art conventional HREELS instruments, but with a dramatic throughput advantage. To the extent that the properties of the TOF analyzer allow investigation of more realistic surfaces, we expect that the instrument will make a significant impact on the development of HREELS within the surface science field.

APPENDIX

Preparation of Highly Oriented PTFE Samples

1. The Deposition of the PTFE films

In our experiment, the PTFE rod used was Teflon[®] from Good fellow, 99.99% purity, 0.5 inch diameter. The melting temperature of the PTFE rod is specified as 327 °C. PTFE films were deposited onto a 10 x 10 mm^2 substrate cut from a silicon wafer having a 3000 Å thick platinum or gold film on it. The rms roughness of the metallized substrate surface was measured by AFM to be less than 12 Å within an area of the order of several square microns.

The deposition of the PTFE films was accomplished by a custom-built device. The PTFE rod was fixed at one end of an aluminum rod; the other end of the aluminum rod was extended out of the oven so that weights could be put on the rod, as illustrated in Fig A.1. The substrate was put between two glass strips so that the PTFE rod could be preconditioned on these glass strips. All of the glass strips and the sample were put on an aluminum cart which slid on an aluminum groove. The cart was connected to a motor by a 1/4 - 40 stainless steel rod and the motor was fixed to the oven in order to reduce vibrational effects of the motor rotation. The end of the PTFE was beveled to 1 x 8 mm^2 . We cut the width of the PTFE rod 2mm less than from the width of the sample so that the surface profiler can be used to measure the thickness of the deposited PTFE films. Each time before the PTFE films were deposited onto the sample, the rod was preconditioned by rubbing the glass 3-4 cm for 20 or 30 minutes just in one sliding direction. Before the PTFE was deposited onto the sample, it was slid 2 to 3 cm on the glass then directly onto the sample. The rotation speed of the motor was selectable to achieve two sliding speeds,

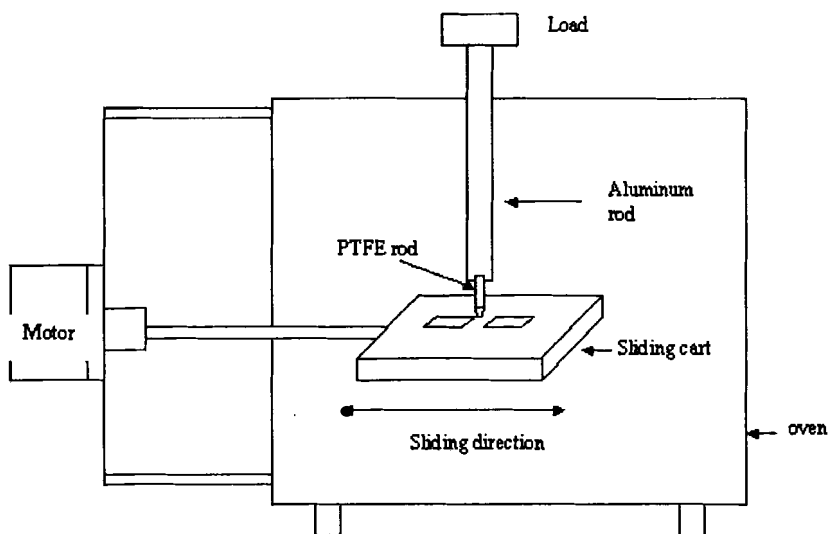


Figure A.1 A schematic drawing of the PTFE film deposition instrument. The substrate was clamped in a groove on the cart between two glass strips. The PTFE rod was attached to one end of the aluminum rod; the other end of the aluminum rod extended out of the oven so that the load on the PTFE rod could be adjusted by adding weight. The aluminum cart was connected to a motor by a $\frac{1}{4}$ - 40 stainless steel threaded rod which slid back and forth. The motor was mounted on the outside of the oven through supports on the back. A thermocouple was connected to the cart so the temperature of the instrument could be monitored.

1 mm/sec and 2 mm/sec. A K-type thermocouple wire was attached to the cart so that the temperature of the system could be monitored.

2. Microscopy Methods

After the PTFE sample was prepared, it was first put under the microscope (Digital camera Microscope, Zeiss, Germany) to observe the optical properties of the PTFE films. Figure A.2 shows the comparison between the optical image of the bare platinum substrate and the image of the PTFE films on the substrate when breathing on these samples. A clear orientation along the friction direction can be observed on the PTFE sample. In order to find the detailed structure of these PTFE films on the substrate, we used the AFM to characterize it.

The AFM (Autoprobe CP AFM, Park Scientific Instruments, Sunnyvale, CA) was operated in air condition. In our measurement, we only used the contact mode, the biggest scanning area was $10 \times 10 \mu\text{m}^2$, the smallest scanning area was $10 \times 10 \text{ \AA}^2$.

3. The Results from AFM

Fig. A.3 shows a sample of the images of the PTFE films measured by AFM. The image shown in Fig. A.3a is the bare platinum substrate; A.3b, A.3c, and A.3d are the images of PTFE films under 220 grams, 480 grams and 1 kg, respectively. From these images, we can see that the basic units of the deposited PTFE films are very long ribbons. The direction of these ribbons is along the sliding direction. As the load increased the ribbons were oriented more parallel to each other and the coverage on the platinum substrate increased. The detailed height profile is shown in Figure A.4. By subtracting the

base slope, the detailed analysis showed that the average height of the PTFE ribbons was around 300 Å.

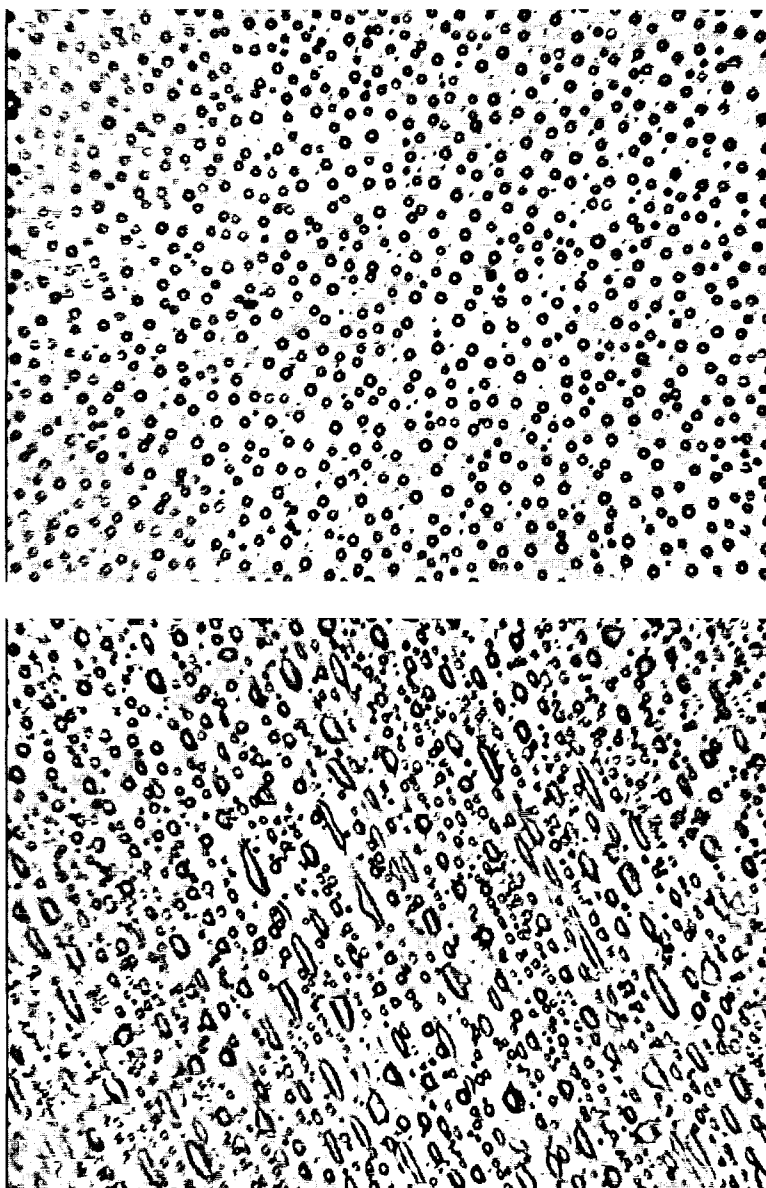


Figure A.2 A photo taken under the microscope. The upper image shows the view when breathing on the bare sample and the lower image is the case when breathing on the PTFE sample.

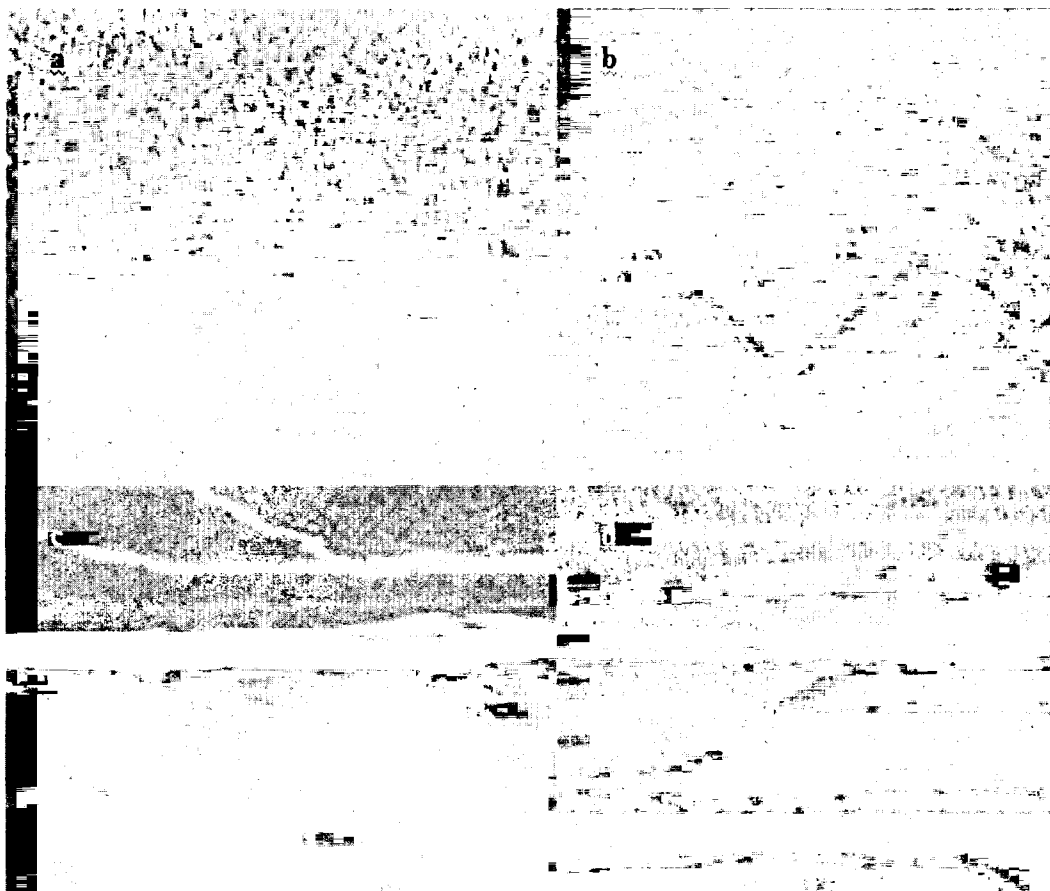


Figure A.3 Some AFM images for the PTFE film on Pt substrate. 3a is the image of bare Pt. 3b,c,d are the AFM images of PTFE films with pressure of 27.5 g/mm², 60 g/mm², and 125 g/mm² respectively. The image reveal the PTFE films forms long and parallel ribbon on the Pt substrate. The scanning area is 10 μm x 10 μm.

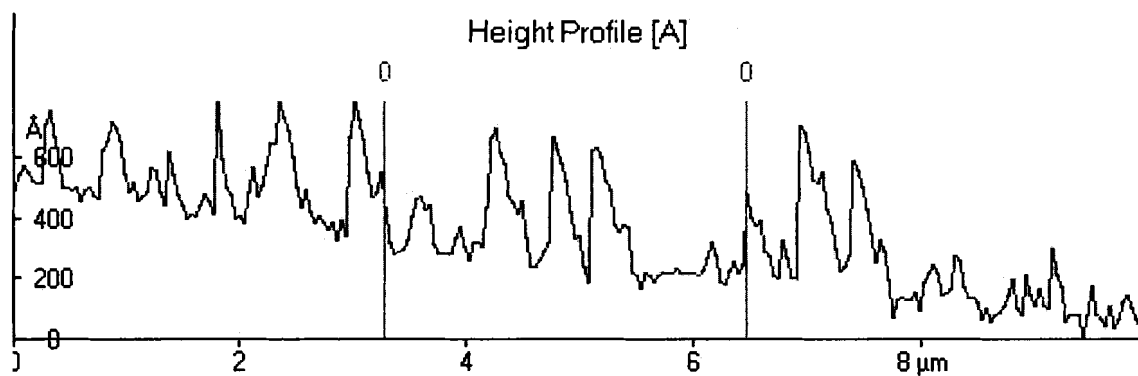


Figure A.4 A height profile for the PTFE films on platinum substrate was obtained by scanning along a line perpendicular to the PTFE ribbons. If subtract the base, the average height for the ribbons is about 300 Å.

REFERENCES

1. Ibach, H. and D.L. Mills, *Electron Energy Loss Spectroscopy and Surface Vibrations*. 1982, New York: Academic.
2. Rowe, J.E. and H. Ibach, *Photoemission and energy loss spectroscopy on semiconductor surfaces*. Surf. Sci., 1975. **48**: p. 44-58.
3. Ibach, H. and J.E. Rowe, *Electronic transitions of oxygen adsorbed on clean silicon (111) and (100) surfaces*. Phys. Rev. B, 1974. **9**(4): p. 1951-1957.
4. Hoffman, P., S.R. Bare, N.V. Richardson, and D.A. King, *Orientation of chemisorbed species from electron impact and dipole selection rules: the formate ion on Pt(110)*. Surf. Sci., 1983. **133**: p. L459-L464.
5. Netzer, F.P. and M.G. Ramsey, *Structure and orientation of organic molecules on metal surfaces*. Crit. Rev. Sol. St. Mat. Sci., 1992. **17**(5): p. 397-475.
6. Frederick, B.G., M.R. Ashton, N.V. Richardson, and T.S. Jones, *Orientation and bonding of benzoic acid, phthalic anhydride and pyromellitic dianhydride on Cu(110)*. Surf. Sci., 1993. **292**: p. 33-46.
7. Cole, R.J., B.G. Frederick, J.R. Power, C.C. Perry, Q. Chen, C. Verdozzi, N.V. Richardson, and P. Weightman, *Orientation of molecular adsorbates from reflection anisotropy spectroscopy*. Physica Status Solidi, 1998. **A 170**(2): p. 235-239.
8. Frederick, B.G., J.R. Power, R.J. Cole, C.C. Perry, Q. Chen, S. Haq, T. Bertrams, N.V. Richardson, and P. Weightman, *Adsorbate azimuthal orientation from reflectance anisotropy spectroscopy*. Phys. Rev. Lett., 1998. **80**(20): p. 4490-4493.
9. Perry, C.C., B.G. Frederick, J.R. Power, R.J. Cole, S. Haq, Q. Chen, N.V. Richardson, and P. Weightman, *Complementary Vibrational and Reflectance Anisotropy Spectroscopy Determination of Molecular Azimuthal Orientation*. Surf. Sci., 1999. **427-428**: p. 446-451.
10. Gadzuk, J.W., *Inelastic resonance scattering, tunneling, and desorption*. Phys. Rev. B, 1991. **44**(24): p. 13466-13477.
11. Palmer, R.E. and P.J. Rous, *Resonances in electron scattering by molecules on surfaces*. Rev. Mod. Phys., 1992. **64**(2): p. 383-440.
12. Ibach, H., *Electron Energy Loss Spectrometers: The Technology of High Performance*. Springer Series in Optical Sciences. Vol. 63. 1991, Berlin: Springer-Verlag.
13. Ibach, H., *Electron Energy Loss Spectroscopy with Resolution below 1 meV*. J. Electron Spectrosc. Relat. Phenom., 1993. **64/65**: p. 819-823.
14. Chabal, Y.J., *Surface infrared spectroscopy*. Surf. Sci. Rep., 1988. **8**(5-7): p. 211-353.
15. Frederick, B.G., T.S. Jones, P.D.A. Pudney, and N.V. Richardson, *HREELS and RAIRS? A complete vibrational study of the surface benzoate species adsorbed on copper*. J. Electron Spectrosc. Relat. Phenom., 1993. **64/65**: p. 115.
16. Lucas, A.A. and M. Sunjic, *Fast-electron spectroscopy of collective excitations in solids*. Prog. Surf. Sci., 1972. **2**: p. 75.
17. Lucas, A.A., J.P. Vigneron, P. Lambin, P.A. Thiry, M. Liehr, J.J. Pireaux, and R. Caudano, *Electron Energy Loss Spectroscopy of Surface and Interface Phonons*

- of Insulators, Semiconductors, and Superlattices. Int. J. Quant. Chem, 1986. S19: p. 687-705.
18. Evans, E. and D.L. Mills, *Theory of Inelastic Scattering of Slow Electrons by Long-Wavelength Surface of Optical Phonos: Multiphonon Processes*. Phys. Rev. B, 1973. 7: p. 853.
 19. Aers, G.C., T.B. Grimley, J.B. Pendry, and K.L. Sebastian, *Electron energy loss spectroscopy. Calculation of the impact scattering from W(100)p(1x1)H*. J. Phys. C: Solid State Phys., 1981. 14: p. 3995-4007.
 20. Ho, W. and R.F. Willis, *Observation of Nondipole Electron Impact Vibrational Excitations: H on W(100)*. Phys. Rev. Let., 1978. 40: p. 1463-1465.
 21. Teillet-Billy, D., D.T. Stibbe, J. Tennyson, and J.P. Gauyacq, *Vibrational excitation in low-energy electron scattering by H₂ molecules physisorbed on a metal surface*. Surf. Sci., 1999. 443: p. 57-68.
 22. Djamo, V., D. Teillet-Billy, and J.P. Gauyacq, *Low-energy electron scattering by N₂ molecules physisorbed on Ag: Study of the resonant vibrational excitation process*. Phys. Rev. B, 1995. 51: p. 5418-5428.
 23. Schulz, G.J., *Resonances in Electron Impact on Atoms*. Rev. Mod. Phys., 1973. 45: p. 378-422.
 24. Schulz, G.J., *Resonances in Electron Impact on Diatomic Molecules*. Rev. Mod. Phys., 1973. 45: p. 423-486.
 25. Frederick, B.G., A. Munz, T. Bertrams, Q. Chen, C.C. Perry, and N.V. Richardson, *Negative Ion Mediated Molecular Manipulation with STM of c(8x2) benzoate/Cu(110)*. Chem. Phys. Lett., 1997. 272: p. 438-444.
 26. Chen, Q., B.G. Frederick, C.C. Perry, A.W. Munz, T. Bertrams, and N.V. Richardson. *Negative ion mediated electron stimulated disordering of c(8x2) benzoate/Cu(110): Extension of the displaced harmonic oscillator model*. in DIET-7. 1997. Ambleside, U.K.: Surf. Sci.
 27. Demuth, J.E., D. Schmeisser, and P. Avouris, *Resonance Scattering of Electrons from N₂, CO, O₂, and H₂ Adsorbed on a Silver Surface*. Phys. Rev. Let., 1981. 47: p. 1166-1169.
 28. Sanche, L., *Low-energy electron scattering from molecules on surfaces*. J. Phys. B: At. Mol. Opt. Phys., 1990. 23: p. 1597-1624.
 29. Rous, P.J., *The lifetime and energy of the 2 $\dot{\gamma}$ shape resonance of N₂ adsorbed on Ag(111): the role of the substrate electronic structure*. Surf. Sci., 1995. 326: p. 67-79.
 30. Harris, S.M. and S. Holloway, *Resonant inelastic scattering of electrons from gas-phase and physisorbed N₂*. Chem. Phys. Lett., 1995. 243: p. 393-401.
 31. Frederick, B.G., Q. Chen, F.M. Leibsle, S.S. Dhesi, and N.V. Richardson, *Electron stimulated disordering in c(8x2) benzoate/Cu(110) surface: A combined STM, LEED and HREELS Study*. Surf. Sci., 1997. 394: p. 26-46.
 32. Akavoor, P., W. Menezes, L.L. Kesmodel, G. Apai, and W.P. McKenna, *High-resolution electron-energy-loss spectroscopy and infrared-spectroscopy of polymer surfaces - high-resolution and orientation effects of polytetrafluoroethylene films*. J. Vac. Sci. Technol., 1996. A 14(1): p. 95-103.

33. Apai, G., W.P. McKenna, P. Akavoor, and L.L. Kesmodel, *HREELS Detection of resonance Electron scattering in oriented polytetrafluoroethylene*. in *41st National Symposium of the American Vacuum Society*. 1994. Denver, Co.
34. Dannetun, P., M. Schot, and M.R. Vilar, *High-resolution electron energy loss spectroscopy of thin crystalline highly oriented films of polytetrafluoroethylene*. *Thin Solid Films*, 1996. **286**: p. 321-329.
35. Frederick, B.G., B.B. Frederick, and N.V. Richardson, *Multiple scattering and defining the background for resolution enhancement in HREELS*. *Surf. Sci.*, 1996. **368**: p. 82-95.
36. Frederick, B.G., G.L. Nyberg, and N.V. Richardson, *Spectral Restoration in HREELS*. *J. Electron Spectrosc. Relat. Phenom.*, 1993. **64/65**: p. 825.
37. Thiry, P.A., M. Liehr, J.J. Pireaux, and R. Caudano, *High Resolution Electron Energy Loss Spectroscopy of Insulators*. *J. Electron Spectrosc. Relat. Phenom.*, 1986. **39**: p. 69-78.
38. Madey, T.E. and J. J. T. Yates, *Surf. Sci.*, 1977. **63**: p. 203-231.
39. Richardson, N.V. and T.S. Jones, *The Angular Behaviour of Electrons Inelastically Scattered from the shape Resonance for CO Chemisorbed on Ni(110)*. *Appl. Phys. A*, 1990. **51**: p. 126-131.
40. Vlasak, P.R., D.J. Beussman, M.R. Davenport, and C.G. Enke, *An interleaved comb ion deflection gate for m/z selection in time-of-flight mass spectrometry*. *Rev. Sci. Instrum.*, 1996. **67**(1): p. 68-72.
41. Brock, A., N. Rodriguez, and R.N. Zare, *Hadamard Transform Time-of-flight Mass Spectrometry*. *Anal. Chem.*, 1998. **70**: p. 3735-3741.
42. Brock, A., N. Rodriguez, and R.N. Zare, *Characterization of a Hadamard transform time-of-flight mass spectrometer*. *Rev. Sci. Instr.*, 2000. **71**(3): p. 1306-1318.
43. Uehara, Y., T. Ushiroku, S. Ushioda, and Y. Murata, *High resolution time of flight electron spectrometer*. *Jap. J. App. Phys.*, 1990. **29**(12): p. 2858-2863.
44. Hatfield, J.V., J. Comer, T.A. York, and P.J. Hicks, *A new generation of integrate multichannel single-particle detectors*. *Rev. Sci. Instrum.*, 1992. **63**(1): p. 792-796.
45. Downie, P., D. Litchfield, R. Parsons, D.J. Reynolds, and I. Powis, *High-resolution position-sensing resistive anode microchannel plate detector systems suitable for megahertz count-rates*. *Meas. Sci. Technol.*, 1993. **4**: p. 1293-1296.
46. Richter, L.J. and W. Ho, *Position-sensitive detector performance and relevance to time-resolved electron energy loss spectroscopy*. *Rev. Sci. Instrum.*, 1986. **57**(8): p. 1469-1478.
47. Charbonneau, S., L.B. Allard, J.F. Young, G. Dyck, and B.J. Kyle, *Two-dimensional time-resolved imaging with 100-ps resolution using a resistive anode photomultiplier tube*. *Rev. Sci. Instrum.*, 1992. **63**(11): p. 5315-5319.
48. Kevan, S.D. and L.H. Dubois, *Development of dispersion compensation for use in high-resolution electron-energy-loss spectroscopy*. *Rev. Sci. Instrum.*, 1984. **55**(10): p. 1604-1612.
49. Okuyama, H., S. Shimonaka, Y. Yasui, T. Takaoka, M. Nishijima, and Y. Taguchi, *Dispersion-compensation electron-energy-loss spectrometer*. *Jap. J. Appl. Phys.*, 1998. **37**: p. 6248-6252.

50. Wu, K.J., L.D. Peterson, G.S. Elliott, S.D. Kevan, K.D. Gibson, B.J. Hinch, and L.H. Dubois, *Dispersion compensation high-resolution electron energy-loss spectrometer for time-resolved surface studies*. Rev. Sci. Instrum., 1991. **62**(5): p. 1256-1262.
51. Ho, W., *Spectroscopy of surface kinetics and reaction mechanisms*. J. Phys. Chem., 1987. **91**: p. 766-779.
52. Benninghoven, A., F.G. Rudenauer, and H.W. Werner, *Secondary ion mass spectrometry. Basic concepts, instrumental aspects, applications, and trends*. John Wiley & Sons, 1987.
53. Dodonov, A.F., I.V. Chernushevich, T.F. Dodonov, V.V. Raznikov, and V.L. Talroze, *USSR Patent 1681340A1*. 1987.
54. Laiko, V.V. and A.F. Dodonov, *Time of Flight Mass Spectrometer*. Rapid Commun. Mass. Spectrom., 1994. **8**: p. 720-726.
55. Buevoz, J.L. and G. Roullet, *Use of a correlation chopper for time of flight neutron scattering. Part II: Deconvolution in the experimental case*. Rev. de Phys. Appl., 1977. **12**: p. 597.
56. Cussen, L.D., J.C. Osborn, P. Gibbs, and T.J. Hicks, *The use of a pseudo-random spin flipper sequence on a polarised neutron scattering instrument*. Nucl. Instr. and Meth., 1992. **A314**: p. 155-162.
57. Nowikow, C.V. and R. Grice, *Cross-correlation time-of-flight analysis of molecular beam scattering*. J. Phys. E: Sci. Instrum., 1979. **12**: p. 515-521.
58. Harwit, M. and N.J.A. Sloane, *Hadamard Transform Optics*. 1979.
59. MacWilliams, F.J. and N.J.A. Sloane, *{PRBS maximal length shift register sequences}*. Proc. IEEE, 1976. **64**(12): p. 1715-1730.
60. Fellgett, P., J. Phys. Radium, 1958. **19**: p. 187.
61. Plankey, F.W. and J.D. Winefordner, *Paper No. 200*. Pittsburgh Conference on Analytical Chemistry and Applied Spectroscopy, 1974.
62. Larson, N.M., R. Crossman, and Y. Talmi, *Theoretical Comparison of Singly Multiplexed Hadamard Transform Spectrometers and Scanning Spectrometers*. Applied Optics, 1974. **13**: p. 2662-2668.
63. Wilhelmi, G. and F. Gompf, *Binary sequences and error analysis for pseudo-statistical neutron modulators with different duty cycles*. Nucl. Instr. and Meth., 1970. **81**: p. 36-44.
64. Zeppenfeld, P., M. Krzyzowski, C. Romainczyk, and R. David, *On the origin of spurious peaks in pseudorandom time-of-flight analysis*. Rev. Sci. Instrum., 1993. **64**(6): p. 1520-1523.
65. Cornwell, T.J., *Image Restoration*. Proc. NATO Advanced Study Institute on Diffraction-Limited Imaging with Very Large Telescopes, 1988: p. 273-292.
66. Wang, Y. and W.H. Weinberg, *Ultrahigh resolution electron energy loss spectroscopy*. Phys. Rev. Lett., 1994. **73**: p. 773.
67. Lucy, L.B., *An iterative technique for the rectification of observed distributions*. Astron. J., 1974. **79**: p. 745.
68. Cittert, P.H.v., *Zum Einfluß der Spaltbreite auf die Intensitätsverteilung in Spektrallinien*. Z. Phys, 1931. **69**: p. 298-308.

69. Bachrach, R.Z., F.C. Brown, and S.B.M. Hagström, *Photoelectron spectroscopy by the time-of-flight technique using synchrotron radiation*. J. Vac. Sci. Technol., 1975. **12**(1): p. 309-312.
70. White, M.G., R.A. Rosenberg, G. Gabor, E.D. Poliakoff, G. Thornton, S.H. Southworth, and D.A. Shirley, *Time-of-flight photoelectron spectroscopy of gases using synchrotron radiation*. Rev. Sci. Instrum., 1979. **50**(10): p. 1268-1273.
71. Berrah, N., B. Langer, A. Wills, E. Kukk, and J.D. Bozek, *Two-dimensional Imaging of Atoms and Molecules Using Angle-Resolved, Electron Time-of-Flight Spectroscopy at the ALS*. Synchrotron Radiation News, 1998. **11**(2): p. 21-24.
72. Loeb, L.B., *Basic Processes of Gaseous Electronics*. 1961, Berkeley: Univ. of California.
73. LeCursi, N., L.J. LeGore, R.H.J. III, C.B.H. Crothers, P.H. Kleban, and B.G. Frederick, *Fabrication of Chopper for Particle Beam Instrument*. US Patent Application No: 10/165,851, 2002.
74. Frederick, B.G., T. Hildebrandt, C.C. Perry, Q. Chen, A.W. Munz, T. Bertrams, V. Zielasek, N.V. Richardson, and M. Henzler, *Inelastic Diffraction in Coadsorbed Periodic Structures*. Surf. Sci., 1998. **418**: p. 407-419.
75. Jackson, R.H., L.J. LeGore, Z. Yang, P. Kleban, and B.G. Frederick, *Application of the Interleaved Comb Chopper to TOF Electron Spectrometry*. Surf. Sci., 2001: p. (in press).
76. Frederick, B.G., *Method for Enhancement of Electron Spectrometer Operation Using Maximum Likelihood Spectral Estimation Techniques*. 2001, Univ. of Maine: USA. p. (patent pending).
77. Rotzoll, G., *Computer simulation of different designs of pseudo-random time-of-flight velocity analysers for molecular beam scattering experiments*. J. Phys. E: Sci. Instrum., 1982. **15**: p. 708-711.
78. Steele, T.A., R.C. Unwin, and A.J. Eccles, *Charged particle velocity analyzer*. 1998: GB.
79. Bialkowski, S.E., *Overcoming the Multiplex Disadvantage by Using Maximum-Likelihood Inversion*. Appl. Spectrosc., 1998. **52**(4): p. 591-598.
80. Richardson, W.H., "Lucy algorithm". J. Opt. Soc. Am., 1972. **62**: p. 55.
81. Jackson, R.H., L.J. LeGore, Z. Yang, P. Kleban, and B.G. Frederick, *Application of the Interleaved Comb Chopper to TOF Electron Spectrometry*. Surf. Sci., 2002. **502**: p. 240-248.
82. LeGore, L.J., R.H. Jackson, Z. Yang, P. Kleban, L.K. DeNoyer, and B.G. Frederick, *Advantages of Maximum Likelihood Methods for PRBS Modulated TOF Electron Spectrometry*. Surf. Sci., 2002. **502**: p. 232-239.
83. Bradbury, N.E. and R.A. Nielsen, *Absolute Values of the Electron Mobility in Hydrogen*. Phys. Rev., 1936. **49**: p. 388.
84. Jackson, B., *The Design of Time of Flight Electron Loss spectroscopy*. To be submitted, 2003.
85. Cutler, D.J., P.J. Hendra, R.R. Rahalkar, and M.E.A. Cudby, *Vibrational Spectra of Crystalline Polytetrafluoroethylene*. Polymer, 1981. **22**: p. 726.
86. Frederick, B.G. and L.K. Denoyer, *Effects of noise and rise time on inversion PRBS modulated data using the Lucy algorithm*. To be submitted.

87. Frederick, B.G., B.B. Frederick, and N.V. Richardson, Unpublished results presented at 7th Int. Conf. Vibrations at Surfaces. Used with permission, 1996.
88. Fernandez, F., J.M. Vadillo, F. Engelke, J.R. Kimmel, R.N. Zare, N. Rodriguez, M. Wetterhall, and K. Markides, *Effect of Sequence Length, Sequence Frequency, and Data Acquisition Rate on the Performance of a Hadamard Transform Time-of-Flight Mass Spectrometer*. J. Am. Soc. Mass. Spectrom., 2001. **12**: p. 1302-1311.
89. Hanley, Q., *Masking, Photobleaching, and Spreading Effects in Hadamard Transform Imaging and Spectroscopy Systems*. Appl. Spectrosc., 2001. **55**: p. 318-330.
90. Yang, Z., R.H. Jackson, P. Kleban, and B. Frederick, *TOF-HREELS and AFM characterization of highly oriented PTFE films*. To be submitted.
91. Chen, Q., B.G. Frederick, and N.V. Richardson, *An HREELS study of γ^* and σ^* negative ion resonances of c(8x2) benzoate on Cu(110)*. J. Chem. Phys., 1998. **108**(14): p. 5942-5947.

BIOGRAPHY OF THE AUTHOR

Zhongyu Yang was born in Chongqing, PR China on April 2, 1973. He was raised in Urumuqi, Xing Jiang province, PR China and graduated from Trailroad No. 3 middle school in 1990. He attended the East China Normal University and graduated in 1994 with a Bachelor's degree in Physics. He went to Beijing and worked as a technician in Beijing University. He entered the Physics graduate program at The University of Maine in the fall of 1997.

After receiving his PhD degree, Zhongyu will pursue a postdoc position in the surface science field to begin his career. Zhongyu is a candidate for the Doctor of Philosophy degree in Physics from The University of Maine in May, 2003.